2016-01-01

Liquid-Phase Exfoliation Of Two-Dimensional Graphite For Ink-Jet Printing

Monica Michel
University of Texas at El Paso, monicamichelp@gmail.com

LIQUID-PHASE EXFOLIATION OF TWO-DIMENSIONAL GRAPHITE FOR INK-JET PRINTING

MONICA MICHEL PARRA

Doctoral Program in Materials Science and Engineering

APPROVED:

Anupama B Kaul, Ph.D., Chair

Thomas Boland, Ph.D.

Stephen Stafford, Ph.D.

Cristian Botez, Ph.D.

Charles Ambler, Ph.D.
Dean of the Graduate School

LIQUID-PHASE EXFOLIATION OF TWO-DIMENSIONAL GRAPHITE FOR INK-JET PRINTING

by

Monica Michel Parra, M.S.

DISSERTATION

Presented to the Faculty of the Graduate School of
The University of Texas at El Paso
in Partial Fulfillment
of the Requirements
for the Degree of

DOCTOR OF PHILOSOPHY

Materials Science and Engineering
THE UNIVERSITY OF TEXAS AT EL PASO
December 2016

Acknowledgements

I want to thank Professor Anupama B. Kaul for offering me a position to join her research group, as one of the first members of the Nanomaterials and Devices Lab (NDL) that she established upon her arrival to UTEP in Sept. 2014. I value her guidance throughout my work, and in the review and significant edits she made to my journal publications and this dissertation. I would also like to thank the rest of my dissertation committee members, Professor Thomas Boland and Professor Steve Stafford in MMBME and Professor Cristian Botez from Physics, for helping review this dissertation and providing their feedback on my research work. I also would like to thank Dr. Chandan Biswas for his help, support and patience in formulating early drafts of my papers.

I greatly appreciate of the members of the NDL group for their support, especially Mr. Gustavo Saenz and Alberto Delgado who joined the group at the same time I did. I am glad we became friends very fast and they were always there to help. I want to thank everybody in the group, Jorge, Jay, Srishty, Ridwan, and Avra for always supporting me with their kind words, good sense of humor and making the group feel like a family; it was great knowing and working with you guys.

Finally, I want to thank my family, my husband Oscar and my children Rodrigo and Fernanda for their support and understanding while I dedicated so much time to this work.

Abstract

Over the last decade, the study of two-dimensional (2D) materials has seen an incredible growth due to their unique thermal, mechanical and electronic properties. Solution phase manufacturing offers a way in which they can be produced at large scale by creating dispersions from the exfoliated material. Once created, different options for assembling devices exist. One technique for large scale manufacturing of materials in this form is ink-jet printing, which is a form of additive manufacturing that has proven to be attractive for the printed electronics industry. One challenge that ink-jet printing still faces is the shortage of inks with appropriate properties, since there are many parameters that affect the success of the printing process in general. In this work, we have developed techniques for the exfoliation of bulk crystals and optimized the properties of the inks so that they are suitable for inkjet printing. Dispersions have been produced and printed successfully by preparing both surfactant–assisted and surfactant–free inks. We have analyzed the effect of some printing parameters such as varying the number of nozzles that are used for printing, the number of passes or layers printed and the annealing conditions, and characterized the structure and electronic transport properties of the printed features. The prepared inks have been printed on rigid SiO_2/Si substrates, as well as transparent and flexible polyimide substrates. The pattern printed on the polyimide was tested as a function of bending, which shed insights into the mechanical elasticity and adhesion of the printed features to the substrate with minimal changes in electrical transport properties, indicating that such structures are ideally suited for flexible electronics. In addition, high power resistor structures have been fabricated that demonstrated outstanding power with levels of up to 7 W being delivered by the printed resistive structures. Furthermore, the resulting prepared inks have shown very little variation in resistance values over a wide range of temperatures allowing them to be used in extreme thermal environments where a

nearly flat temperature coefficient of resistivity may be desired. This work shows great promise of ink-jet printed nanomaterials, and has shed insights into understanding the properties of the printed structures for electronics and flexible electronics applications.

Table of Contents

List of Tables

List of Figures

Chapter 1

Introduction

Single layer materials, also referred to as two-dimensional (2D) materials, are crystalline materials consisting of a single layer of atoms that present unique mechanical, thermal, and electric characteristics. These materials have been studied with great interest ever since the mechanical exfoliation of graphite was performed by Geim and Novoselov in 2004 using scotch tape for which they received the Nobel Prize in Physics six years later [1]. They have been subjects of innumerable studies for their singular properties, improving their synthesis and an ever increasing number of application opportunities [2].Various synthesis possibilities exist for these interesting materials, which include chemical vapor deposition (CVD) techniques [3], physical vapor deposition, mechanical exfoliation, liquid exfoliation and others, each yielding varied results [4] [5].

This rapidly growing class of materials also called 2D crystals [6], includes graphene, hexagonal boron nitride (hBN), and transition metal dichalcogenides (TMD's). The material properties exhibited by 2D crystals can vary widely, from wide band gap insulators such as hBN to semiconductors such as TMD's to zero gap semimetals such as graphene. Despite this variety, all 2D crystals have strong interconnecting bonds while concurrently demonstrating weak interlayer bonding. It is this weak interlayer van der Waals bonding that allows a single layer to be peeled away, or mechanically exfoliated, from the bulk material to produce small, high-quality 2D crystals. Resulting from the exponential growth in knowledge about the unique properties of 2D materials, other compounds and elements besides graphene have generated great interest in

various research fields, specifically MoS_2. In contrast to the linear, gapless energy dispersion of graphene, single-layer MoS_2 is a direct-gap semiconductor with reasonable electronic mobility [7] [8]. TMDs can be described by the chemical formula MX_2, where M is a transition metal atom (from group 4–10 of the periodic table) and X is a chalcogenide species (e.g. S, Se, Te). There are over 40 known TMDs that exist in bulk form [9] [10], depending on the coordination and oxidation state of the metal atoms, or doping of the lattice, TMDs can be metallic, semi metallic or semiconducting [10].

Mechanical exfoliation is a quick and effective means to produce individual 2D crystals for fundamental investigations and materials exfoliated like this are among the highest quality samples available [11, 12, 13]; however, this technique limits production to micron-sized fragments. The exfoliation of 3D material or the bulk in liquids is one possible solution for obtaining larger quantities of dispersed nano sheets. Many authors have followed different paths in the pursuit of isolating single layers of the honey-comb structured carbon atoms, namely graphene, which also includes successfully dispersing and exfoliating graphene oxide (GO) [14, 15]. The problem with this approach is that GO is an insulator which has been chemically functionalized with compounds such as hydroxyls and epoxides. Even though the functionalization components are removed through processing, a significant amount of defects are still left that continue to degrade electronic properties [16]. Graphite flakes have been exfoliated by various research groups, having obtained low concentration dispersions of small graphene flakes. Progress is being made in getting higher concentrations and providing coverage over greater areas by varying solvents [17] [18] with the disadvantage that some of the most promising solvents are toxic, so their use is restricted to certain environments. Many of the ways of synthesizing graphene have been adapted to other 2D materials, such as MoS_2. By exfoliating graphite flakes, monolayer

graphene has been successfully obtained in solvents with surface tensions close to 40 mJ/m^2 [18, 19, 20]. In this work, we have studied five solvents with surface tensions ranging from 23 to 41 mJ/m^2, polarities that range from 3.9 to 6.7, different functional groups, molecular weights; we have also explored more environment friendly solvents, such as Terpineol and Isopropyl alcohol.

One manufacturing technique for solution-based 2D materials is inkjet printing, which has the advantage of digital and additive patterning, a reduction in material waste, and compatibility with different substrates and degrees of mechanical flexibility and forms [11]. Success in this technology is illustrated with the components that have already been inkjet – printed, such as transistors, solar cells, light–emitting diodes, and sensors [21, 22, 23]. Liquid exfoliation of the bulk material is just the first step for printing 2D materials. Once the dispersions have been formulated, they need to be modified to be suitable for the inkjet printing process [22, 24]. Some important physical operations that both define and constrain inkjet printing are: the generation of droplets, positioning and interaction of droplets on a substrate, and drying or other solidification mechanism to produce a solid deposit [25]. Fluid dynamics are involved in the generation of droplets, and it has been determined that the most important physical parameters affecting printing fluids are viscosity, density and surface tension [26, 27, 28].

A component that has been utilized to stabilize the ink dispersions of nanomaterials is Ethyl Cellulose (EC), which is mostly used in coating applications and as a rheology modifier; it is a surfactant that is essentially cellulose and has had some of the hydroxyl groups in its linear chain converted into ethyl ether groups. We have implemented its use here as a stabilizing polymer and surfactant to prevent nanoparticle agglomeration [24, 29]; however, we have studied the effect of its addition before or after sonication. The EC has also been used to modify the viscosity of the solvents to make them more suitable for printing. We have characterized our prepared dispersions

with the help of absorption spectroscopy to compare the amount of nano – particles in each of the five solvents for different sonication times. Optical absorbance has long been used by many authors for example to calculate concentrations [30, 30, 31, 32, 33] by using The Beer – Lambert law. From this optical characterization, we selected the solvents with the highest nano particle concentrations to prepare the inks for printing.

1.1 PRODUCTION OF 2D MATERIALS

One of the first steps in order to use either graphene or other type of 2D material is to synthesize the material. Options include exfoliation, either mechanical or liquid [34]; chemical vapor deposition can be used; recently graphene films have been grown on polycrystalline metal substrates using spin coated polystyrene or polyaniline as a carbon source [35].

In early studies, accidental carbon deposition on and precipitation from metal substrates resulted in graphene formation [36, 37, 38]. Since then graphene growth on many different metal substrates has been studied [39]. In contrast, chemical vapor deposition (CVD) is a technique capable of providing large-area, scalable, cost effective and high-quality crystalline material while also being compatible with standard semiconductor processing techniques [40]. The most studied CVD process for graphene on metals are Ni, Cu, Cu single crystals, and Ir. [6]

Many of the studies and techniques originally intended only for graphene synthesis have provided a strong foundation for the more nascent areas of hexagonal boron nitride (hBN [41, 42] and TMD growth. [43]

1.1.1 Exfoliation

The production of extremely thin sheets from layered precursors is known as exfoliation or delamination. This process has had a tremendous effect on materials science by opening up

properties found only in the 2D form which differ from the bulk materials. Although mechanical exfoliation is a quick and effective means to produce individual crystals for fundamental investigations, this technique limits production to micron-sized fragments, which must be painstakingly sought out.

Liquid – phase exfoliation facilitates the integration of the materials into large – area electronics through the well- known solution – based techniques, such as inkjet printing and roll to roll coating [44]. One of the first approaches to liquid exfoliation was the oxidation of graphite, demonstrated by the monolayer thickness graphite oxide (GO), which although it is electrically insulating, it can be rendered conducting by reduction [15]. At this time, monolayer graphene has finally been successfully exfoliated by using solvents with surface tension close to 40 mJ/m2 [45]. Scientists have obtained low concentration dispersions of small but high quality, defect free graphene flakes, and progress is being made in getting higher concentrations and greater areas by varying solvents such as NMP M – methylpyrrolidone, ethanol, dimethylsulfoxide (DMSO), acetone, acetonitrile, tetrahydrofuran (THF), diethylether, toluene, 1,2 dichlorobenzene (DCB)in different concentrations and combinations [20, 46]. Figure 1.1 illustrates the liquid exfoliation mechanism of separating the bulk material into layers.

Graphene has been exfoliated in aqueous surfactant solutions and also in polymer solutions, although water, with its surface tension of 72 mJ/m^2, cannot by itself exfoliate graphite; when ultra-sonicated and later stabilized, few layer graphene has been obtained [47, 48]. A promising printable graphene ink in ethanol and water totally free of any surfactant, has been obtained with a solvent – exchange method switching from NMP to a water/ethanol solution [49]. A method of exfoliation into single – layer graphene has been reported, showing graphite spontaneously exfoliating in chlorosulphonic acid, with a concentration of 2 mg/ml in the solution [50]. Behatbu

et al. were able to achieve this without the need for functionalization, surfactant stabilization, or sonication, which can compromise the properties of graphene or reduce flake size.

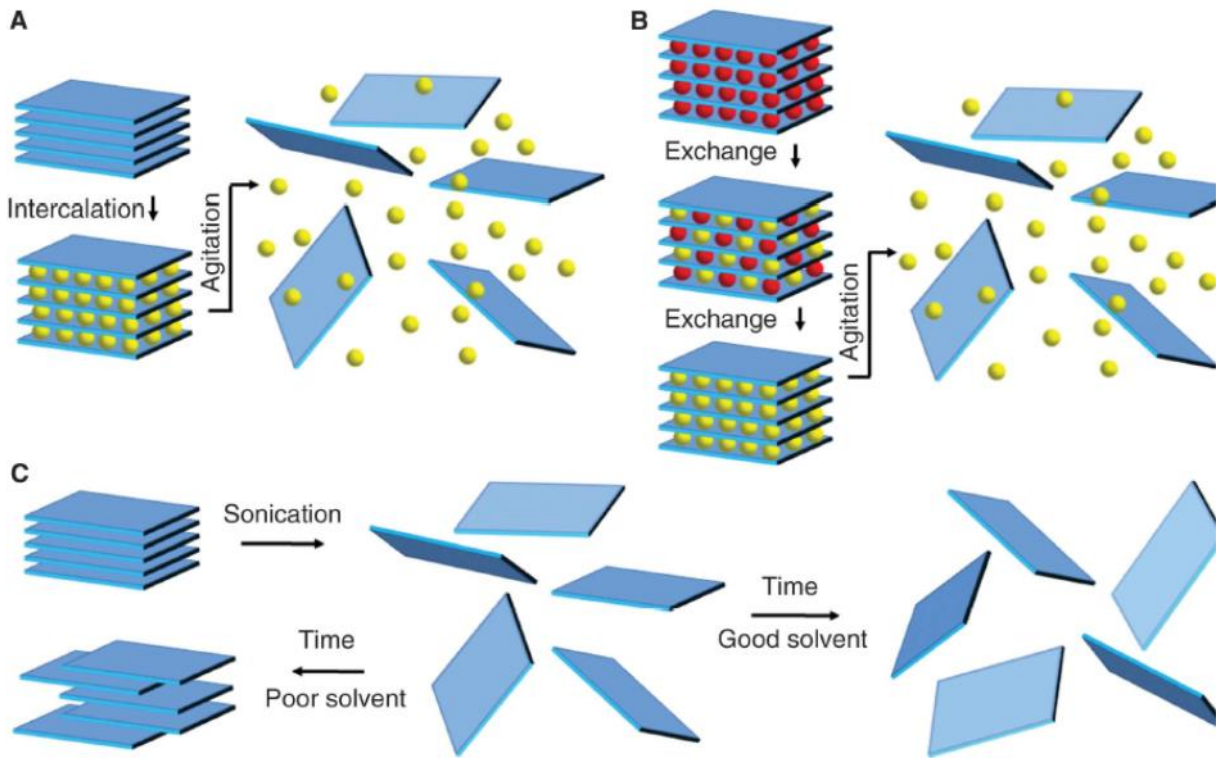

Figure 1.1: Liquid exfoliation mechanism.

Both h-BN and a range of TMDs can be exfoliated with similar methods as those used for graphene, either using solvents and a surfactant or polymer solutions [46, 51]. Dispersions with concentrations as high as 40 mg/ml have been obtained for MoS_2, Ws_2, $MoSe_2$, $MoTe_2$, $TaSe_2$ and $NbSe_2$. [52, 53].

Ultrasonic cavitation has been used and determined to be helpful in the production of two dimensional nano-sheets of graphene, TMC and the de-bundling of carbon nanotubes in solution, in particular, acoustic cavitation. Even though sometimes the high speed jets and intense shock

waves can diminish the size of the nano-sheets or generate defects, which decreases their electrical and other useful properties, the process can be adapted to produce useful material [54].

1.1.2 Growth

There have been different types of studies about growing graphene as film, usually requiring transfer after deposition on a material. Some teams have attempted to avoid this transfer; for example, one can evaporate the thin metal substrate after the graphene growth, or directly depositing carbon or a carbon – based layer on SiO_2 before depositing nickel atop and then annealing to transform the carbon into graphene, but most of these techniques still require very high temperatures. Graphene has been successfully grown in the interface of SiO_2 /Ni, with PECVD with temperatures as low as 450℃ [55]. Graphene films have been grown using a carbon source of polyaniline or polystyrene film that have been spin coated on polycrystalline metal substrates. An easy method has been developed which does not require any gas [35], and the vacuums required are very manageable.

In the case of hBN, sputtering, MBE (molecular beam epitaxy) and IBAD (ion beam assisted deposition) provide some alternative methods for its deposition, an example being the monolayer hBN deposition on Cu foil under low pressure (350 mTorr) using an ammonia borane precursor [56]. For MoS_2, the majority of growth processes can be performed in a quartz tube furnace and have implemented one of the following precursors: (a) thin films of Mo metal, (b) liquid solutions containing ammonia tetrathiomolybdate, or (c) MoO_3 powder. It is known that sulfur forms sulfides with most metals, so the MoS_2 formation is a product of elemental reactions between Mo and S [57, 58, 59]. The selected temperatures, as well as substrate, can impact the crystal quality, with higher temperatures and sapphire substrates demonstrating highest quality growth. The sulfur source may also have an effect on the uniformity of the resulting MoS_2. When

H_2S gas is used, as opposed to the more commonly used vaporized elemental sulfur, uniform films from 2 to 12 layers were synthesized, although with typical grain sizes on the order of 10–30 nm, considerably smaller than that of mechanically exfoliated MoS_2 crystals.

1.2 PRINTED ELECTRONICS

Over half of a millennium ago the first printing press revolutionized the reproduction of manuscripts and books by drastically cutting costs and increasing production capacity; modern day inkjet printers are revolutionizing electronics fabrication by allowing for faster, cheaper, more flexible, and more accessible methods to pattern and package electronic circuits and systems [25]. The variety of printing methods adapted to create electrical devices in different substrates result in what we now call "printed electronics". Normal printing equipment is used to define the patterns, such as serigraphy, flexography, gravure, lithography, ink jet printing, and more. The inks are usually deposited on the substrate creating either active or passive devices, such as resistors or transistors. The idea is printed electronics facilitate at a very low cost, getting printed bending and flexible screens, flexible solar cells, printed batteries, intelligent or smart sensors, and many more.

Among available manufacturing techniques for electronics, a promising approach is inkjet –based – printing, due to the rapid development and deployment of new material inks. One advantage is its digital and additive patterning, reduction in material waste, and compatibility with different substrates and degrees of mechanical flexibility and forms. Ink-jet printing is a versatile technique for the large-area fabrication of flexible electronics, requiring minimal process steps, and serves as one of the cornerstone processes for additive manufacturing [60]. Ink-jet printing has emerged as the approach for the rapid manufacturing of thin-film transistors (TFTs), which are constructed using organic conducting and semiconducting inks [61]. However, despite notable advances, ink-jet printed organic TFTs still show poor air stability, limited lifetime, low mobilities

(< 0.5 $cm^2V^{-1}s^{-1}$) and the ON/OFF ratios are typically $<10^5$ [22]. Such limitations arise primarily from the poor quality of the materials used as the inks in such organic systems. In this work, we report on forming 2DLM-based dispersions suitable for ink-jet printing, where the 2DLMs offer unique attributes, such as greater air-stability, higher-mobilities, and ease of chemical exfoliation given their unique crystal structures. While there are a wide variety of 2DLMs, here we investigate the dispersion characteristics of two specific 2DLMs, i.e. metallic graphite and semiconducting MoS_2.

1.2.1 Printable Fluids

Prior to forming inks of 2DLMs, they must first be dispersed as nanosheets in a liquid. Early work on solution-based exfoliation of graphite comprised of intercalated graphite which could be partially exfoliated by reactions involving an intercalant [62], through thermal shock [63], or by the shear oxidation of graphite [64, 65, 66, 67]. The oxidation of graphite to yield graphene has resulted in fragments of oxidized sheets that exhibit significant structural defects and are often electrically insulating [15].

The choice of solvents used for exfoliation plays a key role for successfully isolating high-quality single layers of 2DLMs that are stable against re-aggregation. Modeling has shown that if the surface energy of the solvent is similar to that of the LM, the energy difference between the exfoliated and re-aggregated states will be very small, removing the driving force for re-aggregation [12]. Kamat, Park, and others have shown that several organic solvents have cohesive energies close to the interlayer energies of 2DLMs, in particular the transition metal dichalcogenides, where the lattice can expand by as much as 100 times when they are dispersed in such solvents [68, 69]. Through these deductions, the most promising solvents for achieving stable suspensions of 2DLMs appear to be N-methyl-2-pyrrolidone (NMP), *N,N*-Dimethylacetamide

(DMA) and dimethylformamide (DMF) [52], while hydrazine, cyclohexyl-pyrrolidinone (CHP), G-Butyrolactone (GBL), 1,3-Dimethyl-2-Imidazolidinone (DMEU) are also known to be effective, while some groups are exploring more nontraditional solvents like ethanol [30, 70]. In this work, we have explored the role of the first three solvents in forming suspensions of 2D MoS_2 and graphite, while also exploring the effect of less toxic and more environmentally friendly solvents, such as Isopropanol (IPA) and Terpineol (T).

1.2.2 The Printing Process

The printing process is seemingly a simple one, with the first step being to load ink into a reservoir that feeds a nozzle. In the second step this nozzle is moved horizontally over a substrate, and an actuator is used to eject a drop of ink from the nozzle. In the third step, the ink droplet hits and adsorbs to the surface of the substrate. Some very important key features must be kept in mind when selecting the optimal printing process, including but not limited to:

• Nozzle type and characteristics (piezo, thermal, electrostatic, acoustic, actuation, waveform)

• Ink formulation (material loading, viscosity, surface tension, carrier fluid).

• Substrate or top-layer surface properties (roughness, free surface energy, ink chemical compatibility).

• Post-print curing (annealing pressure and temperature, ultraviolet (UV) exposure, laser annealing) [25].

1.2.2.1 Inkjet printing theory

There are two different mechanisms or ways in which inkjet printing can take place, continuous inkjet (CIJ) printing and drop - on - demand (DoD) (see Figure 1.2). In both cases, the drop generated can have a diameter around 10 to 150 μm. The essential difference is that DOD generate individual drops when required, while CIJ operates with constant or continuous drop

generation. In CIJ Drop positioning is controlled by moving a drop in flight or by moving the substrate to where a drop is to be printed, DOD locates the printer nozzle above the desired location before the drop is ejected. CIJ is a more wasteful process, since even when the ink can be recirculated, contamination may still occur [71].

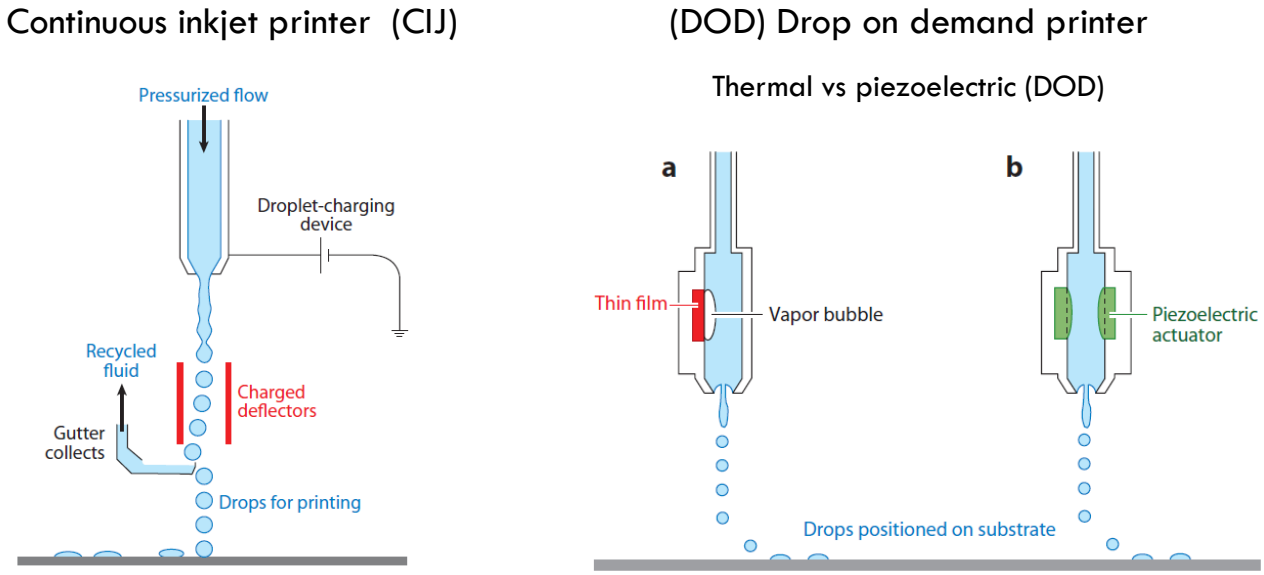

Figure 1.2: Inkjet printing mechanisms. Continuous Inkjet Printing (CIJ) and Drop on Demand (DOD).

In DOD, an actuation mechanism transfers energy to a suitable volume of liquid, in order for it to form a drop. Various actuation mechanisms have been proposed and patented, but the most common techniques are thermal (or bubble) actuation and piezoelectric actuation (PA). In thermal DOD printing, a small heater is located in the fluid chamber, where the fluid is heated forming a small bubble. The rapid expansion and collapse of this bubble generate a pressure pulse that promotes the drop formation and ejection. In piezoelectric DOD printing, the pressure pulse is generated by direct mechanical actuation using a piezoelectric transducer that may be achieved

using MEMS technology and electrostatic forces [72] (see DOD in Figure 1.2b). The piezoelectric effect is the ability of certain materials to generate an electric field in response to mechanical strain, or, similarly, to undergo a change in shape when subjected to an electric field. The direction of mechanical deformation (extension or compression) depends on the direction of the applied field, or the polarity of the applied voltage [73]. In many PA systems, lead Zirconate Titanate (PZT) is used as the active component, due to its strong piezoelectric effect. Different mechanisms are possible for the actuators, push – mode which rely directly on expansion and contraction (see Figure 1.3); shear – mode which create two regions of shear, creating a wall movement; and finally squeeze - mode, in which two layers are used to form a cylinder so that when the field is applied from the outside to the inside, it will contract radially [74].

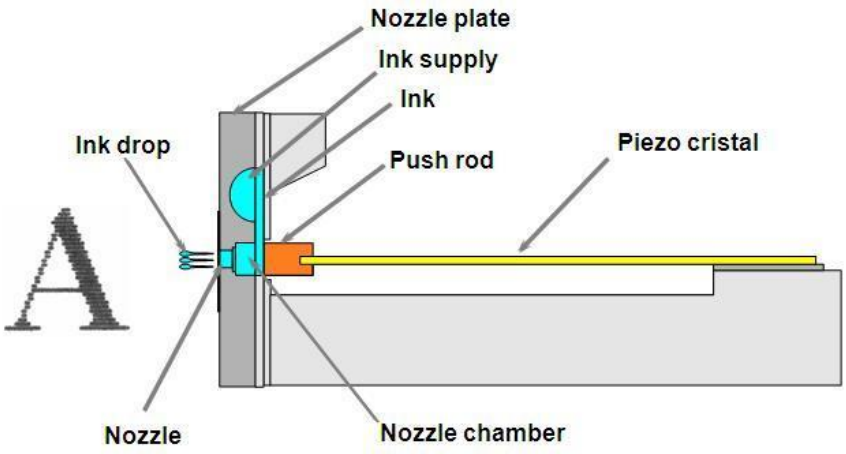

Figure 1.3: Piezoelectric actuator figure.

1.2.2.2 The waveform

In order to optimize the patterns formed by printing, it is important to control the droplet volume, which is a direct result of the waveform that is created at the nozzle. This waveform drives the piezoelectric material which acts on the liquid. The waveform is the combination of the operating conditions of the piezoelectric actuator, which are the driving voltage and the pulse width. By combining different voltage amplitudes, pulse durations, and shapes, different droplet

volumes can be obtained [75, 76]. Inappropriate inks may result in unstable jetting with long filaments forming connecting the ejected droplet to the nozzle [77], which may be corrected by modifying printing parameters. Hwang et al. have studied unipolar, bipolar, M-shaped and W-shaped waveforms and their effect on the drop formation [78, 79]. Time after time, it has been proven that it is not only fluid properties like viscosity, density and surface tension that control the printability of inks, but also the orifice size and the driving waveform parameters, such as voltage value, waveform shape, and pulse time . For example, it has been found that a double waveform with an appropriate interval time between two pulses can generate a single droplet by creating an additional negative pressure to avoid satellite droplets arising from long liquid threads in high-Z-value fluid [80, 81, 82]. A bipolar waveform allows a high voltage difference without the application of an excessively high voltage. In the inkjet printing process, the piezoelectricity, elasticity, and free-surface fluid dynamics should all be considered [83].

1.2.2.3 The Substrate

Due to its additive nature, inkjet printing can be adapted to print in many different substrates: silicon wafers, plastic, paper, cloth, etc., can be used [84, 85]. The selection of a substrate depends on the final characteristics that are desired from the device. The final image or pattern should be a solid object on the substrate, and this liquid – to – solid phase change can occur by a number of mechanisms, and either by itself, of after some kind of treatment. It is therefore important to understand the interactions that occur between the substrate and the fluid in this period. The first interaction that occurs as the drop touches the substrate, is influenced by the fluid properties and the condition of the substrate. At the moment of impact, there may be that splashing occurs. There is a difference in splashing between Newtonian and non-Newtonian fluids to start

with, and it can also be influenced by the nature of the substrate; surface roughness and impact velocity have been proven critical [86, 87], and viscosity is a key parameter in this process [88].

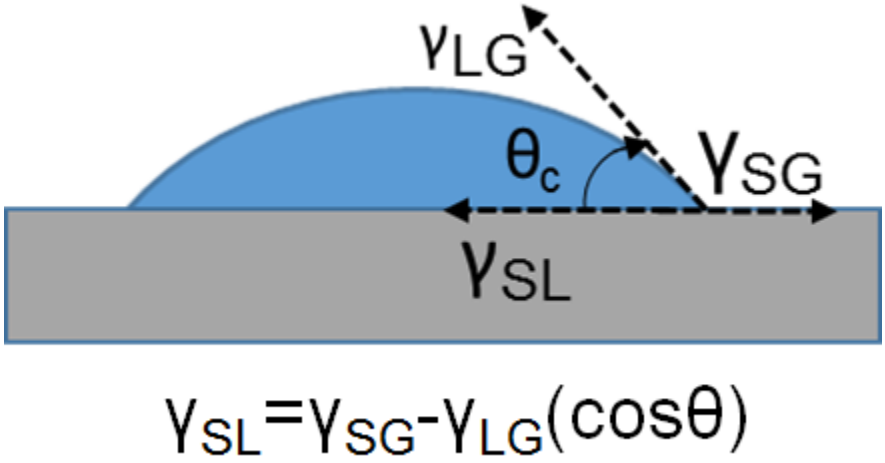

Figure 1.4: Contact angle and Young's Equation.

When a liquid is in contact with a surface, it will tend towards an equilibrium shape that balances all the forces. This shape manifests itself in the form of an equilibrium contact angle and is described by Young's Equation [89] (see Figure 1.4). Young's Equation describes the balance between the three surface energies at interaction if no other forces act upon the system: the surface energy between the liquid and the surrounding environment γ_{LV}, the surface energy between the solid and the surrounding environment γ_{SV} and the surface energy between the liquid and the solid γ_{LS}. The equilibrium wetting of a drop may be further influenced by gravitational forces, roughness of the substrate, the hydrophobic or hydrophilic character of the droplet, as well as other issues such as dust contamination or a solid phase within the droplet (suspensions or ink in our case) [90].

The main difference between printing substrates, besides the different interactions it may have with the fluid, is whether it is flexible, or not. Flexibility may have different meanings, so

we can classify it in three categories: (1) bendable or rollable, (2) permanently shaped, and (3) elastically stretchable. All three types are currently manufactured in an initially flat form, that are later either rolled or bent, shaped to the desired geometry [91, 92], or as in the case of the stretchable electronics, made interconnected with elastically stretchable conductors [93, 94, 95]. In the specific case of flexible electronics, carbon nanotubes (CNT's) are currently under wide study and have already been used to make flexible circuits, flexible displays, flexible solar cells, conformable radio frequency identification (RFID) tags, skin-like stretchable and flexible pressure, strain, and chemical and biological sensors. In addition, they have also been used as the anode and cathode in flexible light emitting diodes, solar cells, and supercapacitors [96]. And these are just examples of uses of CNT's, which still leaves a wide range of organic electronics to mention.

1.3 CHARACTERIZATION

1.3.1 SEM microscopy

Scanning Electron Microscopy (SEM) works by focusing a beam of high-energy electrons to generate a variety of signals at the surface of solid specimens. This signal reveal information such as morphology (texture), chemical composition and crystalline structure and orientation of materials making up the sample. The SEM can perform analyses of selected point locations on the sample; this approach is especially useful in qualitatively or semi-quantitatively analysis to determine chemical compositions (using EDS), crystalline structure, and crystal orientations (using EBSD). The basic principle of the SEM is to capture a variety of signals produced by electron-sample interactions when the incident electrons from the beam are decelerated in the solid sample. These signals include secondary electrons (that produce SEM images), backscattered

electrons (BSE), diffracted backscattered electrons (EBSD that are used to determine crystal structures and orientations of minerals), photons (characteristic X-rays that are used for elemental analysis and continuum X-rays), visible light (cathodoluminescence–CL), and heat.

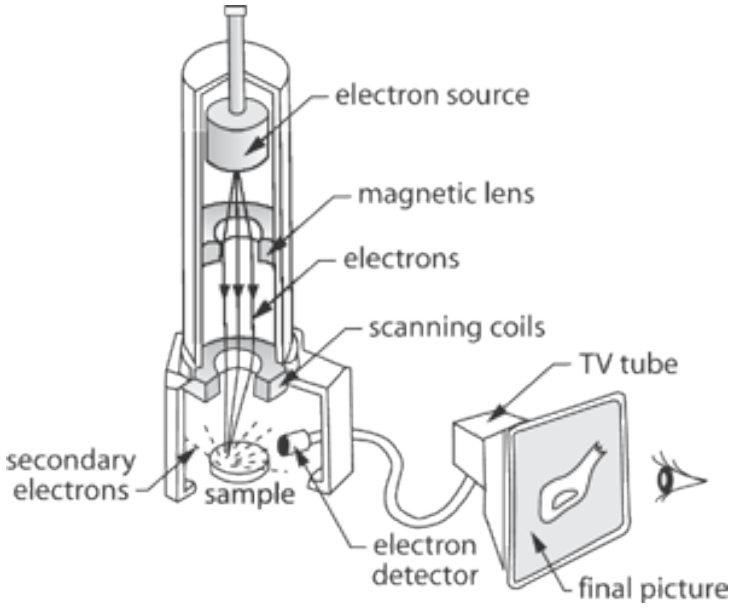

Figure 1.5: Diagram of Scanning electron Microscope.

Figure 1.5 illustrates the components and basic principle of SEM. Secondary electrons and backscattered electrons are commonly used for imaging samples: secondary electrons are most valuable for showing morphology and topography on samples and backscattered electrons are most valuable for illustrating contrasts in composition in multiphase samples (i.e. for rapid phase discrimination). A Hitachi S4800, which can be seen in Figure 1.6 was used for the SEM analysis in this work. X-ray generation is produced by inelastic collisions of the incident electrons with electrons in discrete orbitals (shells) of atoms in the sample. As the excited electrons return to lower energy states, they yield X-rays that are of a fixed wavelength (that is related to the difference in energy levels of electrons in different shells for a given element). Thus, characteristic X-rays are produced for each element in a mineral that is "excited" by the electron beam. SEM

analysis is considered to be "non-destructive"; that is, x-rays generated by electron interactions do not lead to volume loss of the sample, so it is possible to analyze the same materials repeatedly [97, 98, 99].

Figure 1.6: Hitachi S4800 used throughout our work.

1.3.2 Absorption Spectroscopy

Absorption Spectroscopy uses light in the visible and adjacent (near-UV and near-infrared [NIR]) ranges to measure the absorption or reflectance of the radiation from the material to be analyzed. The basic principle is that molecules containing π-electrons or non-bonding electrons (n-electrons) can absorb the energy in the form of ultraviolet or visible light to excite these electrons to higher anti-bonding molecular orbitals. The more easily excited the electrons (i.e.

lower energy gap between the HOMO and the LUMO), the longer the wavelength of light it can absorb. For a molecule to absorb energy of a specific wavelength, it must have two energy levels separated exactly by the energy of the photon that will be absorbed; one needs to have a vacancy that will accept the electron that will jump from the lower energy level [100]. This process is illustrated in Figure 1.7.

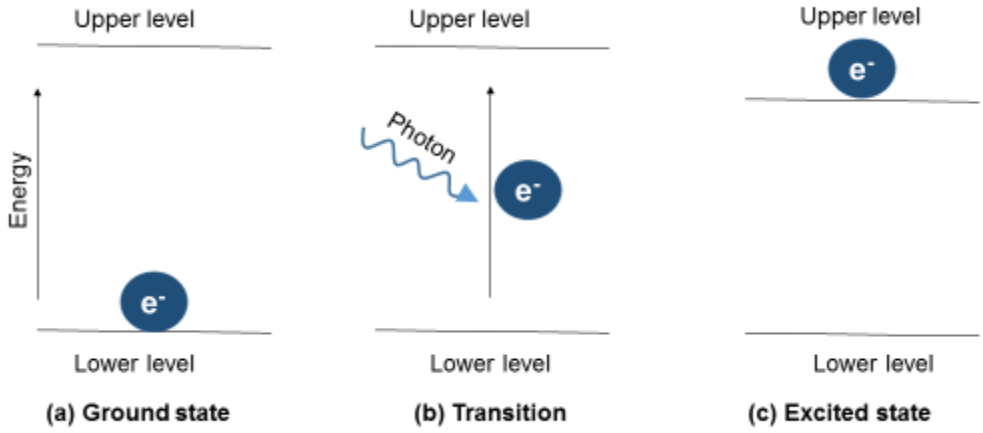

Figure 1.7: Absorption of a photon in spectroscopy.

The Beer-Lambert law states that the absorbance of a solution is directly proportional to the concentration of the absorbing species in the solution and the path length. Thus, for a fixed path length, UV/VIS spectroscopy can be used to determine the concentration of the absorber in a solution.

The wavelengths of absorption peaks can be correlated with the types of bonds in a given molecule and are valuable in determining the functional groups within a molecule. The nature of the solvent, the pH of the solution, temperature, high electrolyte concentrations, and the presence of interfering substances can influence the absorption spectrum. Experimental variations such as the slit width (effective bandwidth) of the spectrophotometer will also alter the spectrum. To apply

UV/Vis spectroscopy to analysis, these variables must be controlled or accounted for in order to identify the substances present [101].

Absorption spectroscopy is routinely used to calculate or compare concentrations of dispersed particles in solutions [102, 103] or for example, to estimate layers of graphene [104]. UV-Vis spectroscopy is also used in the semiconductor industry to measure the thickness and optical properties of thin films on a wafer. In this work, a spectrophotometer Cary 5000, which is seen in Figure 1.8 was used to measure the quality of dispersions and compare the exfoliation characteristics of the different solvents.

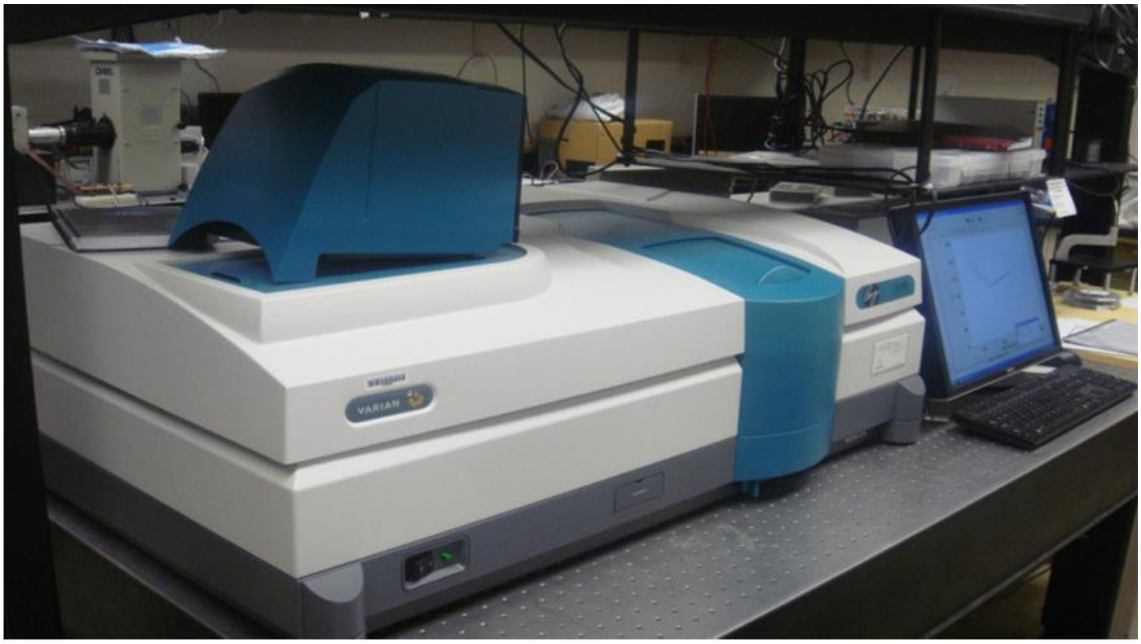

Figure 1.8: CARY 5000 Spectrophotometer used in our measurements.

1.3.3 Electrical Characterization

Electrical Characterization can be used to determine resistivity, carrier concentration, mobility, contact resistance, barrier height, depletion width, oxide charge, interface states, carrier

lifetimes, and deep level impurities. Current with respect to voltage (I-V) curves have been used to characterize our printed devices.

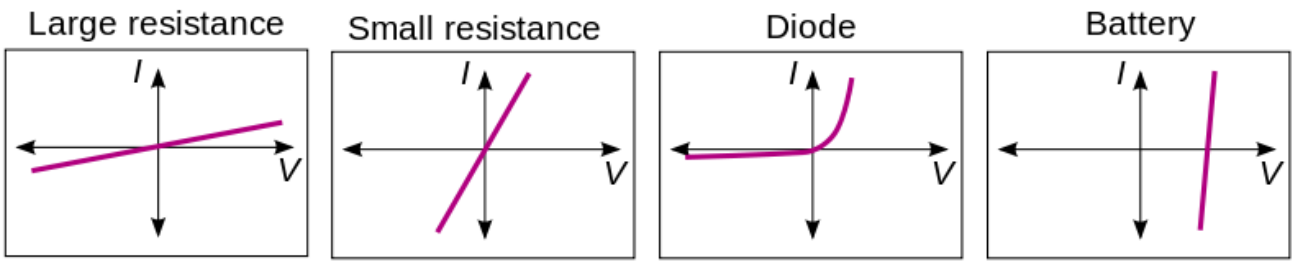

Figure 1.9: Types of IV curves.

An IV curve describes the relationship between an electric current through a circuit, device, or material, and the corresponding voltage, or potential difference across it. Being very simple, our IV curves demonstrate characteristics which are such of a resistor, which according to Ohm's Law exhibit a linear relationship between the applied voltage and the resulting electric current, where the slope of the line is the resistance. Geometric parameters may affect the resistance, in such a way that the specific characteristic of a material would be its resistivity, which accounts for any effect length or area may have on the resistance. Resistivity is the intrinsic property that quantifies how strongly a given material opposes the flow of electric current. The inverse of the resistivity is the conductivity of a material. Other types of IV curves would result in materials that do not obey Ohm's Law, such as diodes, memristors, and other devices, which do not show a straight line in their IV measurements, but may have instead curves, hysteresis, etc. (See Figure 1.9). An image of the Micromanipulator 450PM-B probe stage equipped with a HP precision semiconductor parameter analyzer 4156A used in this work is seen in Figure 1.10.

Figure 1.10: Micromanipulator 450PM-B probe stage equipped with a HP precision semiconductor parameter analyzer 4156A.

1.3.4 Raman Spectroscopy

Raman spectroscopy is a characterization technique that involves shining a monochromatic light source (i.e. laser) on a sample and detecting the scattered light. It provides information about molecular vibrations that can be used for sample identification and quantitation [100]. When this light that is shone on the sample, is scattered, most of it has the same frequency as the excitation source, this is known as elastic scattering or Rayleigh. But some amount of the light that is

scattered shifts in energy from the frequency of the laser because of interactions with the vibration of the molecules (see Figure 1.11). This shifted light is plotted and results in the Raman spectrum of the sample. Raman spectroscopy can be used for both qualitative and quantitative applications. The spectra are very specific, and chemical identifications can be performed by using search algorithms against digital databases.

In the case of the Raman spectra of graphite and graphene, numerous studies have been done in the hopes of understanding their characteristics and significance. For these materials, Raman spectroscopy can be efficiently used to monitor a number of layers, quality of layers, doping level and confinement in graphene nanostructures. Disorder can be monitored via the D peak. The fact that the G and 2D Raman peaks change in shape, position and relative intensity with number of graphene layers reflects the evolution of the electronic structure and electron–phonon interactions. [105, 106].

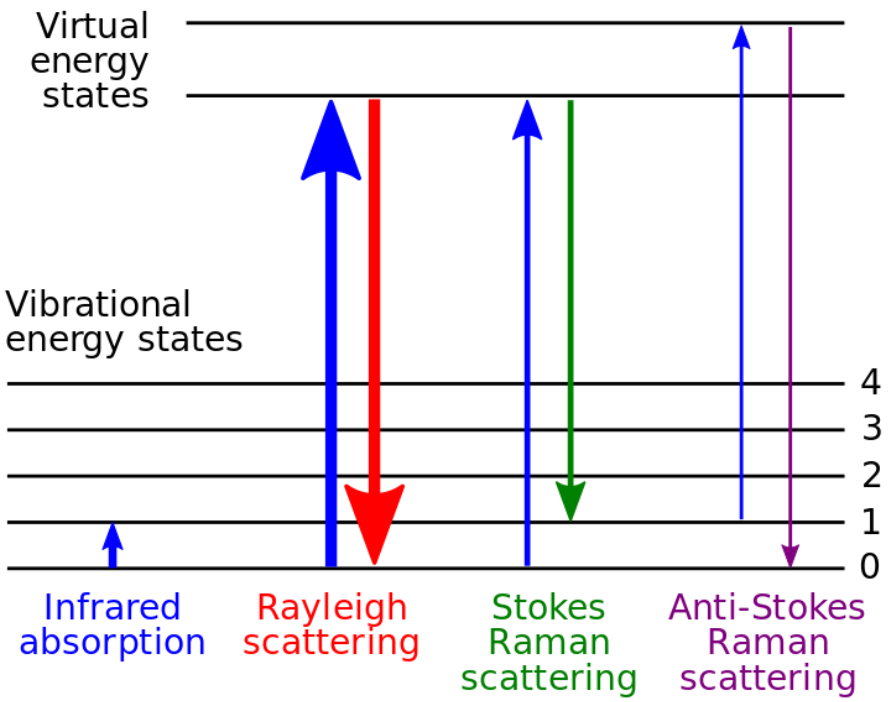

Figure 1.11: Energy-level diagram showing the states involved in Raman spectra.

Raman spectroscopy is able to probe disorder in graphene through defect-activated peaks. It is of great interest to link these features to the nature of disorder. It has been found that the intensity ratio of the D and D′ peak is maximum (~13) for sp3-defects, it decreases for vacancy-like defects (~7), and it reaches a minimum for boundaries in graphite (~3.5). This makes Raman Spectroscopy a powerful tool to fully characterize graphene [107]. Figure 1.12 shows an image of the Horiba Raman Spectrometer used in this work.

Figure 1.12: Horiba Raman Spectrometer used in our measurements.

1.3.5 Transmission Electron Microscopy Characterization

Transmission Electron Microscopy (TEM) is an analytical technique developed in the 1930's by Max Knoll and Ernst Ruska, for which in 1986, Ruska received the Nobel Prize of Physics. In TEM, an image is formed after the interaction of the illuminating source, in this case a

beam of electrons, and an ultra-thin layer of material. The image that is formed may be a diffraction pattern or any of several types of images on the fluorescent screen or photographic film.

The TEM is built around an electron column which can be divided into two principal subassemblies: the electron gun, or source of high-energy electrons, and the electromagnetic lenses, which are used to control the beam and thus generate an image. TEM typically operate at voltages exceeding 60 kV. The electron - ray path is analogous to the visible ray path in an optical microscope, except that the electrons follow a spiral path through the lens as they are focused, while light is focused through the lens in a plane. The interactions of the electrons as they strike the thin film specimen dictate the type of image that will be revealed. The interaction that allows to observe the structural detail in crystalline materials, is the diffraction of the electrons by the array of atomic planes in the specimen, which follow Bragg's Law. Bragg diffraction occurs when the radiation has a wavelength comparable to atomic spacing, and is scattered in a specular fashion by the atoms of a crystalline system, undergoing constructive interference. For a crystalline solid, the waves are scattered from lattice planes separated by the interplanar distance "d". Bragg's Law indicates that when scattered waves interfere constructively, they remain in phase since the difference between the path lengths of the two waves is equal to an integer multiple of the wavelength. The path difference between two waves undergoing interference is given by $n\lambda=2d\sin\theta$, where θ is the scattering angle (see Figure 1.13). When two beams with identical wavelength and phase interact with a crystalline solid are scattered off from two different atoms, the lower beam traverses an extra length of $2d\sin\theta$. Constructive interference then will occur when this length is equal to an integer multiple of the wavelength of the radiation.

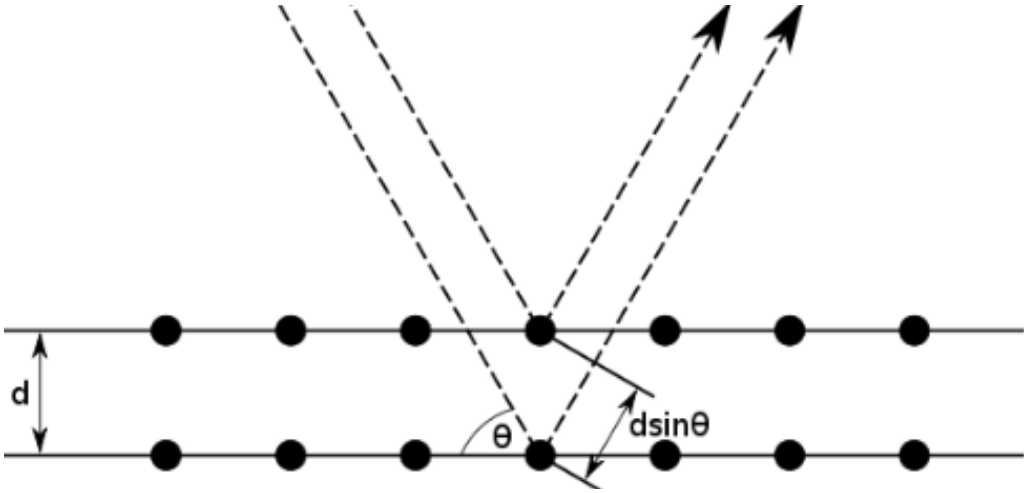

Figure 1.13: Bragg diffraction.

The required size for an imaging sample is around a 5 µm thick, 3mm diameter disk. This means that bulk specimens must be sectioned and electro thinned or ion milled to produce regions that permit the transmission of the electron beam. Electron transparent regions are typically less than 100 nm thick. Different sample preparation techniques exist, and TEM grids can also be used to support ultra-thin films and are useful for analysis of dispersed materials. In this work, the TEM analysis was done after printing on a grid and looking at the supported graphene flakes on the Cu wires.

Chapter 2:

Surfactant-assisted Dispersions

It needs to be recognized that the reliability and printing characteristic of any ink are not inherent properties of the formulation but are strongly dependent on the print – head and process architecture, requiring a holistic approach to the ink design [108]. A good ink should possess specific properties, such as viscosity η, density ρ, and surface tension [18] in order to be successfully printed, and these properties are often contrary to the solvents that seemed ideal for graphene dispersions, so a balancing act and more studies are needed to understand their effect. For example, a free droplet will try to adopt the shape with the lowest surface area, which is a sphere, and in the absence of other forces, that is what it will form. When the liquid is in contact with a solid surface, then we need to consider also the interface energy between liquid and substrate, so in that case, the equilibrium shape of the drop is going to be a spherical cap.

Most of the studies attempting to understand the mechanisms of drop generation and interactions have been based in identifying a number of dimensionless groups of physical constants [109, 110], and how the fluid mechanics of the process of printing are affected by them. The most useful numbers that describe these characteristics are Reynolds ($Re=v\rho a/\eta$), Weber ($We = (v^2\ \rho a)/\gamma$), Ohnesorge ($Oh = (\sqrt{We})/Re$), and $Z = 1/Oh$, where v is the velocity of the drop, ρ is the fluid density, "a" is the nozzle diameter, η is the viscosity of the fluid, γ is the surface tension of the fluid.

Great progress has been obtained in producing liquid-phase graphene dispersions, but efficient and reliable mass production for practical applications, still has many challenges to

overcome. The use of surfactants is well-known in the inkjet ink formulation. They are mainly used to stabilize the dispersion of particles in the medium, even in the case of systems with covalently bound dispersants. Another role of surfactants is the control of surface tension at the liquid – air interface. Here we have determined a way in which to utilize Ethyl Cellulose (EC), a cellulose in which some of the hydroxyl groups of the linear chain have been converted into ethyl groups, in order to engineer the viscosity η of the dispersions; we have also measured its impact on γ of the fluid. In prior work, while EC has been shown to act as a stabilizing polymer and surfactant to prevent nanoparticle agglomeration, we have found it is more effective to incorporate EC *after* the sonication process instead of *prior* to it. One of the obstacles to overcome for successful manufacturing of electronic devices, is to get rid of or diminish the residues that traditional solvents and surfactants employed for graphene exfoliation leave, even after extensive annealing, that disrupt the conductive network [33, 111].

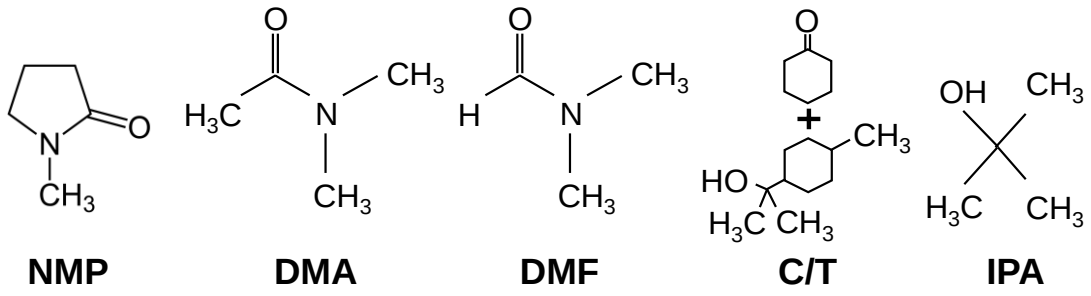

Figure 2.1: Five different solvents used for dispersion MoS_2 and graphite.

We have investigated five solvents (Figure 2.1) with different polarity (P_i) in order to formulate stable graphite and MoS_2 inks appropriate for printing. The solvents studied were: a) NMP (N-methyl – 2 pyrrolidone, P_i = 6.7), b) DMA (Dimethylacetamide, P_i = 6.5), c) DMF

(Dimethylformamide P_i = 6.4), d) mixture of Cyclohexanone/Terpineol (P_i = 4.5), e) IPA (Isopropanol, P_i = 3.9). Solvents with higher polarity values such as NMP, DMA, DMF (P_i value of 6.7, 6.5 and 6.4 respectively) have already been extensively investigated for graphite and MoS_2 dispersion; less toxic and more environment friendly solvents such as C/T and IPA were included in this work covering larger variations in solvent polarities. We have exfoliated Graphite Rod (GR), Graphite Powder (GP) and MoS_2 in these five solvents and they have been subjected to different sonication times, 0.5, 6 and 24 hours, and their absorbance patterns obtained to compare the amount of exfoliated nanoparticles. These studies will allow us to select the best solvent for each material (MoS_2 and graphene) so that we can prepare the ink with the right characteristics for printing.

2.1 METHODS AND MATERIALS

Viscosity Study. The five solvents used in this work were purchased from Sigma Aldrich and used as received, with the exception of the C/T mixture which was prepared at a ratio of 7:3 throughout the experiments. Different concentrations of solvents with 1 wt% to 6 wt% EC (Sigma Aldrich 200646) were prepared and viscosity values obtained. Contact angle measurements were done using a Ramehart 250 F4 standard goniometer and the substrate was SiO_2. MoS_2 was commercially obtained (Sigma Aldrich #69860), and in all the dispersions it was prepared with an initial concentration of 3 mg/ml, as was the dispersion for the Graphite Rod (Sigma Aldrich #496553) and graphite powder (Alfa Aesar #10131). After preparing the dispersions, they were sonicated for 0.5, 6 and 24 hours. A Branson 2800 bath sonicator was used for all the sonication in this work. *Characterization:* Optical absorption spectroscopy was conducted using a CARY 5000 spectrophotometer in quartz cuvettes with 0.3 ml volumetric capacity. Only supernatant liquid was used for absorption measurements. SEM microscopy was carried out in a Hitachi S-4800.

Whenever dispersion samples were drop cast on wafers, SiO_2/Si wafers with a 300 nm oxide layer were used. Electrical characterization was conducted using a micromanipulator 450PM-B probe stage equipped with a HP precision semiconductor parameter analyzer 4156A. *Printing*. The DIMATIX 2831 material printer from Fujifilm was used for the ink jet printing, where the ink cartridges were purchased from the manufacturer and had a volume of 10 pl and equipped with 200 nm syringe filters. The cartridges were comprised of 16 nozzles, where the nozzle diameter was ~ 21.5 μm. *Annealing*: All heat treatment was done on a hot plate at ambient pressure.

2.2 ETHYL CELLULOSE

The use of surfactants, as has been noted before, provides a crucial control of surface tension. If the system's surface tension is too high, ink may not move through the nozzle, or printing may be sporadic. If the surface tension is too low, the ink may leak out of the nozzle. The amount of surfactant will have an effect on stability, printability, and as-deposited wettability. Large amounts of surfactant can decrease the effective density of particles in the printed pattern, have an effect on the sintering and on the adhesion to the substrate. We have used EC to fine tune the viscosity while still allowing for the successful sintering and adherence to the substrate.

2.2.1 Viscosity

EC was added to the five solvents in different wt% from 1 to 6wt%. The addition of EC resulted in an increase in viscosity in all of them. For the five solvents we determined the necessary wt% of EC to obtain the recommended viscosity values for inkjet printing, which are close to 10 cP. It can be observed from Figure 2.2 that the viscosity values for C/T increased almost 15 times with the addition of EC; for example the viscosity of C/T increased from 2 cP to almost 35 cP with only 6 wt% addition of EC. This solvent needs the least amount of EC to reach the optimum

viscosity for printing (10 cP), followed by NMP and IPA (4 wt% EC), while DMA and DMF require the greatest addition at almost 6 wt% EC.

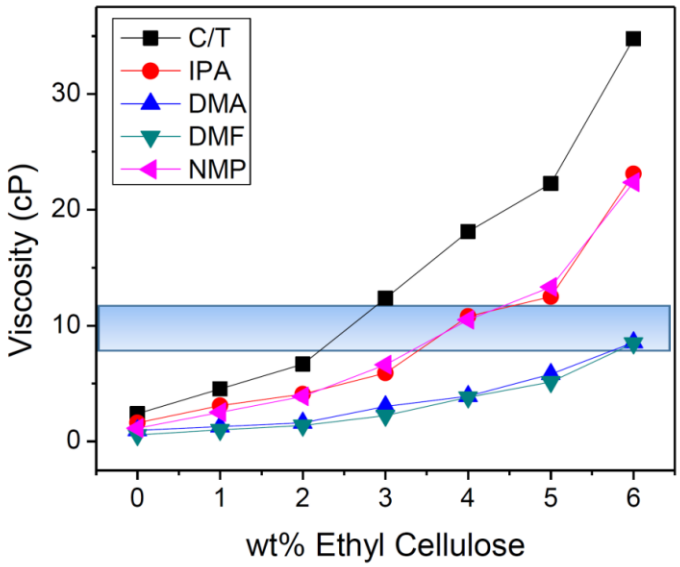

Figure 2.2: Change in viscosity with the addition of Ethyl Cellulose.

2.2.2 Surface Energy

Surface Energy has shown to be important, both for exfoliating layers and nanoparticles from bulk material, and for the impact it has on the fluidic properties of the printable ink. The surface energy relation between liquid, solid and gas interfaces is expressed by Young's equation $\gamma_S = \gamma_{SL} + \gamma_L cos\theta$, where γ_S is the surface energy of the solid, γ_{SL} is the interface surface energy, γ_L is the surface tension of the liquid, and θ is the contact angle between liquid-solid interface. Contact angles were measured with a Ramehart goniometer for the different concentrations of EC in all solvents on SiO_2 substrate. Figure 2.3 illustrates the steps used to measure the contact angle; Figure 2.3a shows the drop falling, Figure 2.3b shows the time at which the drop is in contact with the substrate and Figure 2.3c shows the spread of the drop on the substrate and the contact angle

it makes. The drop diameter was observed to be around 200 µm for C/T with 4 wt% EC as shown in Figure 2.3b.

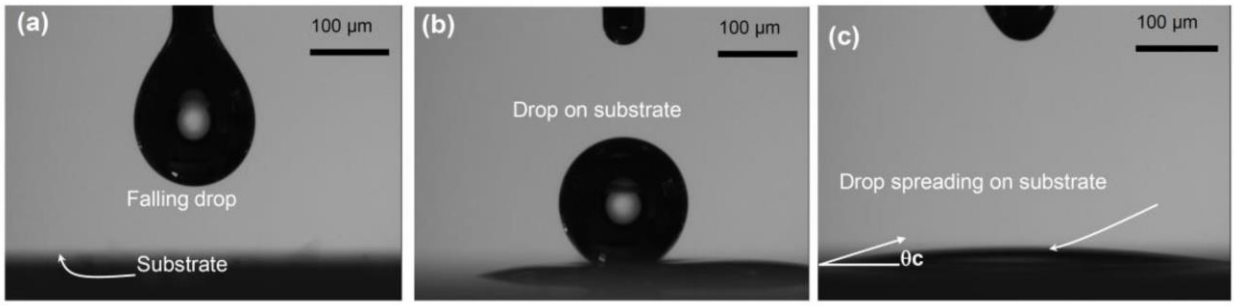

Figure 2.3: Sequence of steps for measuring the contact angle between fluid and the substrate.

Contact angle measurements shown in Figure 2.4a demonstrate increases for all five solvents with increasing EC concentration. The increase in θ_c of the solvent is likely to be due to the reduction of liquid surface tension with increasing EC concentration. It was evident from our investigation that the increase in θ_c with increasing EC concentration was much higher for IPA which has the lowest Pi, as compared to C/T with the next lower Pi; it was almost identical for NMP, DMA, and DMF which have similar Pi. IPA and terpineol have hydroxyl groups that form intermolecular hydrogen bonds, which as was mentioned above, is one of the parameters to consider for stable dispersions. These hydrogen bonds cause the molecules to "stick" together and act as if they had a higher molecular weight. DMF and DMA have very similar structures and Pi values, with their only distinct feature being the hydrogen bond in DMF that is replaced with a methyl group in the DMA; this may result in a difference in the exfoliation, but almost no difference in their viscosity behaviour is observed. From the data shown in figure 2.4, we see that there is an insignificant change in contact angle with the addition of EC for solvent NMP, which

is also the same behaviour noted for DMF and DMA. This is in contrast to IPA and C/T where the contact angle changed more significantly as more EC was added. Furthermore, the jetting properties and drop formation required for printing depend on both viscosity and surface energy.

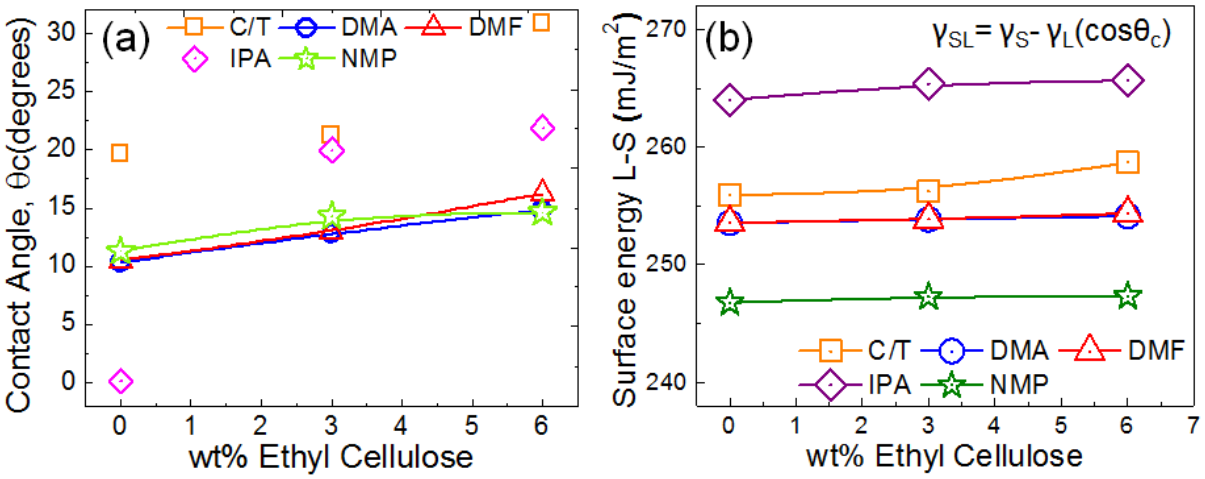

Figure 2.4: a) Contact angle change with respect to wt% EC and b) change in interface surface energy.

The surface energy relation between liquid, solid and gas interfaces can be expressed by Young's equation $\gamma S = \gamma SL + \gamma L cos\theta c$, where γL is the surface tension of the liquid, γSL is the surface energy between solid to liquid interface, and γS is the surface energy of the solid [32, 72, 112]. We have calculated the surface energy of the liquid – solid interface (γSL) from the measured θ_c of different solvents. For example, for IPA 3 wt% EC, θ_c was measured ~ 19°, and given the surface energy for SiO_2 ~287 mJm^{-2}, from the Young's equation we obtained an interface surface energy value of 265 mJm^{-2}. It is important to note that for γL, we assumed the initial surface tension values for the respective solutions, i.e., γL values for IPA, C/T, DMA, DMF and NMP are 23 mJm^{-2}, 33mJm^{-2}, 34 mJm^{-2}, 34 mJm^{-2} and 41 mJm^{-2}, respectively. Figure 2.4b shows the

variations in the liquid-solid surface energies with increasing EC concentration which indicate the interface surface energy between the liquid drop and the SiO_2 substrate was not modified by more than 5% with the addition of EC, which is likely due to the substantially larger substrate surface energy ~287mJm^{-2} for SiO_2. From the measured contact angle and using Young's equation, we have determined the change in surface energy values.

2.3 MoS_2 DISPERSIONS

After the η and γ are optimized through the addition of EC, we proceeded to formulate dispersions of 2DLMs. Here we discuss the results related to the MoS_2 dispersion which was prepared using MoS_2 powder and adding 1 wt% EC for controlling dispersion viscosity. Two sonication times were investigated (0.5 hours and 6 hours) followed by a 24 hour stabilization period. Optical absorbance spectroscopy was used to investigate the MoS_2 dispersion (figure 2.5(a)) which indicates the absorption increased as the sonication time increased, due to particle size and/or layer number reduction. This is also visualized by the appearance of the vials in the inset of figures 2.5(b-f), where the solution appears darker with the greater sonication time for the solvents investigated.

The C/T absorbance was greatest, followed by DMF, NMP, DMA, and IPA. The characteristic peaks for MoS_2 at 608 nm and 665 nm [113, 114] were observed in C/T and NMP, and mildly in the other solvents, which is related to excitonic behavior in ultra-thin nanosheets, and we will report on this characteristic in greater detail in forthcoming work [115]. Our aim in conducting this study was to look at differences between "low" sonication exposure (as noted by the 0.5 hr. samples) and "high" exposure (as noted by the 6 hr. samples).

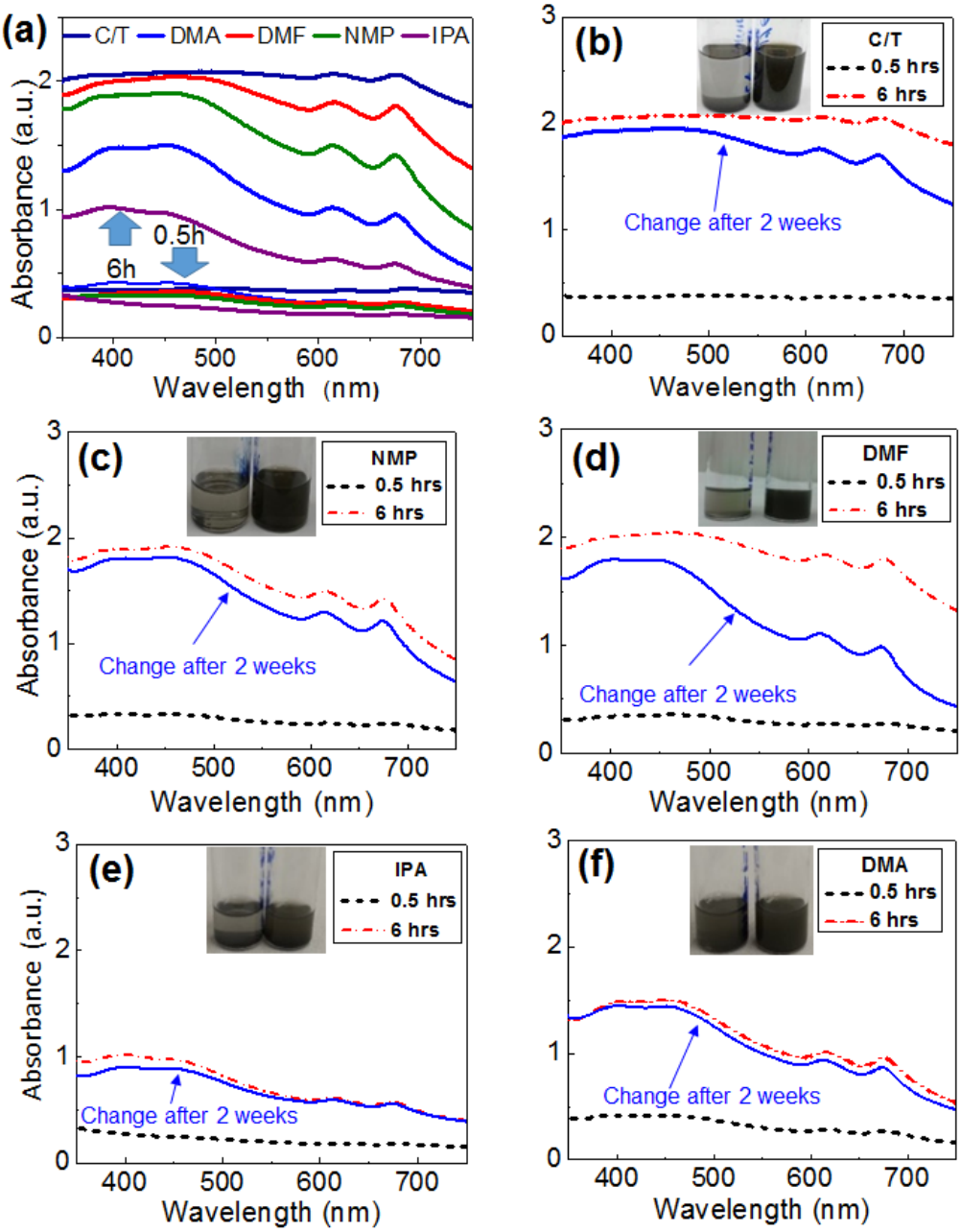

Figure 2.5: a) Absorbance spectra of MoS_2 in the five different solvents sonicated for 0.5 and 6 hours. b) to f) Absorbance spectra of shown individually for each of the give solvents including the absorbance after 2 weeks.

We believe that the important fact elucidated from our analysis here is that the relative absorbance generally seems to increase over the entire spectral range considered (350 nm – 800 nm) for all the solvents at the high exposure level, as illustrated by the data in figure 2.5(a)-(f) for MoS_2. Hence, we infer that the dispersability and exfoliation of MoS_2 increases for the 6 hr. sonication or higher exposure condition, compared to the lower exposure condition of 0.5 hr. The stability of the dispersions over time was also explored for the 6 hour sonicated samples, which indicated a high degree of suspension stability for DMA followed by IPA, NMP, C/T, DMF (see figure 2.5(b-f)). In the case of DMF, a pronounced decrease in the absorbance after a two-week "settling" period was observed, possibly due to particulate re-agglomeration.

2.4 GRAPHITE DISPERSIONS

Two sources of graphite were used as the starting templates for generating the graphite/graphene dispersions, namely commercially available graphite rod (GR), as well as graphite powder (GP). The dispersions were prepared and sonicated in each of the five solvents for 6 and 24 hours, and the effect of the EC was analysed. SEM, optical spectroscopy and electrical measurements were done to compare the graphite dispersions.

2.4.1 SEM microscopy

In order to look at the initial structure of the two materials, the graphite rod was broken into small pieces and both were placed on carbon dots on the SEM. Figure 2.6(a) depicts a scanning electron micrograph (SEM) of the broken GR pieces, as purchased from the manufacturer (inset), with its layered structure (see arrow in figure 2.6(a)). The GR flake distribution varied from a few microns to almost 50 μm. In the second case of the GP, the SEM micrograph in figure 2.6(b) reveals large particles (see black arrow) with particle distribution ranging from 100 μm to 700 μm,

~ 10X larger than the flake size distribution in the GR. We experimented with two forms of graphite, one that is an untreated or "natural" graphite (graphite rod), and the other is an artificially compressed graphite powder (GP). In the graphite rod, the layered structure can be clearly visualized through the platelet-like lamellar structure observed (figure 2.6(a)), while the graphite powder is composed of a carbon where this platelet-like structure is non-evident, and the material resembles solid, "dense pebbles" (figure 2.6(b)). Given the highly compressed nature of the GP in figure 2.6(b), the higher density and absence of interlayers is likely to inhibit the penetration of the solvent to effectively exfoliate the material using solution- based dispersion.

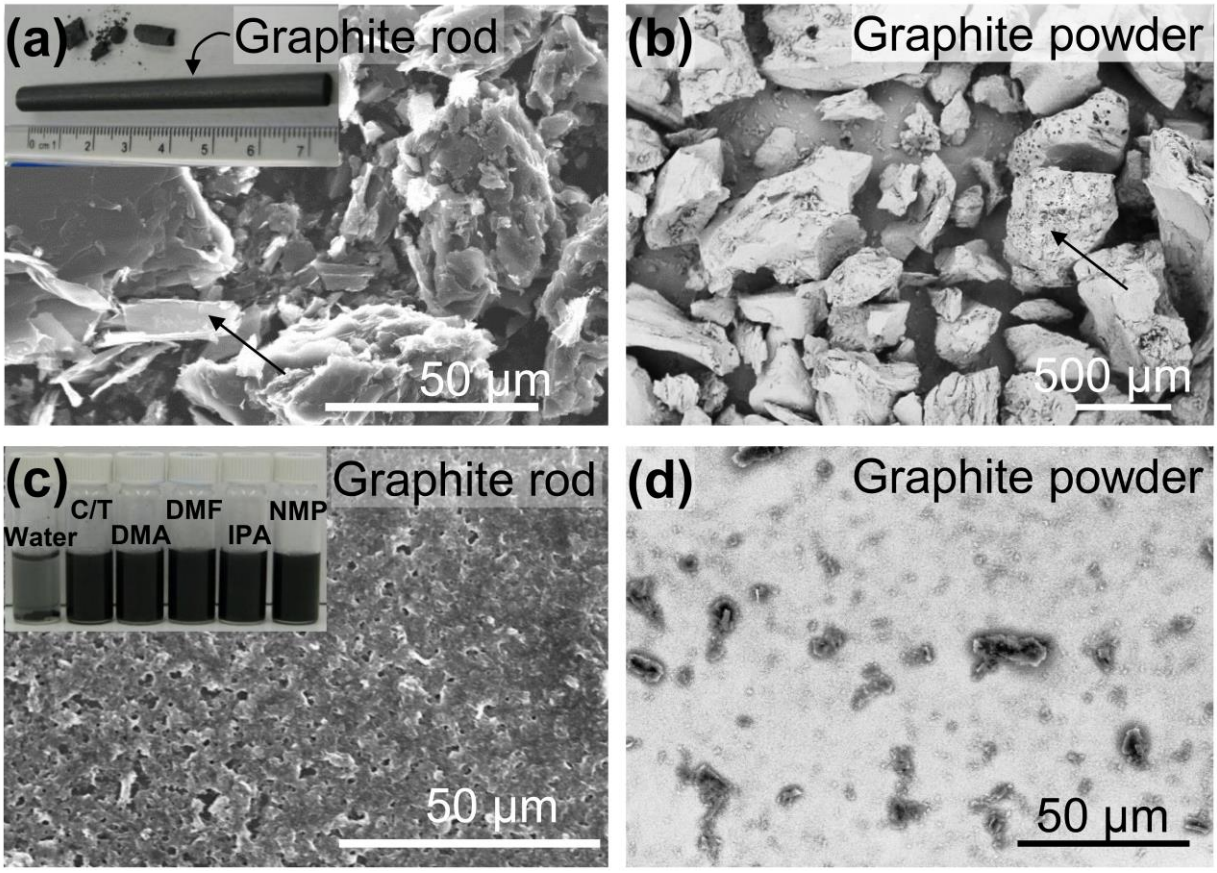

Figure 2.6: SEM micrograph of a) GR inset showing graphite rod pieces as received. b) Graphite powder c) GR dispersion in NMP drop casted on SiO_2. Inset shows dispersions in the five solvents. d) GP dispersion in NMP drop casted on SiO_2.

The GR was successfully dispersed in all five solvents by sonicating for 6 hours, as shown by the vials in the inset of figure 2.6(c), including water. Despite its benign nature, even the water-based graphite dispersion showed discoloration indicating the exfoliation of graphite flakes occurring, to some extent, in water. The SEM micrograph of the drop-cast GR dispersion in NMP (on SiO_2/Si) is shown in figure 2.6(c), which resulted in small pinholes in the film, but in contrast, a very sparse distribution of randomly distributed particles in the GP film was observed, as shown in figure 2.6(d). Thus, the GR flakes seem to form a continuous film (figure 2.6(c)), which was not observed for the GP.

2.4.2 Role of Ethyl Cellulose

Ethyl Cellulose has been used in the coatings industry for several decades and known to be a rheology modifier [116]. Here we explore its role in the ink formulation process of our 2DLMs. In prior work, EC has been used as a dispersant surfactant for inkjet printing of 2DLMs [84], where it is usually added to the solution mixture before sonication in order to promote EC intercalation deep into the graphite layers and to prevent particle aggregation [21, 117]. However, this process reduces the effective sonication power density experienced by individual particles, and consequently reduces flake exfoliation.

In our study we have demonstrated that adding EC to the GR before sonication resulted in much larger particle size, as shown by the black arrow in Figure 2.7a of the optical micrograph image of the drop-cast surface, which is likely due to the reduction of the effective sonication power density. This is in contrast to the image in Figure 2.7b where no large particles are detected at the same magnification. The optical spectra in Figure 2.7c also corroborates the higher density dispersion for the case without the EC, given the higher optical absorbance in this case. This suggests the EC acts as a "shock absorber" in the sonication process and reduces the effectiveness

of the exfoliation. In light of this, our results indicate that EC should be added after sonication to prevent particle agglomeration, and improve suspension stability, while at the same time noting its importance in tuning the viscosity for optimum ink printability.

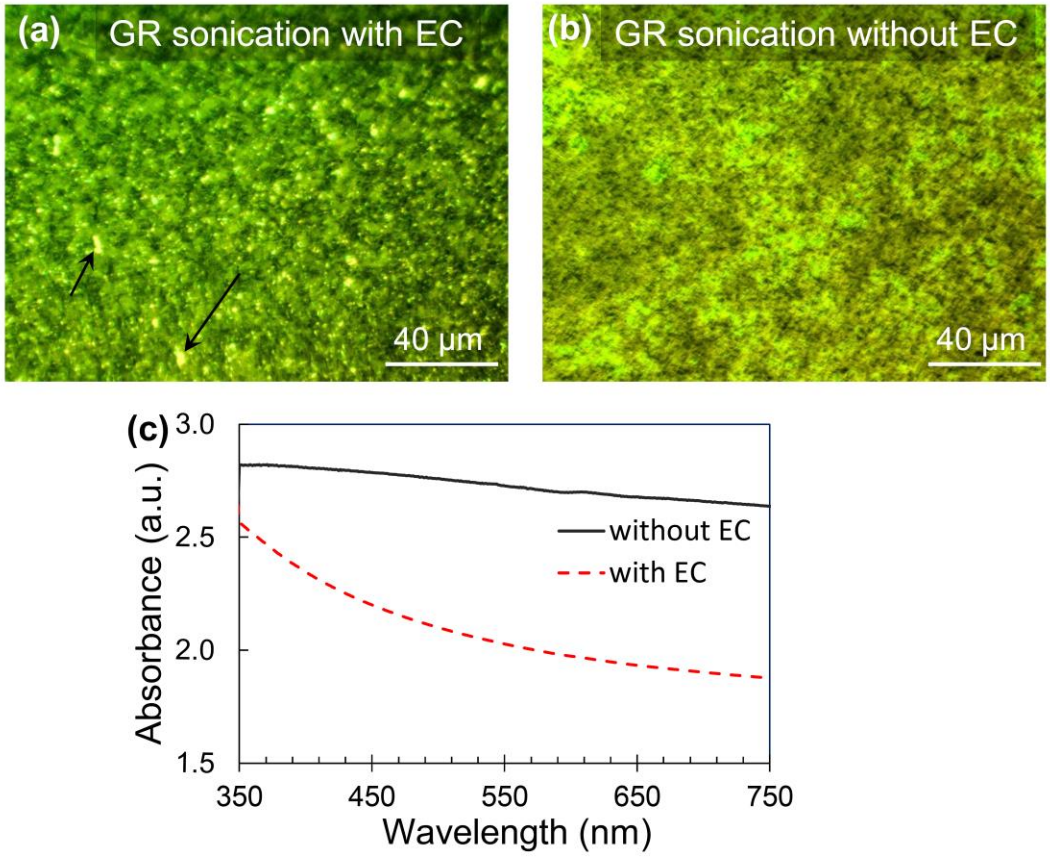

Figure 2.7: a) Optical image of GR dispersed in NMP and sonicated for 24 hours with 4wt%EC added b) Optical image of GR dispersed in NMP and sonicated for 24 hours without EC added. c) Comparison of absorbance for GR dispersed in NMP sonicated 24 hours with and without EC.

GR and GP were dispersed at concentrations of 3 mg/ml in the five solvents studied and sonicated for 6 and 24 hours and absorption spectroscopy was used to evaluate the dispersions, and the results are shown in figure 2.8. A higher dispersion of nanoparticles was obtained as the

sonication time increased for both starting materials; however, the range of absorption was very different as can be seen in the figure. Optical absorption spectroscopy for the GR and GP suspensions (without EC) in NMP are shown in figure 2.8, for sonication times of 6 hours and 24 hours. The GR suspension exhibits higher absorbance, and hence a higher concentration dispersion, at both sonication times compared to even the 24 hour sonication of the GP. We believe that the layered structure of the graphite rod results in a higher concentration of nano-dispersed particles in solution, and consequently a continuous film morphology results after the drop-casting process. This result comprehensively demonstrates that the GR is a useful starting template for formulating inks for ink-jet printing, given its layered structure in contrast to the GP. For this reason we have chosen GR as the raw starting material for formulating our dispersions for ink-jet printing, which we report on from hereon.

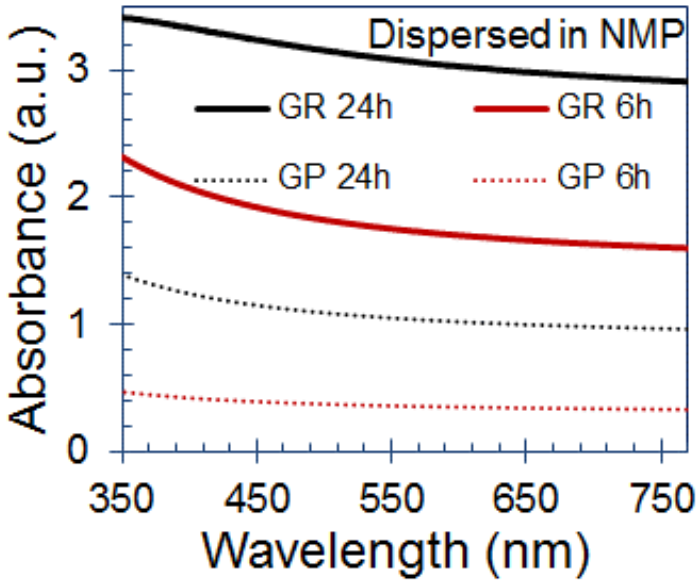

Figure 2.8: Absorption spectra of GR and GP dispersed in NMP and sonicated for 6 and 24 hours.

Figure 2.9 shows the variation in the optical absorbance spectra for the GR, where the NMP and DMF yielded a higher optical absorbance in comparison to all of the other solvents, a signature of the higher dispersion density in this case. These results indicate that the layered structure of the GR is more likely to have the van der Waal bonds broken and produce the desired nanoparticles than the GP.

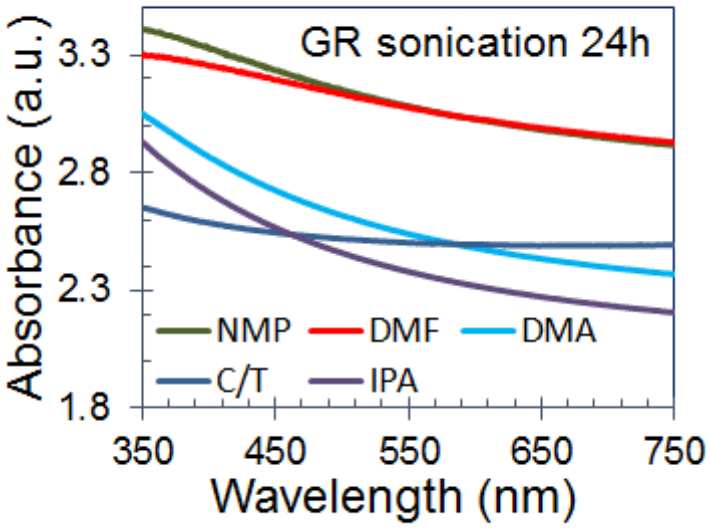

Figure 2.9: Absorbance of dispersions in five solvents for GR after being sonicated for 24 hours.

2.4.3 Electronic Properties and Morphology Characterization of 2D-Graphite Dispersions

GR dispersions were drop-cast onto SiO_2 substrates and annealed at 350 °C for 60 min and their electronic transport properties measured. Illustrated in figure 2.10 is an I-V characteristic of the GR dispersion in all five solvents, while the inset depicts the GR film resistance. Using two-terminal measurements, the GR dispersion in DMF exhibited the lowest resistance (1.6 KΩ)

compared to C/T which yielded the highest resistance (18 KΩ) for the same electrode spacing and approximate thickness.

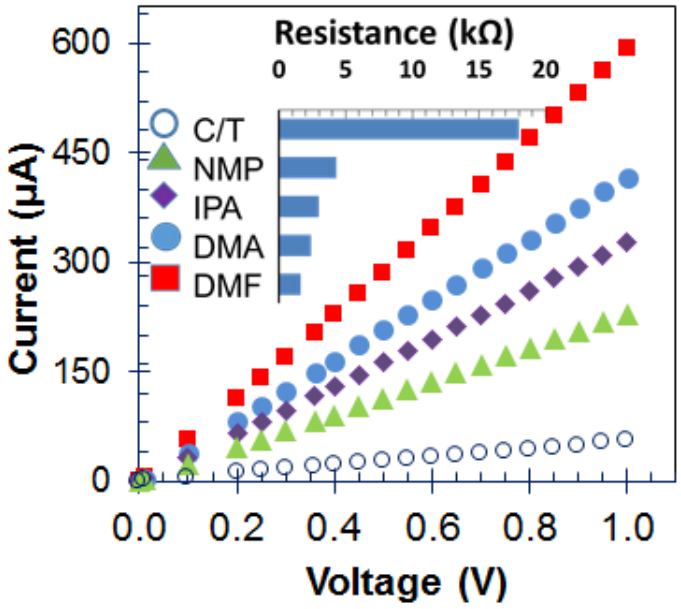

Figure 2.10: I-V curves of GR dispersed in five solvents after being drop cast on SiO_2/Si wafer and annealed for 1h at 350°C.

The image in figure 2.11(a) is indicative of a uniform film morphology for the DMF sample, unlike the NMP sample shown in figure 2.11(b), which exhibited a rougher and more non-uniform film morphology. From our initial observations, we have found that the drop-cast samples from the C/T dispersion appeared to form a non-uniform film. The non-uniform film morphology is likely the reason for the high resistance observed in this case. While the GR dispersed in DMF exhibits the lowest resistance in drop-cast films compared to other solvents, it requires the addition of ~ 6 wt% of EC compared to ~ 4 wt% required for NMP to yield optimum viscosity and printability (10 cP). For this reason, the dispersion of GR in NMP was used in the ink preparation

for printing given its higher particle dispersion as deciphered from optical absorption spectroscopy data.

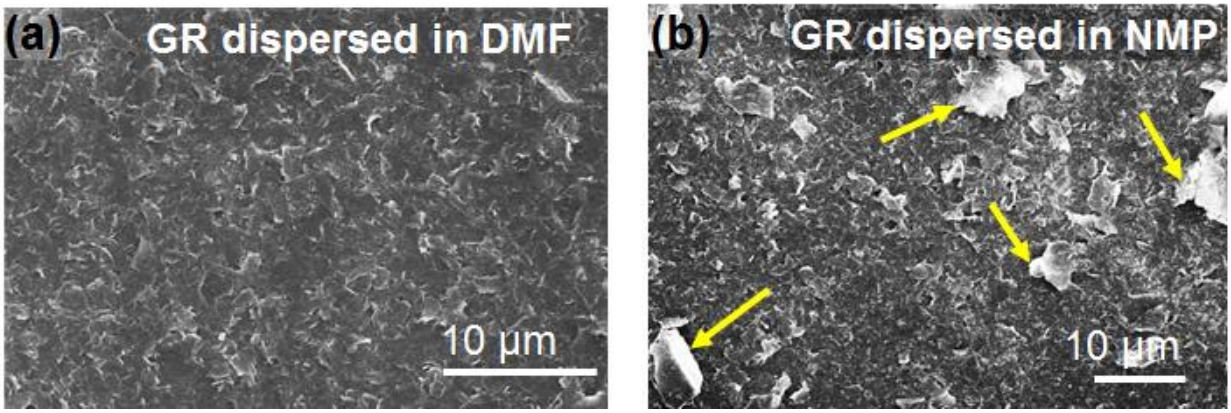

Figure 2.11: a) SEM micrograph film resulting from dispersion of GR in DMF. b) SEM micrograph film resulting from dispersion of GR in NMP.

2.4.4 Ink-jet Printing of 2D-Graphite Dispersions

Since a particle size below 200 nm is necessary to avoid nozzle clogging in our ink-jet printer, the dispersion (GR+ NMP solvent + EC) was filtered using a 0.2 µm syringe filter. Electronic transport measurements were conducted for the unfiltered and filtered inks as shown by the I-V characteristic in figure 2.12. Resistance values obtained for the filtered and unfiltered ink were 9.6 kΩ and 4.3 kΩ, respectively. While the filtered ink exhibited a higher resistance, this is not surprising due to the removal of more graphite precipitates during the filtration process. The top inset in figure 2.12 shows the relatively dark black color of the filtered ink in the vial, which is suggestive of a high concentration nanoparticle dispersion, while the bottom inset shows the relatively smooth surface morphology of the drop-cast ink onto SiO_2 that explains its reasonable electronic transport characteristics.

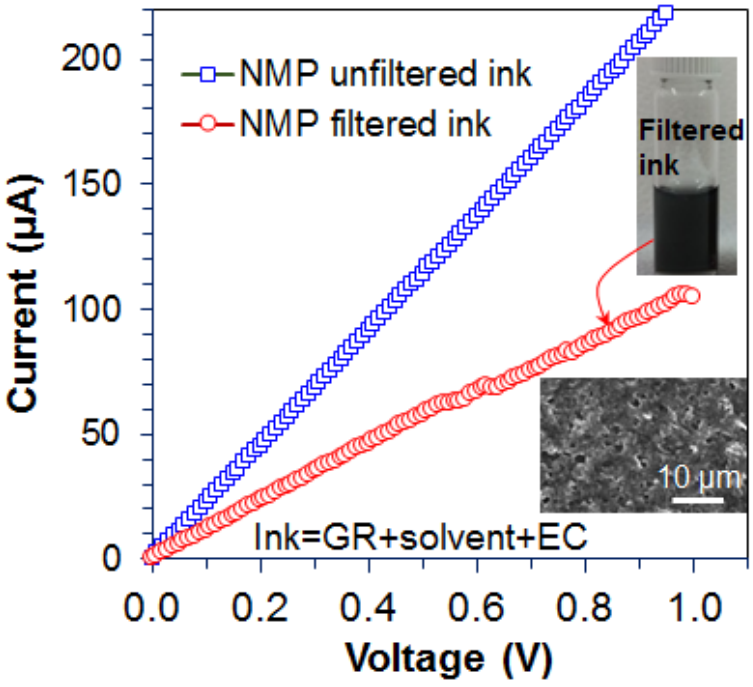

Figure 2.12: a) I-V curve of filtered and unfiltered GR ink.

Ink-jet printing of our 2D graphite ink was performed using a DIMATIX 2831 ink jet printer, which utilizes the micro-electro-mechanical (MEM)-based piezoelectric actuation mechanism. The NMP ink was successfully printed onto SiO_2/Si substrates, as shown in figure 2.13(a) which represents an array of ink-jet printed lines of graphite formulated NMP-based inks. Figure 2.13(b) shows the high-magnification optical micrograph of two printed lines on the SiO_2 substrate with a line-width of ~ 240 µm. This image illustrates the ink solution is concentrated in the center of the line due to the well-known Marangoni effect [32, 85], in which nano-dispersed ink particles tend to move towards the higher concentrated regions.

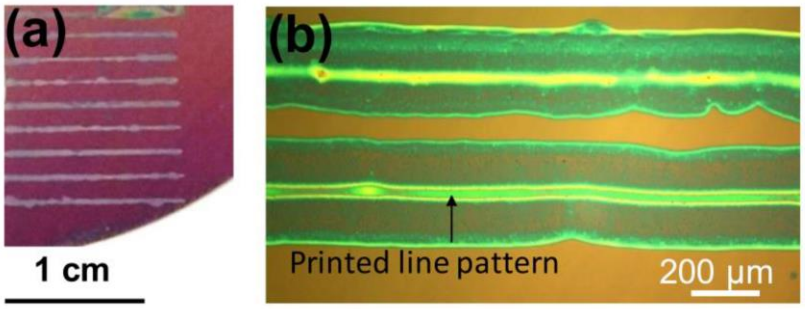

Figure 2.13: a) Digital image showing printed lines patterned with the prepared ink on SiO_2 substrate. b) Optical image of SiO_2 substrate with printed pattern.

As stated earlier, the ink fluidic properties are represented by the Reynolds, Weber, and Ohnesorgh numbers. The ink fluidic properties can be represented in a plot of *Re* versus *We*, (see figure 2.14) which illustrates the impact of γ, ρ, η on the ink-jetting characteristics. The fluid position on the map can be modified as indicated by the arrows with an increase in the v, ρ, η, or γ. Furthermore, this plot can define optimum printing regions by specifying inadequate drop dynamics regions, such as viscous, splashing, satellite drop, and insufficient energy for drop formation, as shown in figure 2.14. Through our experiments, we clearly see that our inks are well within the printable fluid region (see red dashed oval in figure 2.14) for optimum printing for the synthesized dispersion of GR in NMP. The combination of η and γ for our dispersions has resulted in printable inks with *Re* from 1.7 to 2.2 and *We* of 48 to 90, close to the limit of printable fluids. Results from previous investigations have also been mapped onto this plot for comparison [18, 32, 83, 110]. In some of them the inks were clearly inside the "printable" region, while others are further from the boundaries. It should be noted that the ink position on the fluidic property plot can also be modified by changing printer parameters, such as firing voltage, jetting waveform,

standing time, cartridge and substrate temperature, to some extent, which can provide another degree of freedom for potentially targeting the ink properties toward the printable fluid regime.

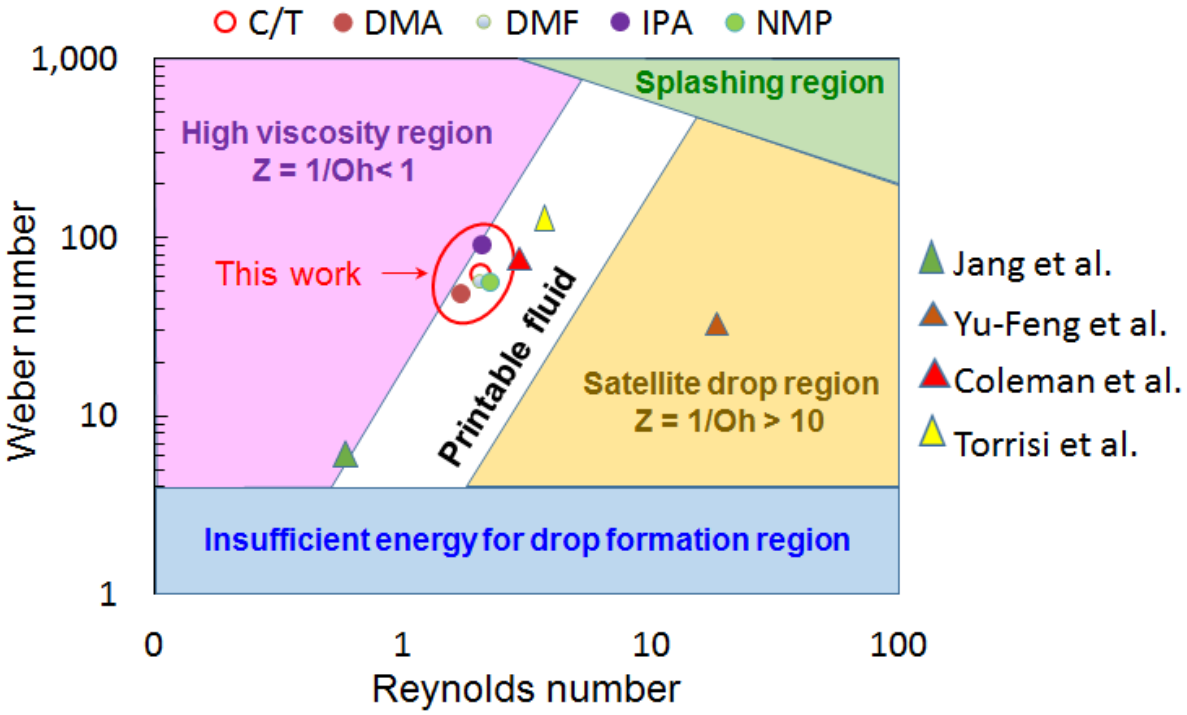

Figure 2.14: Ink fluidic property plot, illustrating the effect of the Reynolds number and the Weber's number on the ink fluidic properties. This indicates different regions for fluid mechanics, and the optimal region for stable drop formation and jettability.

Chapter 3:

Optimization of Printing Parameters

In this work, we have conducted a systematic investigation of the ink-jet printing parameters that sheds insights into the characteristics of the printed features, and we have successfully utilized these inks for fabricating practical devices that display unique characteristics, specifically, the ability to deliver ultra-high levels of power using ink-jet printed graphite resistors. We have also determined that the active nozzle number, printing passes, and annealing conditions have an important role to play in determining printed line resolution, as well as the morphological and electronic transport characteristics of the printed graphene features, where the inks are generated via sonication of the bulk graphite crystal. Here the inks are dispersed drop-by-drop in pico-liter volumes using drop-on-demand ink-jet printing technology, to construct macro-scale device architectures onto a wide range of substrates, from rigid to flexible and transparent.

3.1 METHODS AND MATERIALS

Materials: The ink used in this work was prepared by sonicating commercially available graphite rod pieces (Sigma Aldrich #496553) at a concentration of 6mg/ml in N-methyl-2-pyrrolidone (NMP) for 24 hours. After the sonication, 4%wt Ethyl Cellulose (EC) (Sigma Aldrich 200646) was added to the dispersion in order to obtain the optimum printing viscosity, and sonicated for another 4 hours. A Branson 2800 bath sonicator was used for all the sonication done in this work. The ink was separated after allowing the dispersion to stabilize overnight and selecting only the supernatant to avoid any precipitates that may contain bigger particles. Then, the cartridge was

filled. *Printing*. The DIMATIX 2831 material printer from Fujifilm was used for the ink-jet printing, where the ink cartridges were purchased from the manufacturer and had a volume of 10 pl. The cartridges comprised of 16 nozzles with a nozzle diameter of ~ 21.5 µm. All heat treating was done on a hot plate at ambient conditions. The printing conditions were varied in order to study the effect of the number of active jetting nozzles, as well as the number of passes. The platen on the printer was always heated at 60°C. *Characterization:* SEM microscopy was carried out in a Hitachi S-4800. The TEM analysis was conducted using a TEM 2100F field emission gun. The Raman data was obtained using a Horiba LabRAM HR Evolution where the excitation laser wavelength used was 532 nm. Electrical characterization was conducted using a micromanipulator 450PM-B probe stage equipped with a HP precision semiconductor parameter analyzer 4156A. Profilometer measurements were performed on the Brocker Dektak XT Stylus Profiler. *Substrate:* SiO_2/Si wafers with a 300 nm oxide layer and polyimide substrates were used for drop casting and printing. In the case of the polyimide, it was placed on top of Si substrate in order to hold it.

3.2 Effect of Number of Nozzles used for Printing

A stable solute dispersion is critical for a good performance of a printing ink, and this is obtained by controlling the solution's viscosity, density and surface energies [28, 85, 118]. Graphite dispersion in NMP with 4wt% EC was prepared considering viscosity and surface energy requirements for DIMATIX printer and reported in our earlier work [119]. Initially we demonstrate the effect of printing varying the number of nozzles used for printing (out of the 16 nozzles in a cartridge). Figure 3.1a shows the DIMATIX cartridge which consists of two components: fluid module (bag, valve, pressure system) and jetting module (MEMS jetting structure, heater, thermistor, electrical connection, fluid connection). Figure 3.1b represents a closer view of the jetting module which has 16 nozzles linearly spaced with 254 µm distance (dashed red color region

at bottom) and electrical connection array at the top of the image. Each individual nozzle with 23 µm in size can be seen in Figure 3.1c.

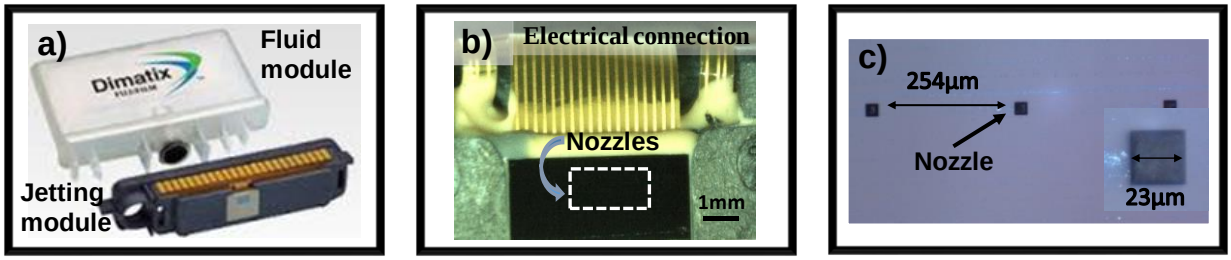

Figure 3.1: a) Dimatix Cartridge b) Close up of Jetting Module. c) Image of nozzles showing nozzle distance and size.

After obtaining a stable dispersion of 2D graphene as detailed earlier, in Chapter 2, where we engineered the dispersion viscosity through the addition of surfactant EC in N-methyl-2-pyrrolidone (NMP) to prepare optimal dispersions [120].

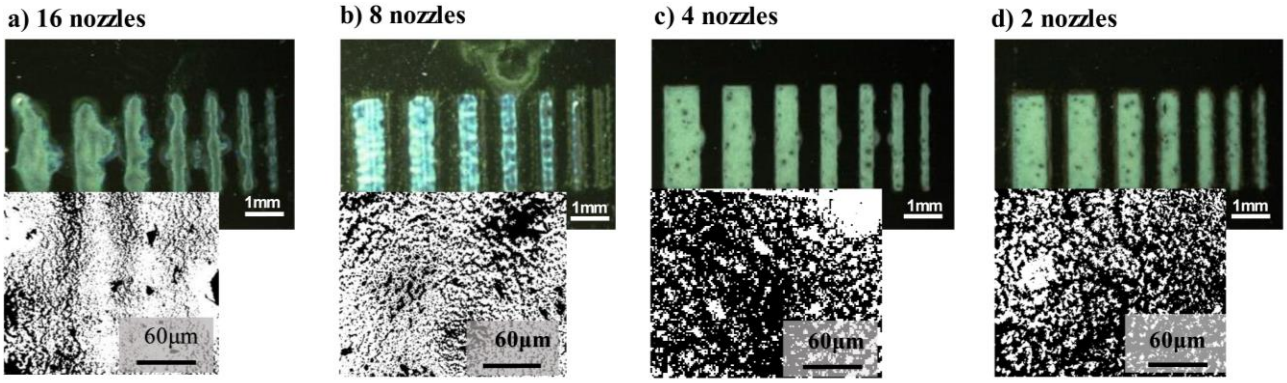

Figure 3.2: Printed line arrays with a) 16, b) 8, c) 4, and d) 2 nozzles. The printed array consisted of seven parallel lines that were 3 mm in length and spaced 0.8 mm apart, and the line width decreased from 1 mm to 0.1 mm. The insets at the bottom left of (a)-(d) show binary images used to calculate graphene content.

In Figure 3.2, the effect of nozzle number on the printing resolution is provided, where an array of lines with 15 passes was printed on SiO_2/Si substrates using 16 (maximum for cartridge), 8, 4 and 2 nozzles, and annealing was conducted for 1 hour at 300°C. As can be seen in Figure 3.2a-(d), the line edge resolution and uniformity of the printed arrays improved as the number of active nozzles decreased from all 16 firing (Figure 3.2a) to only 2 active nozzles printing (Figure 3.2d). Printing with all 16 nozzles resulted in non-uniform line edges due to excessive volume of ink delivered that likely leads to ink spreading on the substrate, compromising line resolution.

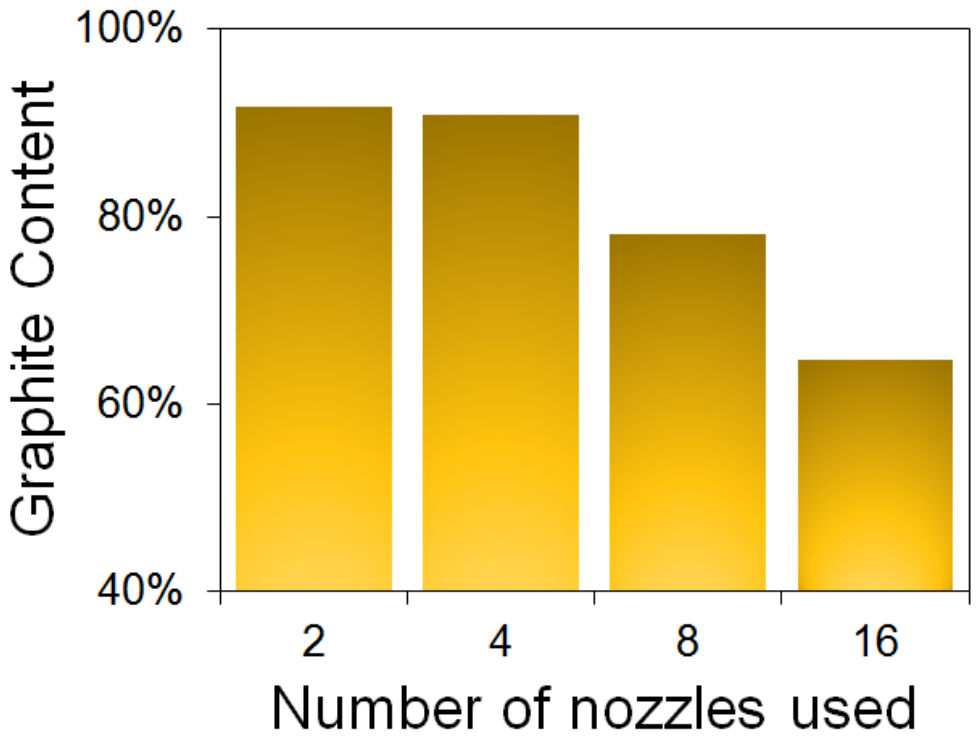

Figure 3.3: Graphite content depicted quantitatively in as a function of the active nozzle number.

Besides the edge resolution, the graphite content was quantified by converting the obtained optical images to binary format, as illustrated at the bottom left images in insets of Figure 3.2a–(d), where the black regions represent graphite, and the white regions indicate the absence of graphite. This shows that the content of graphite is maximized when the number of active nozzles

used is between 2 and 4, and it is least when all 16 nozzles are firing. Figure 3.3 quantifies this change in graphite content as a function of the number of active nozzles. These results validate that the homogeneity of the graphite nanomembrane distribution and coverage increases as the number of active nozzles was reduced from 16, 8, 4, and 2. Figure 3.3 shows the graphite content to be ~ 90% and unaltered between 4 and 2 active nozzles.

We then proceeded to conduct 2-terminal current-voltage (I-V) measurements on the printed graphite films which were formed using 2 and 4 nozzles. Both of the samples exhibited linear Ohmic characteristics, as shown in Figure 3.4, where the resistance in the 2 nozzle case was calculated to be 600 kΩ, which was 4X lower than the 4 nozzle case; printing with 8 or more nozzles yielded poor electronic transport characteristics, which is consistent with the poor film homogeneity and uniformity we observed (Figure 3.2a-(d)) of the printed lines with increasing nozzle number.

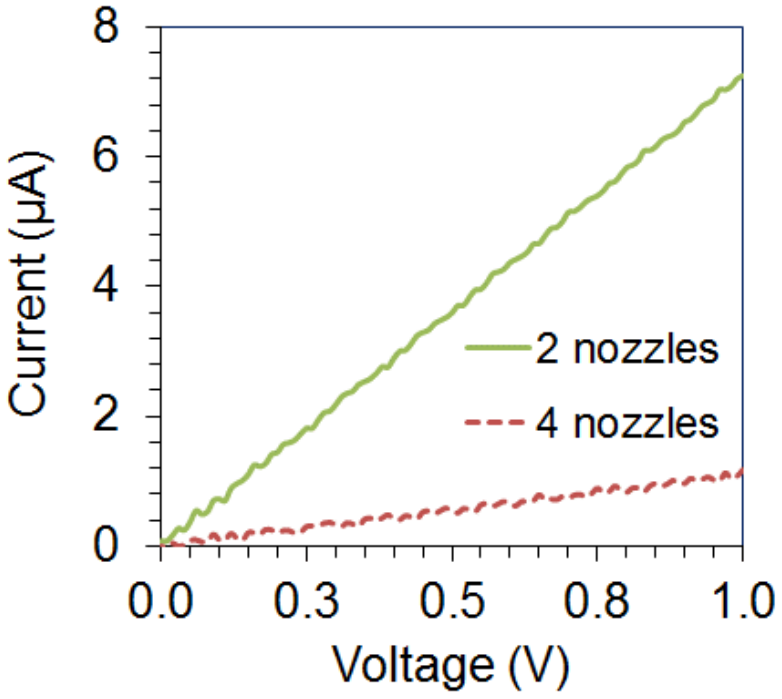

Figure 3.4: I-V measurement of printed lines using 4 and 2 nozzles.

While keeping the number of printing passes fixed, the *R* was seen to decrease rapidly as the printed line width increased, as shown in Figure 3.5. Graphite films printed with 2 nozzles, exhibited consistently lower *R* values compared to 4 nozzles for all of the line widths explored here. Above linewidths of 0.5 mm, the *R* change remained unchanged with increasing line width, as shown in Figure 3.5. The low *R* values noted in the 2 active nozzle case compared to the 4 nozzle case may have to do with the reduced ink volume deposited on the substrate which allows the solvent to evaporate more readily during the annealing step.

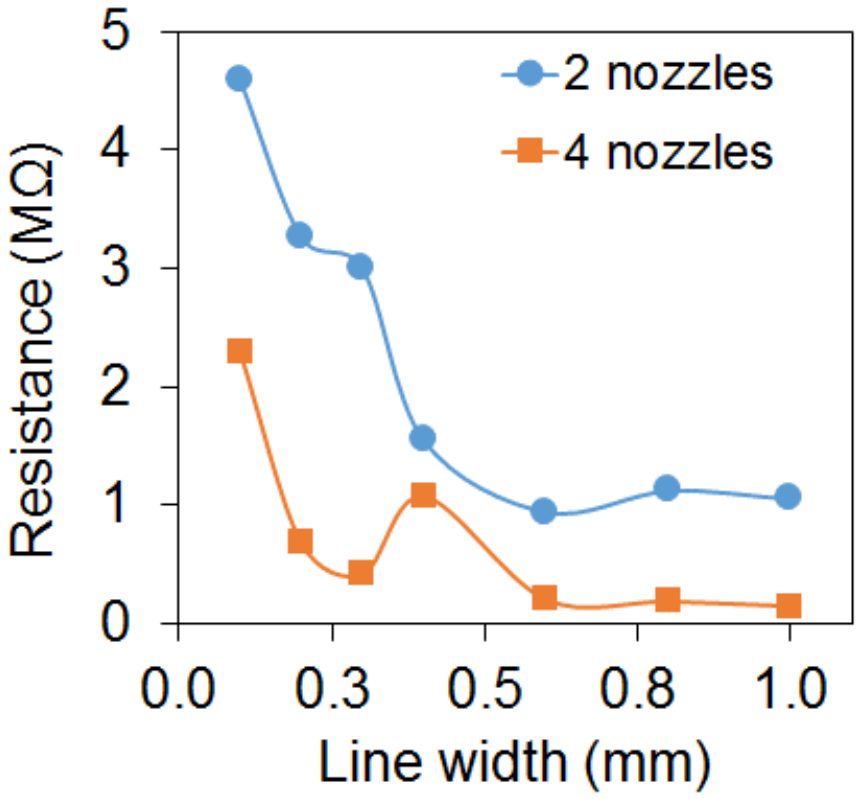

Figure 3.5: Change in resistance values with different printed line widths. The probe-tip separation was 1.5 mm.

3.3 Effect of Number of Passes

The effect of the number of printing passes was also examined here, where we conducted tests at 15, 25, 35, 45, 55 and 65, passes for ink printed on the SiO_2/Si substrate, and annealed at 300°C for 1 hour, as noted earlier, and measured the ensuing I-V Characteristic that is shown in Figure 3.6; the inset in Figure 3.6 shows the device geometry. Figure 3.6 shows Ohmic behavior with maximal current transport occurring when 25 passes were used, where increasing passes of 35, 45 and 55 passes progressively decreased the currents, and no continuous channel was observed for 15 passes.

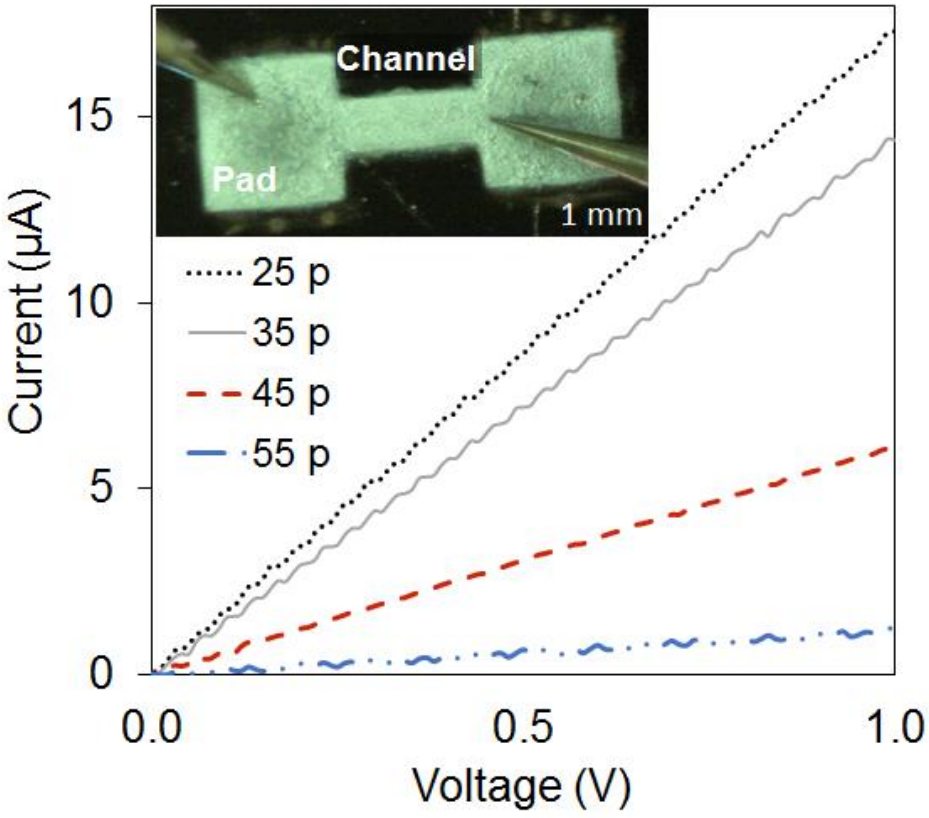

Figure 3.6: I-V Characteristics comparing number of passes. Inset showing printed pattern indicating channel (1.5 mm length, 0.5 mm width) and square pad (1.5 mm) sections.

Figure 3.7 shows the variation in R with increasing printing passes, while the inset shows the thickness of the printed graphite films, which increased as the number of passes increased, particularly after 45 passes where a dramatic increase was noted. The lowest ρ value was obtained for 25 passes, where ρ was calculated to be 3.8 mΩ-m. The increase in R values with increasing passes was likely due to the inability to evaporate the EC and NMP from the presumably thicker printed film where, as an example, the thickness for 45 passes was as high as 420 nm.

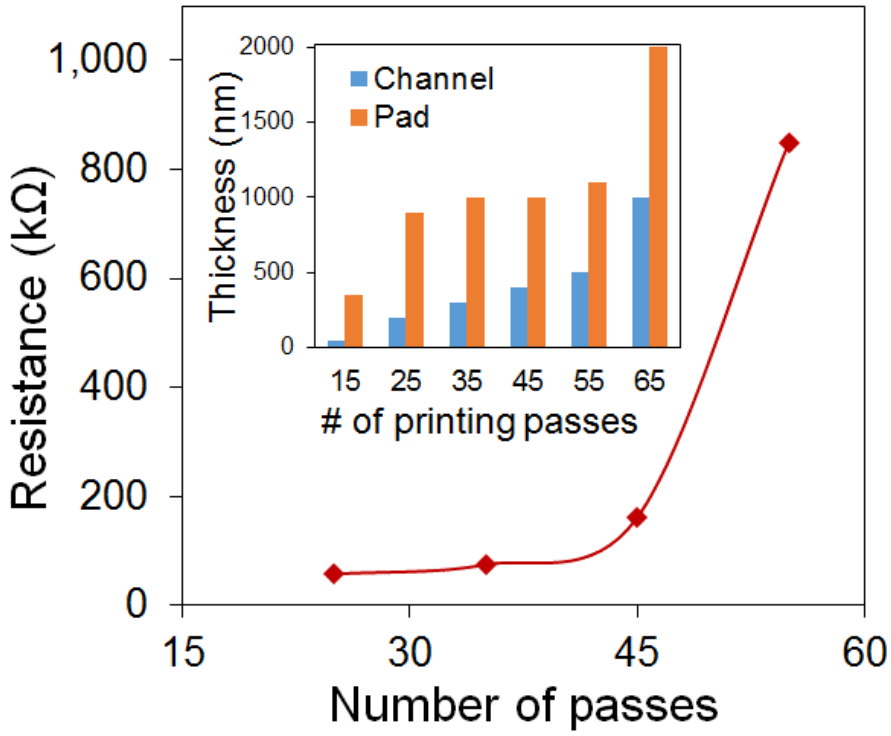

Figure 3.7: a) I-V Characteristics comparing number of passes. Inset showing printed pattern indicating channel (1.5 mm length, 0.5 mm width) and square pad (1.5 mm) sections. (b) Resistance values as a function of the number of passes. Inset showing average thickness of channel and pad with varying number of passes, where thickness was measured using a profilometer.

The inset in Figure 3.7 shows the average thickness for the pad and channel regions increased at a different rate with the number of printing passes, and in the case of the channel region, the films were consistently thinner than the pad. This is explained on the basis of the ink migrating to the pad region due to fluidic and capillary interactions during the first few passes, resulting in thicker films in the pad regions compared to the channel; moreover for 15 passes, where no electrical transport was detected as discussed in the context of Figure 3.2a, the thicknesses were measured to be 55 nm, suggesting that the density of graphite nanomembranes in the channel region is not sufficient to form a continuous network at these thicknesses. The above results on the printing parameters, such as number of active nozzles and printing passes clearly demonstrates the importance of optimizing these parameters to yield functional structures of 2DLMs using ink-jet printing.

3.4 Effect of Annealing Temperature and Time

We proceeded to examine the role of the annealing T-time profile on the morphological and electronic transport characteristics for structures printed on SiO_2/Si substrates where 30 printing passes were used. The annealing temperatures considered were 250°C, 300°C, 350°C, 400°C and 450°C, and two annealing times were used, 1 hour and 2 hours. The top-surface SEM images were obtained from the channel area and are shown in Figure 3.8a-(f). The microstructure for the sample annealed for 1 hour at 250°C (Figure 3.8a) shows random particles embedded in a matrix structure which is presumed to be remnant EC. Ethyl Cellulose is a polymer that possesses excellent membrane-forming ability and durability and is commonly used as a flexible coating for paper, cloth and leather. However, at the same time, the electrical properties of EC indicates that it is electrically insulating, which corroborates the fact that the *R* for this sample was the highest at 2 MΩ, as noted in Figure 3.9. Thus, the SEM in Figure 3.8a shows the excessive presence of

EC when a low annealing temperature of 250°C is used. The microstructure of the samples that were annealed at higher temperatures (see Figure 3.8b-(c)) shows that this potentially insulating matrix is largely removed (less charging is seen in the SEM images of Figure 3.8b and (c) when compared to (a) for example), and a more uniform and conducting film has formed, which is corroborated by the lower *R* values seen in Figure 3.9 for samples annealed at temperatures > 300°C. Figure 3.8c shows increased porosity in the microstructure for annealing temperature of 450°C, which is consistent with the increased *R* values seen at 450°C in Figure 3.9.

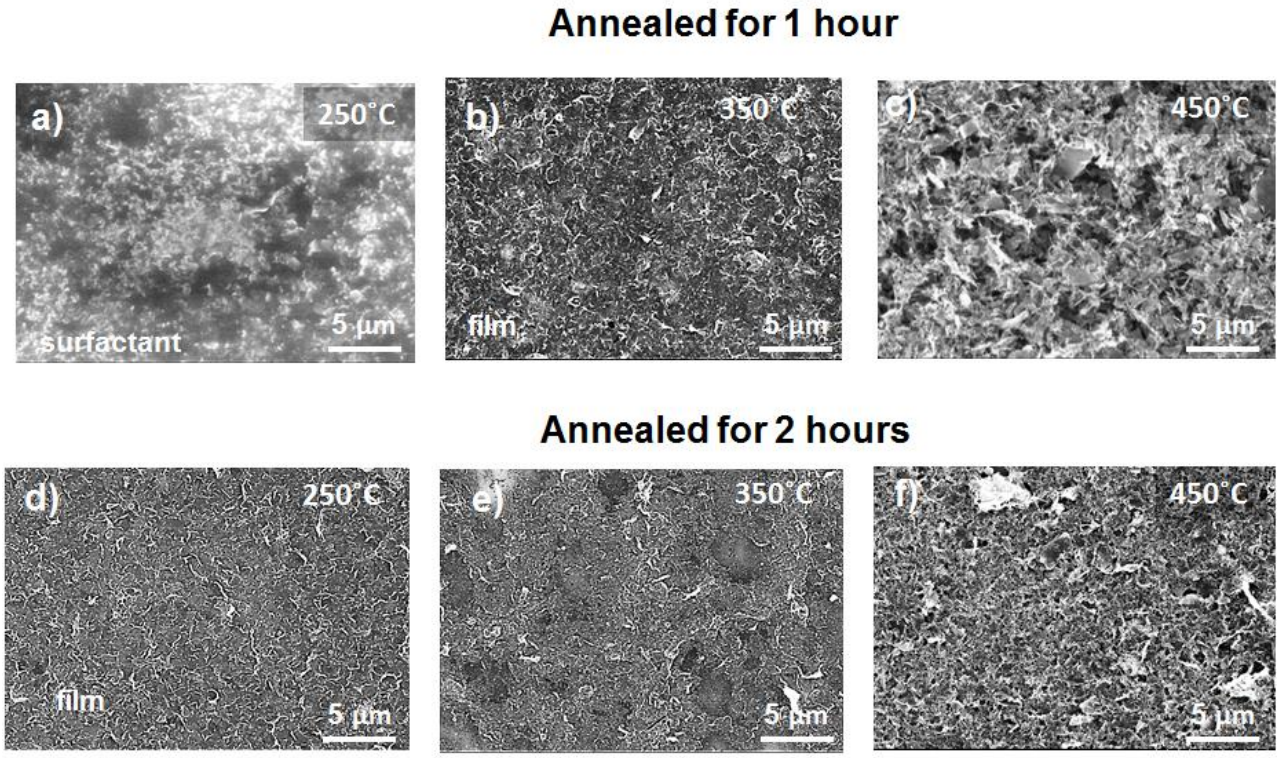

Figure 3.8: SEM images showing microstructure of the ink-jet printed lines after annealing for 1 hour (a)-(c) and 2 hours (d)-(f).

Annealing for 2 hours at the same temperatures (250°C – 450°C) resulted in a significant reduction in *R* values, as shown in Figure 3.9. The *R* was reduced from 2 MΩ to 43 kΩ for samples annealed for 1 hour and 2 hours, respectively, at an annealing temperature of 250°C. The corresponding microstructures depicted in Figure 3.8d-(f) show more film uniformity at all temperatures, which correlates to the enhanced electrical conductance values (Figure 3.9), in contrast to the case where the samples were annealed for 1 hour only. The longer annealing time likely accounts for the additional diffusion and coalescence of the nanomembranes to yield uniform films.

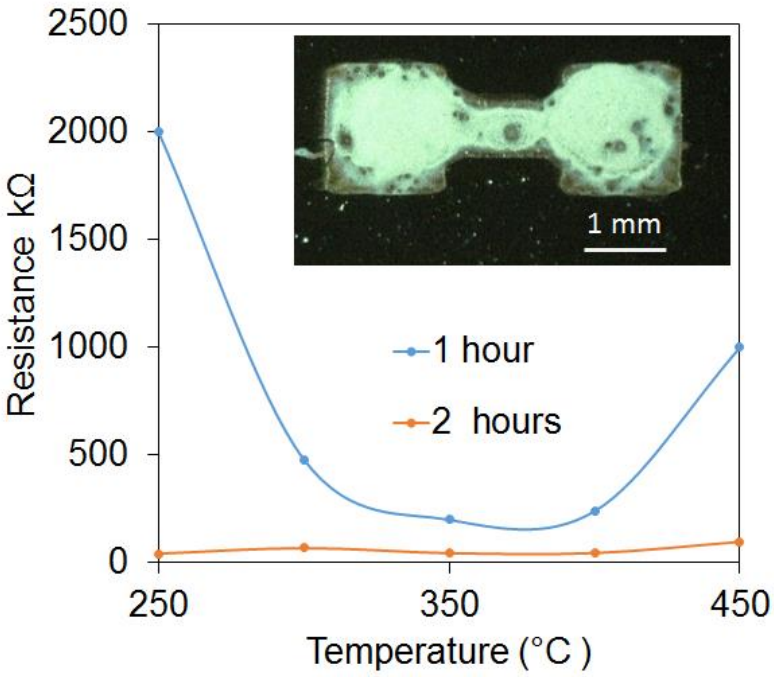

Figure 3.9: Resistance values variation as a function of the annealing temperature for the two times considered.

The temperature-time profile of annealing on our samples demonstrated that while lower annealing temperatures can be traded for high-annealing temperatures, the annealing time has to

increase to drive-off the excessive remnant solvent. This decrease in annealing temperature is advantageous to widen the portfolio of materials that would otherwise be precluded in flexible electronics, given thermal stability issues at higher temperatures in some of these materials systems.

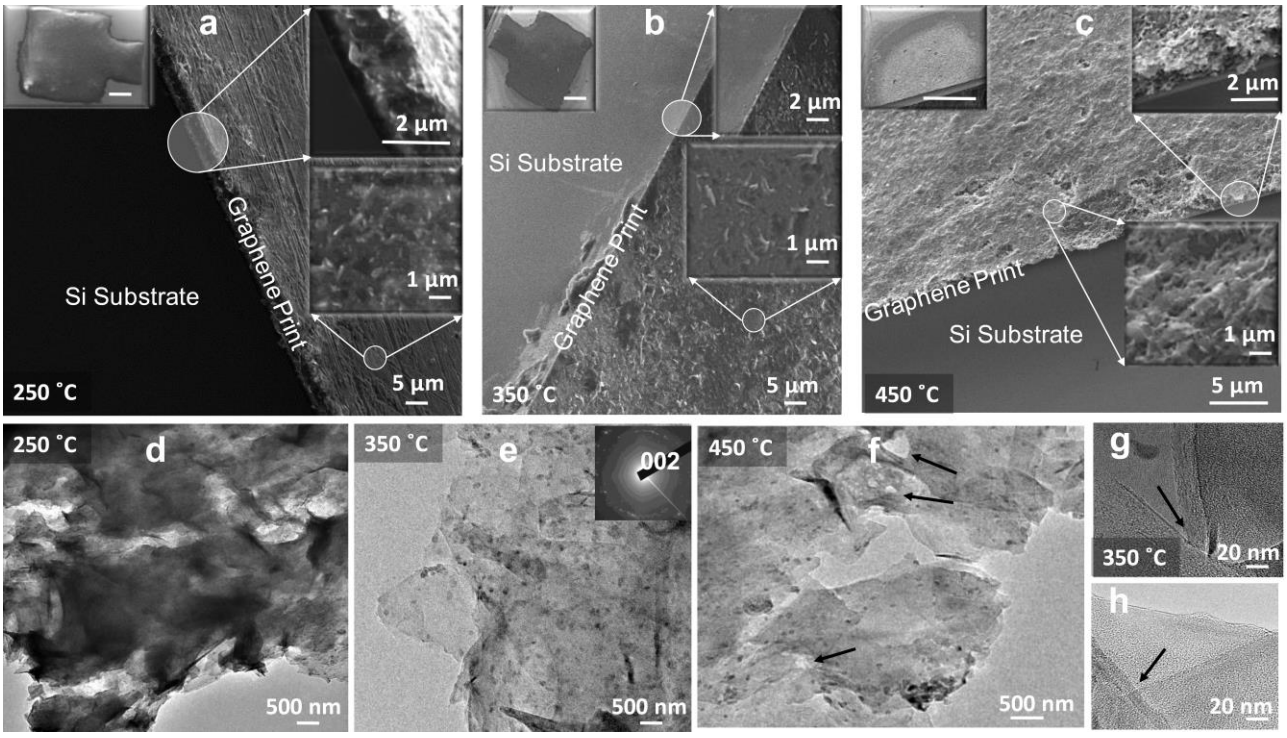

Figure 3.10: SEM images showing the interface between printed sample and SiO_2 /Si substrate for 1 hour annealed samples at (a) 250°C, (b) 350°C and (c) 450°C. Left top insets in (a)-(c) show low magnification images of the sectioned sample (scale bar ~ 0.5 mm). The high magnification cross sectional SEM images (top right in (a)-(c)) reveal the interfacial characteristics between the ink-jet printed graphene and the SiO_2 /Si substrate. The right bottom images show the surface morphology in (a)-(c). In (d)-(f), bright field TEM images of the printed graphene film are shown for samples annealed at 250°C, 350°C, and 450°C, respectively. Arrows in (f) depict the presence of voids. The stacking of the graphene sheets is seen in (g)-(h) for the 350°C annealing time where arrows show the stacked graphene nanomembrane junctions.

To further build upon understanding the morphological characteristics of the ink-jet printed graphene films, Figure 3.10a-(c) show high-resolution SEM images of the printed films that were annealed for 1 hour at 250 °C, 350 °C and 450 °C, while Figure 3.10d-(f) show the TEM images at the corresponding annealing conditions. The high resolution SEM images were obtained for ink-jet printed samples that were sectioned orthogonal to the plane of the substrate within the channel area (these sample images are shown in the top left insets of Figure 3.10a-(c)), where cross sectional SEM images of the printed films were also obtained and are shown in the top-right insets of Figure 3.10a-(c). From the cross sectional image of the 250°C heated sample shows a thick continuous film with graphene embedded in a matrix material which is likely to be remnant EC, as eluded to earlier. As the annealing temperature was increased to 350°C (see Figure 3.10b), the graphene nanomembranes are denser and the surface morphology (middle right inset of Figure 3.10b) reveals a uniform surface topography. When the annealing temperature was raised to 450°C, the porosity of the films increased as voids were apparent (Figure 3.10c inset on right), and the surface is notably rougher and less uniform (Figure 3.10c inset on left middle). These results seem to be consistent with the electrical transport measurements of Figure 3.9, which indicated 350°C to be the optimum annealing temperature.

In order to conduct the TEM study of the ink-jet printed graphene films, Cu grids were used, and the TEM results are shown in Figure 3.10d-(f). The TEM results once again reveal that the sample annealed at 250°C shows graphene sheets embedded in a matrix material (EC/solvent), as shown in Fig. 3.10d. As the annealing temperature was increased to 350°C (Figure 3.10e), the graphene membranes are clearly visible from the bright-field images, and a good intermembrane connection is noted, suggesting that the EC/solvent between them has been largely removed.

The selected area diffraction (SAD) pattern of the sheets confirms the 002 orientation of multiple graphene sheets (shown in the top right inset in Figure 3.10e). Finally, when the annealing temperature was increased to 450°C, the presence of voids is noted to increase, as shown by the location of the arrows in the figure. The high magnification TEM images of Figure 3.10g and (f), correspond to the annealing temperature of 350°C, clearly reveal stacking of graphene layers with the interface marked with arrows. The presence of the dark islands within the graphene membranes in Figure 3.10e and (f), is suggestive of defective sites, which may be due to remnant residues from the solution dispersions, which we discuss in more detail in the context of the temperature dependent response of the resistivity of our printed films.

Our ink-jet printed graphene films were further characterized using Raman spectroscopy, as well as temperature-dependent Raman, which is a non-invasive technique used to characterize the structural and electronic properties of materials [121]. The Raman shift is depicted in Figure 3.11a for samples annealed at temperatures ranging from 200 to 450°C, which shows the well-defined D band (1350 cm^{-1}), G band (1580 cm^{-1}) and a 2D or G' band (2700 cm^{-1}), indicating the presence of monolayer or few-layer graphene. The D band has been attributed to in-plane A_{1g} zone-edge mode [122] and can be used to monitor the defect distribution of graphite films by computing the D/G ratio [123]. Conductivity data has not been reported for the sample annealed at 200°C due to its excessively high R beyond the scope of the instrumentation. The defect ratios for samples annealed at 1 hour and 2 hours in Figure 3.11b demonstrate the films with the lowest D/G values occur for samples annealed at 350°C for 1 hour, and 300°C for 2 hours which is consistent with our electrical data (Figure 3.11(d)), where the lowest R values were seen at these conditions. Furthermore, the full-width-half-maximum (FWHM) of the D band is used to monitor defect distribution in graphene films [124]. The D band showed a maximum FWHM of ~ 99 cm^{-1}

for samples annealed at 250°C, which decreased to ~ 40 cm^{-1} for annealing at 350°C, as seen in Figure 3.11(b).

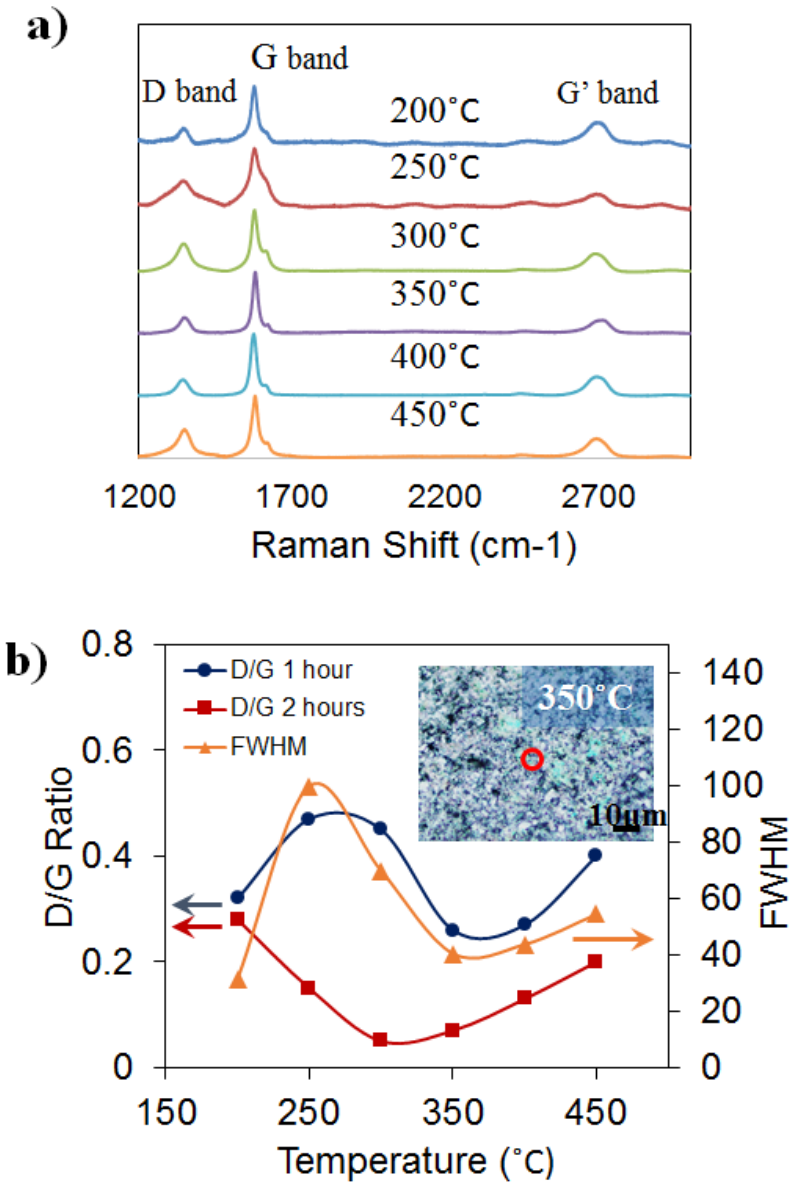

Figure 3.11: Raman analysis of the printed graphite films. a) Raman shift as a function of annealing temperature for ink-jet printed graphene. b) Change in the D/G ratio for samples annealed at 1 and 2 hours; secondary axis indicating FWHM of D band corresponding to one hour annealing time.

This further verifies that the minimum defect distribution in the ink-jet printed graphite films occurred at an annealing T of 350°C. As the annealing T increases from 250°C to 350°C, the defect concentration was reduced, and the nanomembranes align themselves while forming a highly conductive printed graphite film, which is consistent with the TEM measurements on our samples as well. It is not surprising that operating ink-jet printed graphite films at high power levels may have the potential for increased Joule heating, which can change the crystalline and electronic properties of the printed graphene films at these high-thermal/power conditions.

We proceeded further with the Raman measurements using the same sample that had been annealed for 350°C, to conduct T-dependent Raman measurements from 24.4°C to 600°C, where the data is shown in Figure 3.12a. When defects are present, it gives rise to two other features in the Raman spectra at ~ 1350 cm^{-1} (D band) and 1615 cm^{-1}(D' band). The D' band appears as a small shoulder on the G band, and the intensity of the D' band is relatively small compared to the D band [125]. Clear peak shift in the G band is seen toward lower wave numbers with increasing temperature, similar to the case for the D' band which gets more pronounced in intensity at 600°C compared to room T. Previous investigations have demonstrated that electron-phonon coupling plays an important role in the T dependence of the G band shift [126].

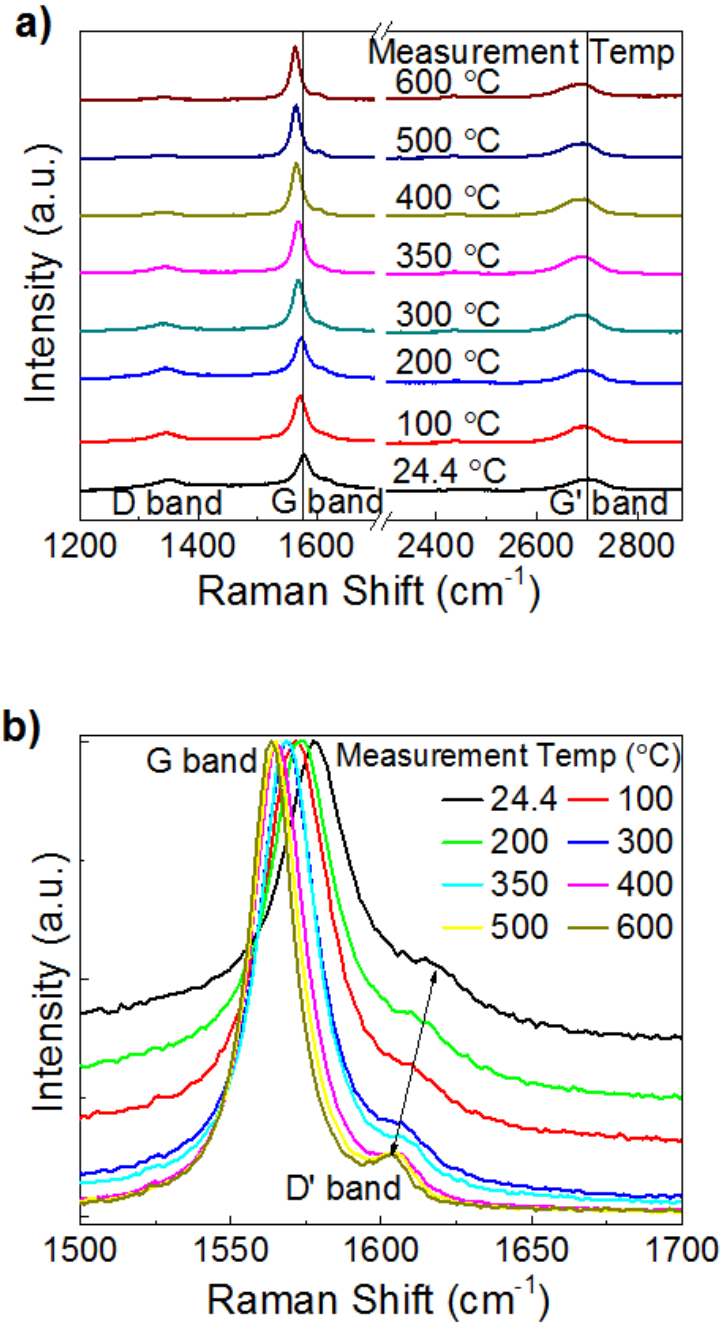

Figure 3.12: a) Raman peak shift at different Ts for the 350°C and one hour annealed sample. b) Change in position of G' and D' band as measured at different Ts for the one hour 350°C annealed sample.

The thermal expansion coefficient (TEC) is an important thermal and mechanical performance parameter of the printed graphite films, which can be estimated from the Raman data. The TEC of the printed graphite film was estimated from the G and G' band Raman peak position shift and the data are shown in Figure 3.13a and Figure 3.13b respectively. Near room temperature (24.4°C) printed graphite films exhibit a G band near 1577.4 cm^{-1}; however, it decreased to 1563.5 cm^{-1} with increased temperature up to 600°C, which resulted in a G band peak shift in printed graphite films close to 14 cm^{-1}, as shown in Figure 3.13a. Similarly, the peak shift in the G' band was observed to be nearly 17.5 cm^{-1} as shown in Figure 3.13b (from 2701 cm^{-1} at 24.4°C to 2684 cm^{-1} at 600°C). These results in printed graphite films match previously investigated single and few layered graphene films on different substrates [121]. Higher shift with increasing temperature in the G' band (17.5 cm^{-1}), compared to G band (14 cm^{-1}) matches previously investigated CVD grown graphene films on copper substrates, highlighting the double resonance processes in the G' band, which were more sensitive to the changes in the electronic band structure than due to T induced strain [127]. On the contrary, the G mode is an optical phonon with zero vector which is very sensitive to carrier density instead of strain [123, 124].

The T dependence of the G and G' mode frequency shift in printed graphite films can be represented by the following relation: $\omega = \omega_0 + \chi T$, where ω_0 is the Raman frequency shift when the temperature T is extrapolated to 0 K, and χ is the first-order temperature coefficient determined by the slope of the linear fit. The extracted negative value of the G band temperature coefficient χ_G was ~ 2.8 μeV/°C, which was much smaller compared to the G' band temperature coefficient $\chi_{G'}$ (3.5 μeV/°C). Previous investigations have also shown χ_G to be smaller than $\chi_{G'}$ (~12 and 22 μeV/°C, respectively [124]); however, we have found the values obtained in this work, to be much smaller, indicating ink-jet printed graphite films to be less susceptible to thermal cycling.

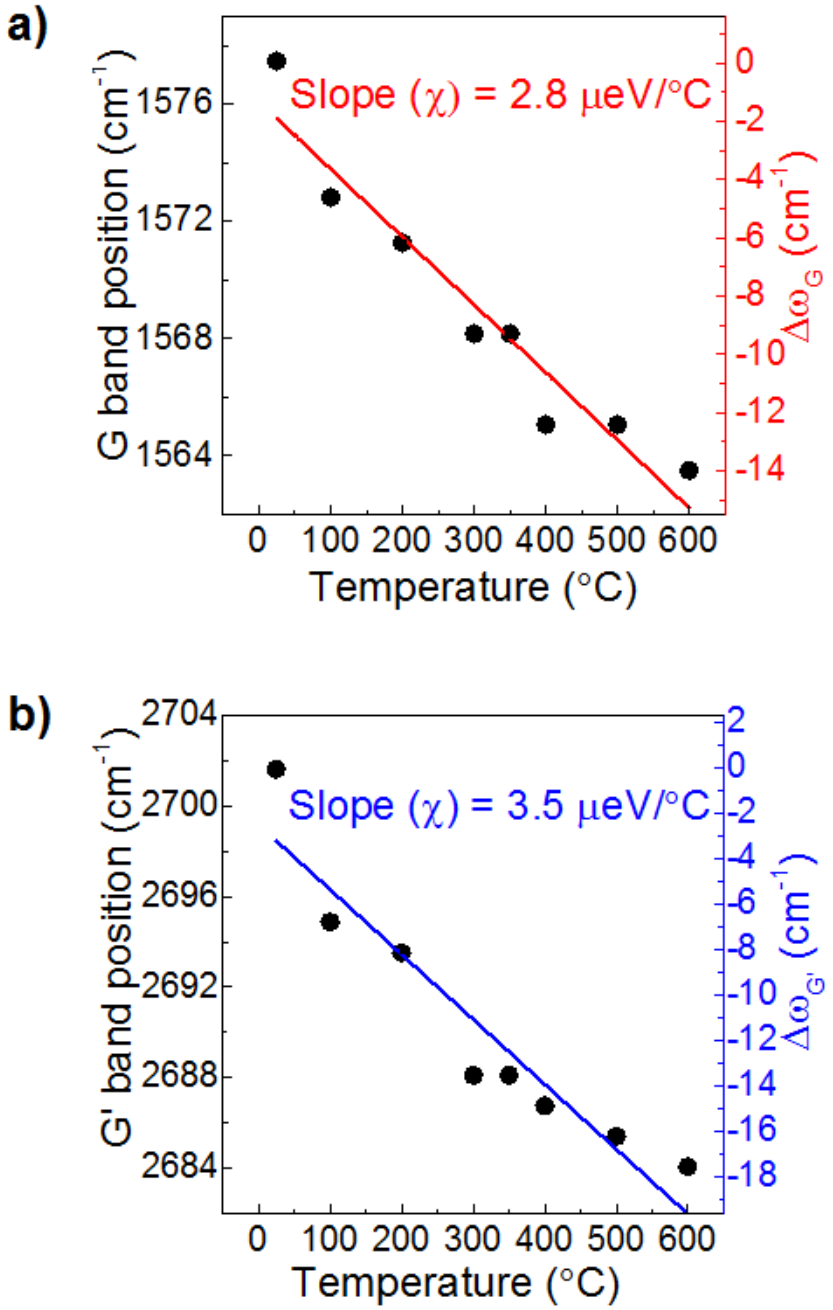

Figure 3.13: a) Calculated slope for shift in G (χ_G ~ 2.8 μeV/°C) and b) G' ($\chi_{G'}$~ 3.5 μeV/°C) bands.

Chapter 4:

Fabrication and Characterization of a High-power Resistor

Continuous miniaturization of devices, for example in consumer electronics, defense and aerospace applications, is largely driven by our desire for smaller, light-weight, ultra-thin devices, where such structures on fully flexible platforms can drive down costs even further [128, 129]. For flexible electronics applications in particular, the substrates pose less restrictions compared to the Si-based semiconductor industry, where in the former a wide variety of additive manufacturing techniques easily lend themselves for the production of functional structures on arbitrary substrates within the context of what is generally referred to as "printed electronics." The previous analysis of our ink-jet printed graphite films provided insights into the micro - and nanostructure of our material, which guided the design of a resistive, high-power structure that was constructed on both rigid and flexible and transparent substrates, and exhibited high-performance characteristics which we now describe in more detail here.

High-power resistive structures have applications as temperature sensors, heating elements, current limiters, or in thermal management as heat spreaders to facilitate heat transfer [130, 131]. As mentioned, the formulations were used toward the successful fabrication of a high-power graphite resistive structure that was printed on both rigid and flexible substrates, and can deliver power levels approaching 10 W, where a near-flat, negative temperature coefficient of resistivity (TCR) was measured. The change in resistance R with respect to an increase in T of a material, as denoted by the TCR, is positive for $R \propto T$ or negative where $R \propto 1/T$. The activation energy E_a was computed to be ~ 2.4 meV for our ink-jet printed graphite resistors, which is 100X

lower compared to high TCR materials such as mechanically exfoliated graphene, for measurements we conducted in the 6 K – 350 K range [130]. Interestingly, previous studies have shown the possibility of using the temperature-dependent electrical properties of graphene as a temperature sensor [132]. In other studies, positive and negative TCR materials have been combined to achieve a near-zero- (NZ-) TCR bilayer composite structure [133]. Resistors having NZ-TCR are desirable for various applications, such as analog and data conversion circuits, specialty instrumentation circuits, and static random access memories (SRAMs) [134]. High-power resistors that can dissipate many Watts of electrical power as heat may be used as part of motor controls, in power distribution systems, or as test loads for generators. While one-dimensional (1D) carbon nanotube based systems demonstrate a NZ-TCR, our results show the TCR and E_a to be the lowest amongst the 2DLMs reported to date. We have modeled the transport characteristics of our ink-jet printed features as a composite structure made up of remnant Ethyl Cellulose (EC) used in the solution dispersion as a surfactant, not to mention the graphite nanomembranes contributing toward the composite behavior as well. The unique microstructure of our printed nanocomposite was used as a basis upon which to explain the thermal response of the electronic transport of our devices that we believe is mediated via defects in the sonicated graphite. Evidence for defects was validated via Raman Spectroscopy and Transmission Electron Microscopy of our ink-jet printed graphene nanomembranes. The thermal-invariance of resistivity or a small TCR exhibited by our devices has utility as a component in flexible electronics where a stable current or heat-load load maybe necessary in harsh or extreme thermal environments.

4.1 METHODS AND MATERIALS

Materials: The ink used in this work was prepared by sonicating commercially available graphite rod pieces (Sigma Aldrich #496553) at a concentration of 6mg/ml in N-methyl-2-pyrrolidone

(NMP) (Sigma Aldrich #270458) for 24 hours. A Branson 2800 bath sonicator was used for all sonication in this work. After the sonication, 4%wt Ethyl Cellulose (EC) (Sigma Aldrich 200646) was added to the dispersion and sonicated for another 4 hours. The ink was separated after allowing the dispersion to stabilize overnight and selecting only the supernatant to avoid any precipitates that may contain bigger particles. *Printing*. The DIMATIX 2831 material printer from Fujifilm was used for the ink-jet printing, where the ink cartridges were purchased from the manufacturer and had a volume of 10 pl. The cartridges comprised of 16 nozzles with a nozzle diameter of ~ 21.5 μm. All heat treating was done on a hot plate at ambient conditions. *Characterization:* SEM microscopy was carried out in a Hitachi S-4800. The TEM analysis was conducted using a TEM 2100F field emission gun. Electrical characterization was conducted using a micromanipulator 450PM-B probe stage equipped with a HP precision semiconductor parameter analyzer 4156A. A Lakeshore CRX–4K probe station was used to obtain the *R* vs *T* data with a Keysight B1500-A Semiconductor Device Analyzer.

4.2 POWER MEASUREMENTS

In this work, the power handling and dissipation characteristics of our ink-jet printed device was evaluated, and cryogenic measurements of the electronic transport were conducted from 6 K to 350 K from which the TCR, and other parameters were tabulated. The operational power of the printed devices was investigated with different annealing temperatures to examine their high power operational capabilities. Figure 4.1a shows output power variations of samples that were annealed for 1 hour (top graph) and 2 hours (bottom graph), where the data shows the power response for samples annealed from 300°C to 450°C. The highest output power of the printed graphite films was obtained for samples annealed at 350°C for both the 1 hour and 2 hours cases. However, analysis of the annealing time shows that the sample annealed at the 1 hour time

exhibited an ability to deliver 90 μW of power at 1 V, which was higher compared to the sample annealed for 2 hours that delivered 20 μW at 1 V. Our ink-jet printed graphite devices exhibited very low *R* (43 kΩ) and consequently very high output current and power compared to previous investigations (up to 600 MΩ and 4 MΩ in Ref [132] and [135], respectively). Due to this reason, we expected very high power operation in our printed devices.

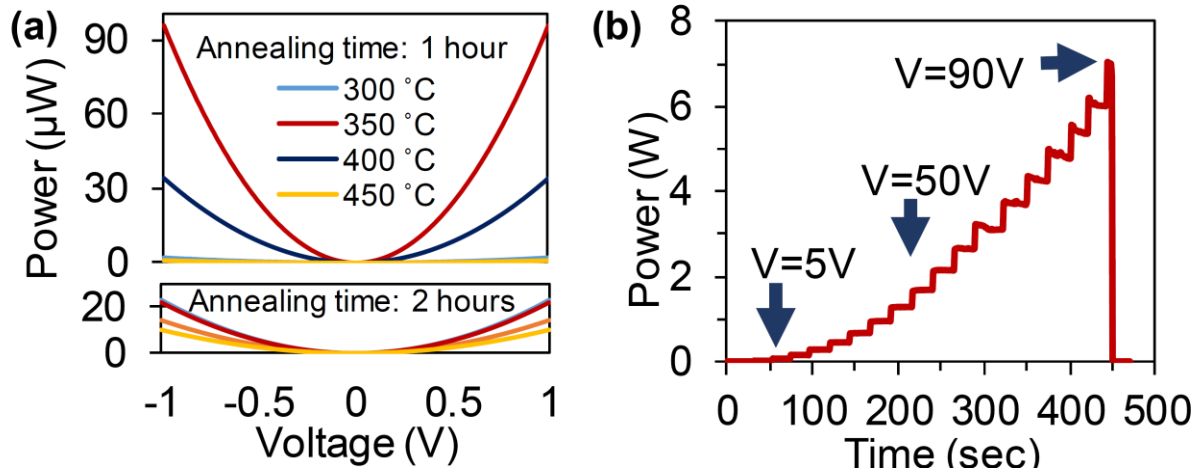

Figure 4.1: Figure 6. a) Output power variation for the printed devices after one (top) and two hours (bottom) of annealing time. b) Temporal output power variation as increased voltages were applied to the device which shows the ability of the structure to deliver 7 W of power.

Figure 4.1b shows the temporal output power variations when increasingly higher applied voltages were applied. The power increased up to 7 W when the applied voltage increased to 90 V, at which point Joule heating at the contacts limited the transport. This measurement clearly shows the potential of our ink-jet printed graphite devices to operate under extremely high output power conditions, approaching ~ 10 W. According to our knowledge this was significantly higher compared to previous investigations (5 mW in Ref. [135]), and strongly highlights the opportunity to apply our ink-jet printed graphite films for high power applications for flexible electronics.

4.3 RESISTANCE VS TEMPERATURE MEASUREMENTS

In order to better understand the electronic transport characteristics of our ink-jet printed graphite resistors, we conducted R-T measurements of our devices from 6 – 350 K from which the TCR and thermal index were computed. To conduct this measurement, first a mask was prepared on a transparency, as shown in the top, left inset of Figure 4.2, in order to lithographically define regions where large Mo contacts were sputter deposited and patterned via lift-off. The graphite lines were then ink-jet printed to connect the Mo-contacts on which the probes for the cryogenic test were placed to ensure a good electrical contact without mechanically disrupting the network of nanomembranes from the ink-jet printed graphite for this thermal transport test.

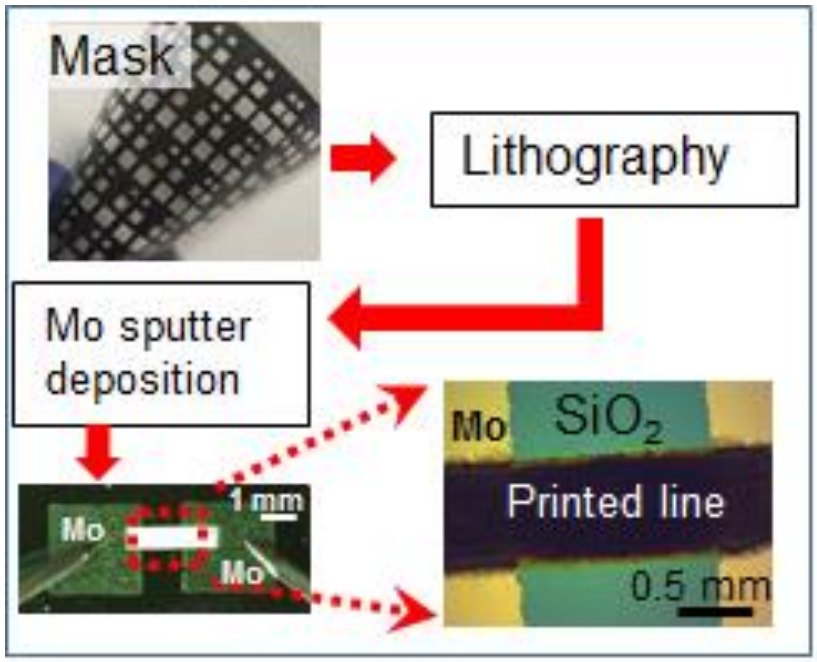

Figure 4.2: Process flow used to prepare the samples for R-T measurements.

The fabricated device is shown at the bottom left inset of Figure 4.2, while the magnified image in the bottom right inset of Figure 4.2 clearly shows the ink jet printed line bridging the Mo electrodes. Figure 4.3 shows the change in R with T for two different annealing conditions (250°C

and 350°C annealed for 1 hour) and the ln*R* (logarithmic scale) versus 1000/*T* characteristic of the structures. The sample annealed at 250°C showed consistently higher *R* values (e.g. 82.79 kΩ at 140 K) when compared to the sample annealed at the higher temperature (e.g. 2.92 kΩ at 140 K). This data was fit to the Arrhenius Model, denoted by Eqn. (1) below:

$$R(T) = R_o exp(\frac{E_a}{2kT}) = R_o exp(\frac{B}{T}) \quad (1)$$

where *R(T)* is the *R* at temperature *T*, R_o is the *R* at $T = \infty$, E_a is the thermal activation energy as noted previously, *k* is the Boltzmann constant, and *B* is the thermal index. Eqn. (1) can be rewritten as:

$$lnR = lnR_o + \frac{E_a}{2kT} = lnR_o + \frac{B}{T} \quad (2)$$

where a linear relationship is expected between the *ln R(T)* vs. *T* plot [130].

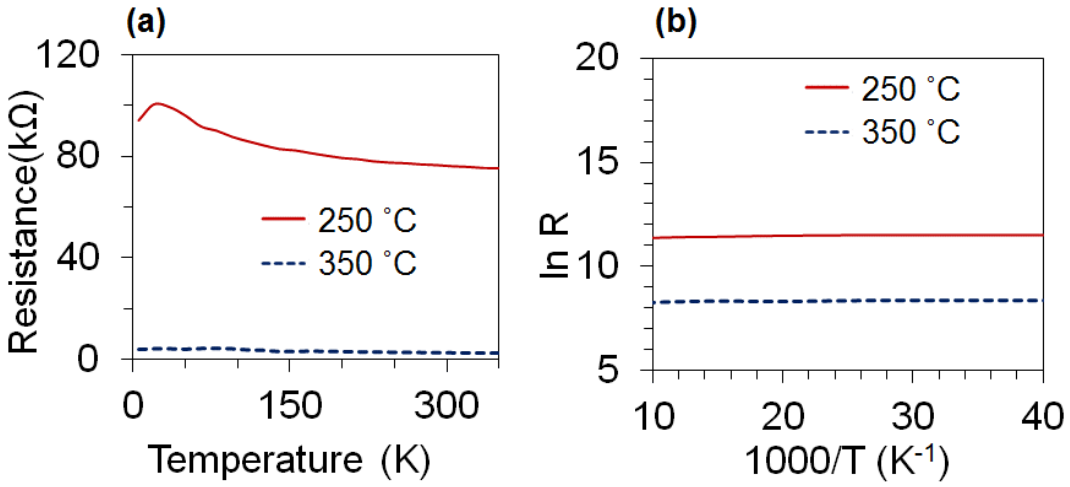

Figure 4.3: (a) Variation of resistance values with respect to temperature and (b) *ln (R)* is plotted as a function of 1000/T.

When plotting ln *R(T)* as a function of *1000/T* (Figure 4.3b), the thermal parameters *B*, E_a and TCR were extracted, and were tabulated to be 14 K, 2.4 meV and 0.015%, respectively. These

values are also shown in Table 1 which compares our results to other material systems noted from prior work.

Table 4.1. Comparison between high, low and NZ-TCR materials indicating thermal index *B*, activation energy E_a, and TCR values from prior reports.

Temperature response	**Material**	**Thermal index *B* (K)**	**Activation Energy E_a (meV)**	**TCR (%K^{-1})**	**Reference**
High TCR	Graphene	1034	177.84	-1.148	[135]
	Graphene	946	167.2	-1.05	[130]
Low TCR	Printed graphite film	14	2.4	-0.015	This work
Near zero TCR	Carbon Nanotube + Carbon Black	5	0.86	-0.005	[133]
	Antiperovskite $Mn_3Ni_{1-x}CuxN$	2	0.34	-0.002	[136]

Both annealing conditions resulted in very small thermal index (14) over the *T* range studied and they displayed a negative TCR behavior. In general, most materials display much larger TCR values, but a few limited materials show NZ-TCR behavior [136]. High TCR materials demonstrated earlier (such as graphene) [130, 135] exhibited TCR values of ~ 1.14 % with *B* and E_a ~ 1034 K and 177 meV, respectively (see Table 1). These type of materials are primarily used for thermistor, temperature sensing devices and heating applications [137]. The printed graphite film demonstrated here falls in the low TCR category, and materials with low TCR or NZ-TCR can be used in a wide range of applications such as resistors in high precision electric heating systems, thermoelectric devices, micro heaters and other areas where a constant *R* over a range of temperatures is desired [136]. Our analysis shows that our devices exhibited the lowest reported TCR values amongst 2DLMs. Simultaneously, the printed graphite film demonstrated the ability

to deliver very high power levels ~ 7 W without degrading or failing. Therefore, the printed graphite film demonstrated in this work will be extremely valuable for high-power flexible electronics applications, with the unique low TCR feature at the same time.

The previous results allow us to propose a model to explain the *R* response of the prepared material with temperature. The total *R* of the composite film is the result of the addition of the temperature dependent contributions of the *R* from various sources which are indicated below in Eqn. (3).

$$\rho_{composite}(T) = \sum \rho_G(T) + \rho_{interface}(T) + \rho_{defects}(T) + \rho_{EC}(T) \quad (3)$$

Where $\rho_{composite}$ represents the *R* of our overall ink-jet printed composite structure, ρ_G is the intrinsic *R* of the graphite membranes, $\rho_{interface}$ is the *R* at the interfacial junctions between nanomembranes, $\rho_{defects}$ is the *R* due to defects within the nanomembranes and ρ_{EC} is the R due to the remnant EC/solvent; *(T)* indicates that these terms all have their unique *T* dependencies, and the overall $R\,\rho_{composite}$ is a sum over all of these ensemble contributions. Our previous discussion on the Raman data demonstrated that the presence of the prominent G peak which indicates that the graphite is dominant in the composite and so the contribution from other components such as remnant EC should be minimal in the thermal response. The contribution from the $\rho_{interface}$ should also be minimal since at higher temperatures there should be more energy for electrons to tunnel across the interface reducing *R*, which we do not observe strongly here. We believe the contribution from the defects is dominating the electronic transport response, where the D/G ratio was seen to be ~ 0.26 from Raman Spectroscopy in the ink jet printed films, while the TEM also showed dark agglomerations for samples annealed at 350°C (e.g. Figure 3.10f). The slight negative TCR dependence with E_a ~ 24 meV represents a small energy activation barrier for

electron hopping that explains the negative TCR, but the generally temperature insensitive *R* is suggestive of transport limited by defects, which we have exploited judiciously to our advantage to demonstrate a practical device for flexible electronics.

4.4 PRINTING ON FLEXIBLE SUBSTRATES

The prepared ink was also printed on flexible polyimide and polyethylene terephthalate (PET) substrates. Figure 4.4a and (b) show *R* values for graphite inks printed on rigid SiO_2/Si substrates and on flexible polyimide substrates, respectively, with the insets in both figures reflecting printed structures on the various rigid, flexible and transparent PET substrates. The *R* scaled linearly as the probe separation distance increased in both Figure 4.4(a) and (b), as expected. However, for the case of the polyimide substrate (Figure 4.4(b)), the *R* was generally lower, which may be due to better adherent properties of the graphite ink on the carbon based polyimide substrate compared to SiO_2/Si.

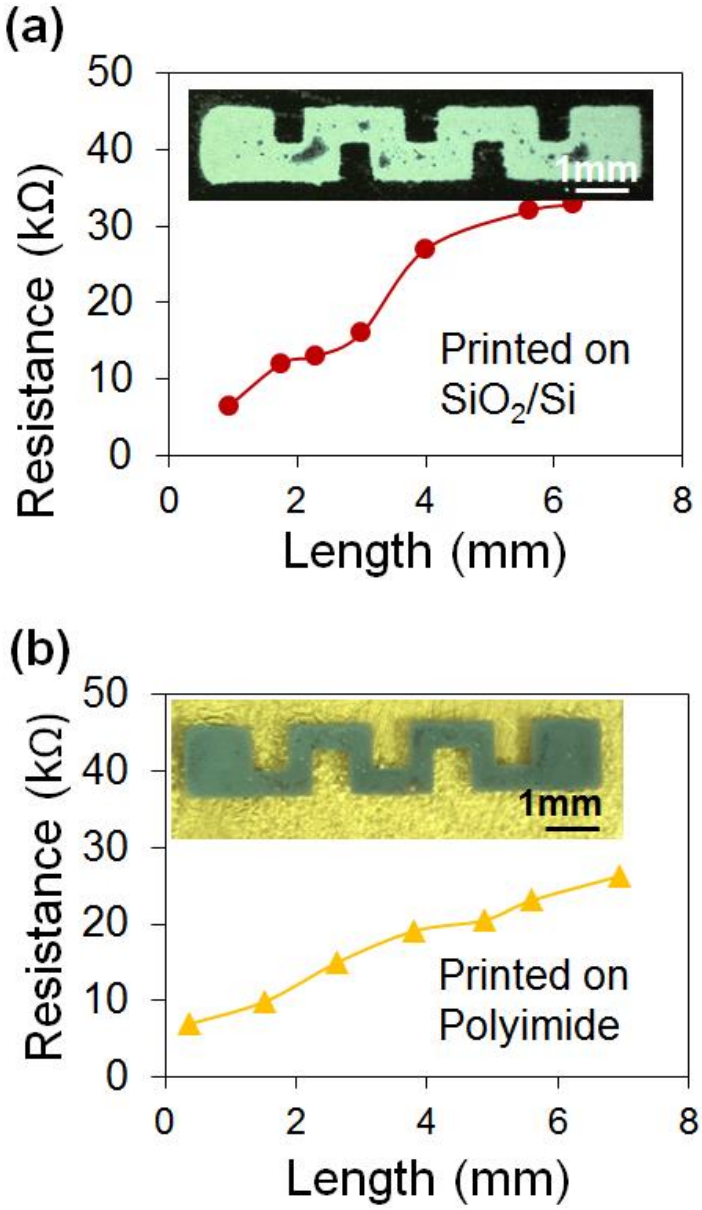

Figure 4.4: a) I-V comparison of printed ink on both SiO_2/Si, and on b) polyimide substrates for 1 hour of annealing time; top inset showing optical image of a printed pattern on PET substrate and bottom inset is an image of a resistive structure printed on polyimide substrate.

Chapter 5:

Surfactant-free Inks

Ethyl Cellulose has long been used as a surfactant as well as to tune the viscosity of printable inks [119]. The motivation for this work was to develop a solution dispersion that does not rely on the addition of any surfactant, functionalization group or stabilizer to begin with, and yet it possesses the rheological properties that make it suitable for ink-jet printing. We have succeeded in creating such a dispersion, where the viscosity values of Cyclohexanone (*C)* and Terpineol (*T)* are optimized to yield a printable ink, but where the exfoliating potential of *T* is also noted. Surfactant is used to aid in the stability of the dispersions which has been necessary in prior reports on the ink-jet printing of 2DLMs to avoid agglomeration that leads to nozzle clogging over time. Remarkably, our prepared inks are stable for weeks without the need for surfactants, where a brief sonication step for a few minutes is necessary to condition the dispersion just prior to ink-jet printing. Our nozzles remained clear and clog-free for weeks after the initial ink filling.

After formulating the surfactant-free inks, we studied the properties of the printed features to understand the role of annealing on the transport characteristics of the printed inks. This ink was used to print resistive device structures on both rigid SiO_2/Si and flexible polyimide substrates. Strain-dependent bending tests revealed that our printed features exhibited minimal change in electrical transport properties with strain, indicating intrinsic robustness of the graphene nanomembranes themselves, as well as good adherence of the printed features to the flexible polyimide substrates. The thermal stability of the printed features was also evaluated, where the change in resistance was measured as a function of temperature in the 6 K to 350 K range. When

temperature varies, most materials show a temperature dependent resistance change, as denoted by the temperature coefficient of resistance (TCR), where TCR can be positive if the resistance increases as temperature increases, and negative for the converse case. Additionally, for some applications a large TCR is desirable, such as thermistors and temperature sensors, where a small change in temperature should yield a large change in the resistivity for such devices to operate ideally. In other situations, a temperature independent TCR is needed, which are referred to as near-zero- (NZ)-TCR materials. Such materials are created intentionally to display this NZ-TCR characteristic; for example, bi-layer composites, comprising of polymers with a carbon nanotube base (having negative TCR) and a carbon black base (having positive TCR), yield a hybrid structure where resistance changes minimally with temperature with small TCR ~ 2% [138]. In this work, the smallest variation from the normalized resistance was found also to be less than 2% with a negative TCR throughout the entire measuring range (6 K to 350 K). In other material systems such as antiperovskites, an anomalous change in electronic transport from the metallic behavior is noted at 200 K where the NZ-TCR regime is noted due to correlated ionic moments aligning below 200 K [139]. Other inorganic composites with low or NZ-TCR behavior comprise of fine TaN/Cu particles in the tens of nm range, where the TCR value can be tuned by varying the TaN/Cu ratio [140]. We believe our work is the first report of a 2DLM based ink-jet printed device that exhibits a low TCR where resistance changes minimally with temperature. Thus, our surfactant-free dispersions yield not only printable and stable inks, but the resistive device structures formed with these inks display very low TCR values, and exhibit an electrical response that was immune to bending or mechanical strain, make them highly attractive for printed and flexible electronics.

5.1 METHODS AND MATERIALS

The solvents used in this work, Terpineol *(T)* (Sigma Aldrich #86480) and Cyclohexanone *(C)* (Sigma Aldrich #398241) were purchased from Sigma Aldrich and used as received to prepare ink mixtures at different ratios. The viscosity measurements were conducted using a Brookfield DV–E viscometer. The Graphite Rod (GR) (Sigma Aldrich #496553) was dispersed in the different solvent mixtures at a concentration of 10 mg/ml, and placed in a bath sonicator for 24 hours. A Branson 2800 bath sonicator was used for all sonication in this work. Supernatants from the dispersions were used for the optical absorption measurements. *Printing*. The DIMATIX 2831 material printer from Fujifilm was used for the ink jet printing, where the ink cartridges were purchased from the manufacturer and had a volume of 10 pl, with 16 nozzles and a nozzle diameter of ~ 21.5 μm. *Characterization:* SEM microscopy was carried out in a Hitachi S-4800. Electrical characterization was conducted using a micromanipulator 450PM-B probe stage equipped with a HP precision semiconductor parameter analyzer 4156A. A Lakeshore CRX–4K probe station was used to obtain the resistance as a function of temperature with a Keysight B1500-A Semiconductor Device Analyzer. Profilometer measurements were performed on the Brocker Dektak XT Stylus Profiler. *Substrate:* SiO_2/Si wafers with a 300 nm oxide layer and polyimide substrates were used for ink-jet printing.

5.2 VISCOSITY AND ABSORPTION MEASUREMENTS

The solvents *T* and *C* have been previously studied as dispersants for graphene by various groups, but in these prior reports the addition of a surfactant was also included in the formulations [11, 102]. Due to its higher viscosity, *T* can be used to tune the viscosity of the ink to achieve the recommended 10 cP for optimal printing. Various ratios of *T* in *C* were prepared and their viscosity was measured in order to find the optimum viscosity for ink-jet printing. Figure 5.1a shows the change in viscosity values for the *C/T* mixture; for example, with 0 % *T*, or 100 % *C* a viscosity

of 2 cP resulted, while 100 % *T* exhibited a viscosity ~ 36 cP. The optimum viscosity was achieved at 80 %*T* with a value of 10 cP.

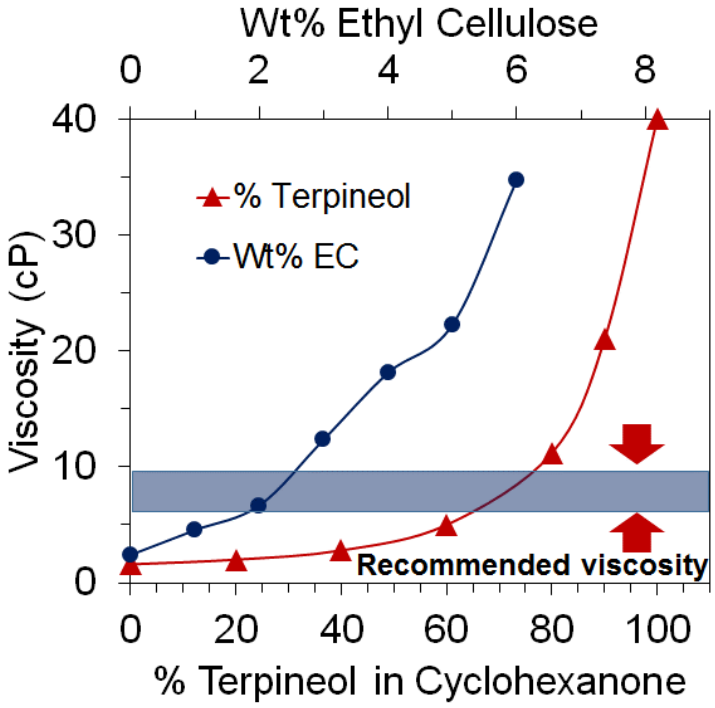

Figure 5.1: Change in viscosity values for different solvents. Primary horizontal axis showing % of Terpineol in Cyclohexanone (C/T) and secondary horizontal axis showing C/T (7:3) with increasing wt% of EC.

The secondary horizontal axis (on top) of Figure 5.1 shows the results of previously reported work in which the viscosity of a *C:T* mixture at a ratio of 7:3 solution was modified with the addition of EC [120]; we refer to this as the surfactant-assisted formulation for comparative purposes. The area of the optimum viscosity for printing is indicated by the blue shaded region on Figure 5.1.

The GR ink was prepared with different ratios of the *C:T* and the dispersions were allowed to stabilize overnight and the supernatant was used for characterization and printing optimization.

Optical absorbance spectroscopy was used to analyze the dispersions and the results obtained are shown on Figure 5.2a.

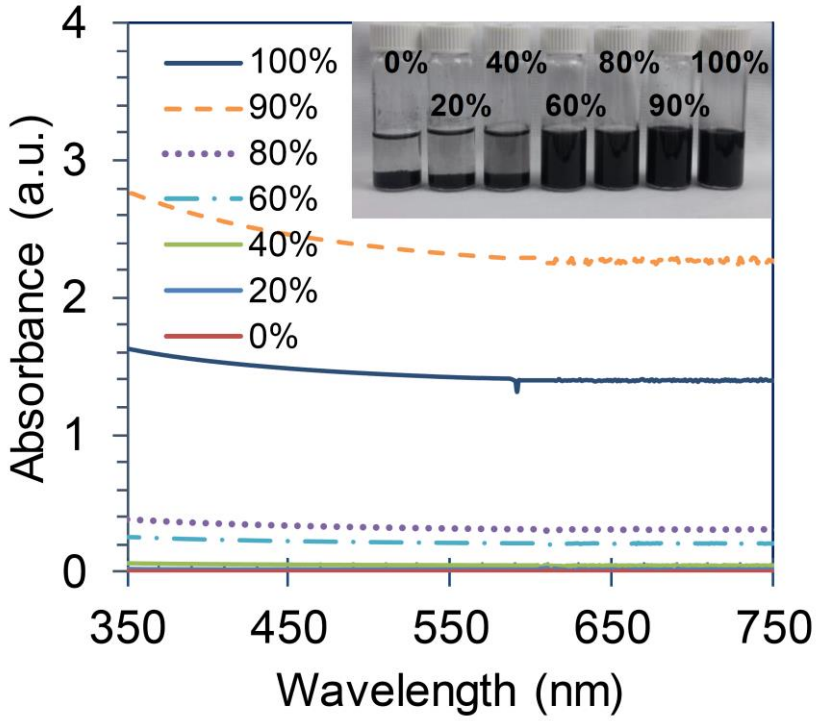

Figure 5.2: (a) Absorbance values obtained for the graphite rod (GR) dispersed in increasing percentage ratios of T in C. Insets showing vials of the GR dispersions in increasing percentage ratios of T in C.

Absorbance measurements revealed that as the concentration of *T* in the dispersion was increased, the absorption increased, where the highest absorbance was seen to occur at $T \sim 90$ %. This data clearly suggests that *T* has an important role to play in effectively exfoliating the graphite into nanomembranes, which is also corroborated by the optical images of the vials in the inset of Figure 5.2a, where the dispersions look darker in color as the % *T* increases.

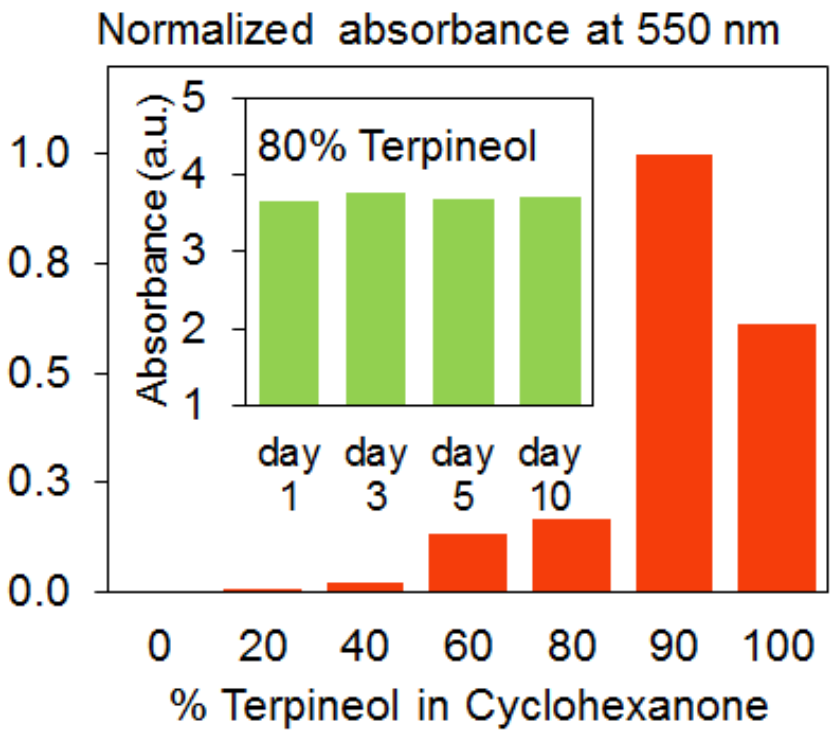

Figure 5.3: Normalized absorbance values at a wavelength of 550 nm of the GR dispersed in various percentages of C/T; inset shows the absorbance values for the prepared GR dispersions in 80% T taken as a function of time, indicating the dispersions to be stable with aging.

The enhanced exfoliation of graphite in *T* was further highlighted in Figure 5.3, which depicts the normalized absorbance values at a wavelength of 550 nm, and the increase in the absorbance as *T* increased is clearly evident, where a maximum is noted to occur at 90% *T*. However, we proceed with the ink formulation for *T* ~ 80%, given the fact that the viscosity for the 90 % case was close to 20 cP that fell well outside the optimal regime of 8 – 12 cP for viscosity suitable for ink-jet printing. The stability of the dispersions with time was evaluated and the data is shown in the inset of Figure 5.3, which shows the absorbance was unchanging with time over the course of 10 days.

5.3 ELECTRICAL CHARACTERIZATION MEASUREMENTS

After optimizing the rheological properties of our ink formulations, we began to explore the electronic transport characteristics of the dispersions once they were drop cast onto SiO_2/Si substrates and annealed for 1 hour at 350°C, prior to conducting the I-V measurements. Current-voltage (I-V) measurements were obtained for the graphite ink prepared at different ratios of *C:T*, and the results are shown in Figure 5.4. The graphite dispersed in 100% *T* showed the highest current values (1 mA at 1 V) with the current decreasing with reduced *T* concentration. Figure 5.4 demonstrates the resistance values generally decreasing as the % *T* increases in *C*.

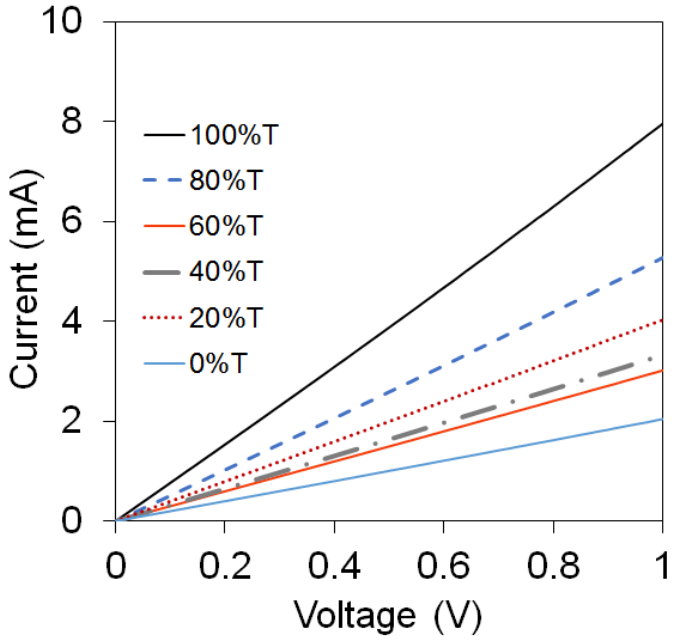

Figure 5.4: I-V measurements of the GR dispersed in different ratios of C/T that were drop casted onto SiO_2 /Si substrate and annealed for 1 hour at 350°C.

The insets in Figure 5.5 show microstructures of our drop cast samples that were obtained using Scanning Electron Microscopy (SEM). The 0% *T* dispersion shown at the top (100% *C*) displays nearly bulk platelets that exhibit voids and poor spatial uniformity. For the 80% *T* case

however (SEM shown in bottom inset), the exfoliated material formed a conductive film comprised of thinner and more uniform flakes which is consistent with the higher conductance values seen in this case. It was apparent from the structural characterization, as well as the electronic transport data, that a concentration of 80% *T* provided optimal exfoliation of the graphite.

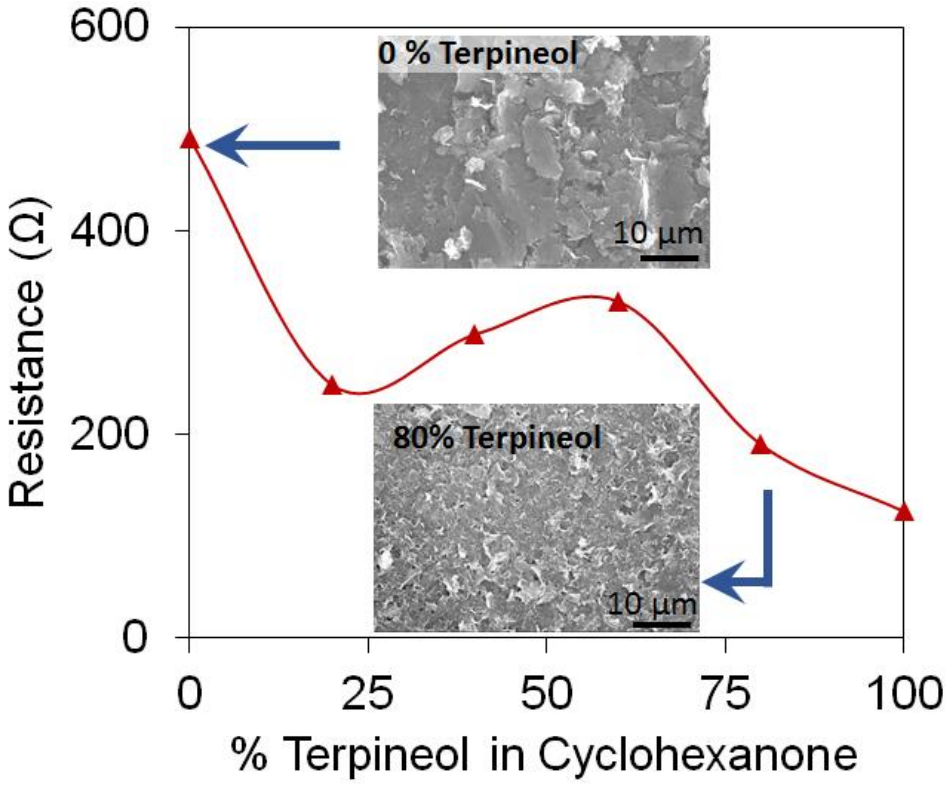

Figure 5.5: Resistance values obtained from the dispersions with different ratios of C/T. Insets of SEM micrographs of the surface morphology for dispersions made with 0% T or100% C (top) and 80% T (bottom).

Figure 5.6 shows I-V curves comparing the drop casted surfactant-free 80% *T* graphite ink (left vertical axis) and the surfactant-assisted graphite ink (right vertical axis); here the surfactant-

assisted ink comprises of EC and NMP, as noted earlier. Surfactant–free ink resulted in two orders of magnitude greater current values (5 mA at 1 V of applied voltage, or a resistance value ~189 Ω) compared to the surfactant-assisted ink (0.06 mA at 1 V, or a resistance value ~ 18 kΩ).

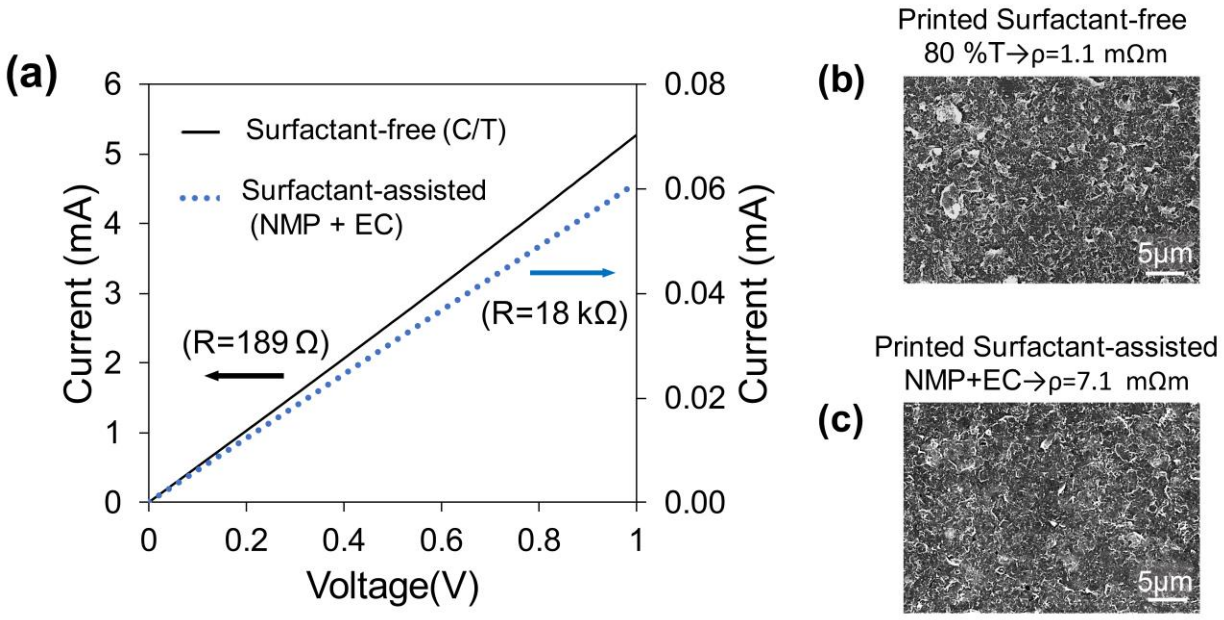

Figure 5.6: (a) I-V measurements resulting from the drop casted GR dispersion prepared with surfactant-free 80% *C/T* (80*T*) (primary vertical axis) and the surfactant-assisted GR dispersion (secondary vertical axis). SEM micrographs showing the resulting films after printing on SiO_2/Si substrate with (b) surfactant-free and (c) surfactant-assisted GR dispersions where ρ is 7X lower for the surfactant-free case.

Figures 5.6 (b) and (c) show SEM micrographs of the surfactant-free and surfactant-assisted film, respectively, resulting from GR inks. Both resulting films show large-area uniformity with approximately a similar platelet size; however, the continuous presence of the surfactant affects the resistivity ρ by remaining embedded within the material, since ρ ~ 7 mΩm and 1.13 mΩm, for the surfactant-assisted ink and surfactant-free inks, respectively. Ethyl Cellulose is a

polymer that possesses excellent membrane-forming ability and durability and is commonly used for flexible coatings for paper, cloth and leather, and as an electrical insulator. Ethyl Cellulose's thermoplastic characteristics and insulating properties have been studied mostly below 200°C, which is when decomposition is initiated [116]. Recent studies using thermogravimetric analysis (TGA) show two stages of the thermal degradation reaction for EC in the 180°C to 300°C region and at 370°C. Even at higher temperatures degradation of EC occurs slowly, and at 1000°C about 2% remains as residual mass [141]. It is no surprise that some EC will remain in the surfactant-assisted inks even after annealing [142], which is likely to compromise the formation of an intimate contact between respective graphene nanomembranes, reducing the overall electrical conductivity of the printed film. On the other hand, in the *T* based surfactant-free ink, the *T* has a lower boiling point ~ 215°C, and since our annealing temperatures are well above this, the prospect for residuals remaining is minimized, and the ensuing electrical conductivity is higher, as we observe here.

Figure 5.7 demonstrates the effect of the annealing temperature on the resistance of the prepared inks, once it was ink-jet printed onto the SiO_2/Si substrate, as shown by the image of the printed structure in the inset of Figure 5.7. The printed graphite patterns were annealed for either 1 hour or 2 hours, and the annealing temperature was varied from 200°C to 400°C; the resistance values are shown in Figure 5.7 as a function of the annealing temperature (vertical axis is logarithmic scale) for the two annealing times considered. Annealed samples at 200°C and 250°C showed very high resistance (10 MΩ and 100 MΩ). The resistance values were significantly reduced to the 300 kΩ range, when annealing temperatures were > 300°C. For annealing temperatures > 300°C, the resistance remained in the kΩ range for all annealing durations and temperatures tested, demonstrating that the minimum annealing temperature should be ~ 300°C to achieve low resistance printed films.

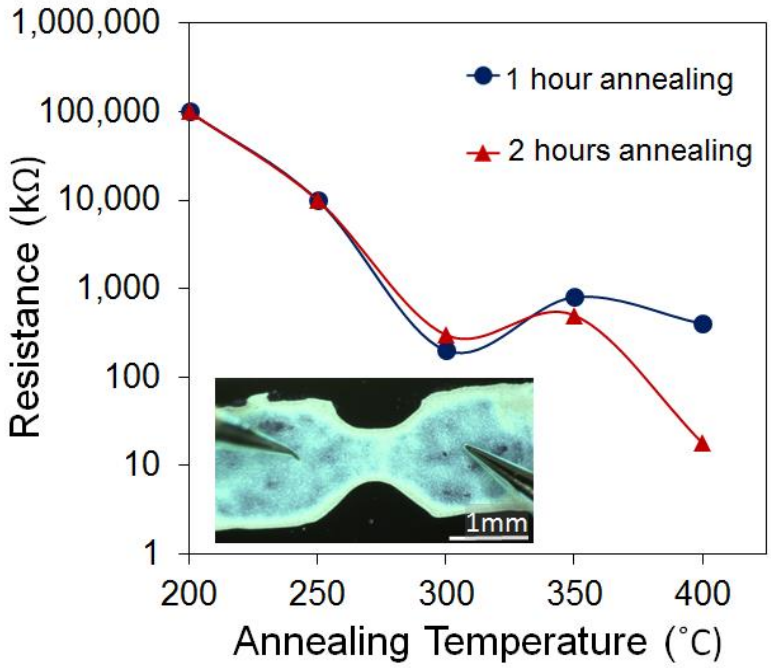

Figure 5.7: Resistance values for the printed ink after annealing for one and two hours at different temperatures. Inset showing printed pattern as probes are measuring.

The surfactant-free ink was used to print a pattern on SiO_2/Si and polyimide substrates at identical conditions (30 printing passes and annealed for 1 hour at 350°C). Figure 5.8 demonstrates the scaling of the resistance of the printed patterns as the separation between the probe tips increases. The inset of Figure 5.8 shows an optical image of the printed graphite film on the polyimide substrate. The printed film on polyimide shows lower linear sheet resistance values (1.4 kΩ/mm) compared to the one printed on the SiO_2/Si substrate (2.1 kΩ/mm) substrate which may have to do with the better substrate–thin film interaction and lower thermal mismatch of the polyimide substrate compared to the SiO_2/Si substrate after heat treatment [95]. Our surfactant-free inks were thus shown to be successfully ink-jet printed onto both rigid and flexible substrates.

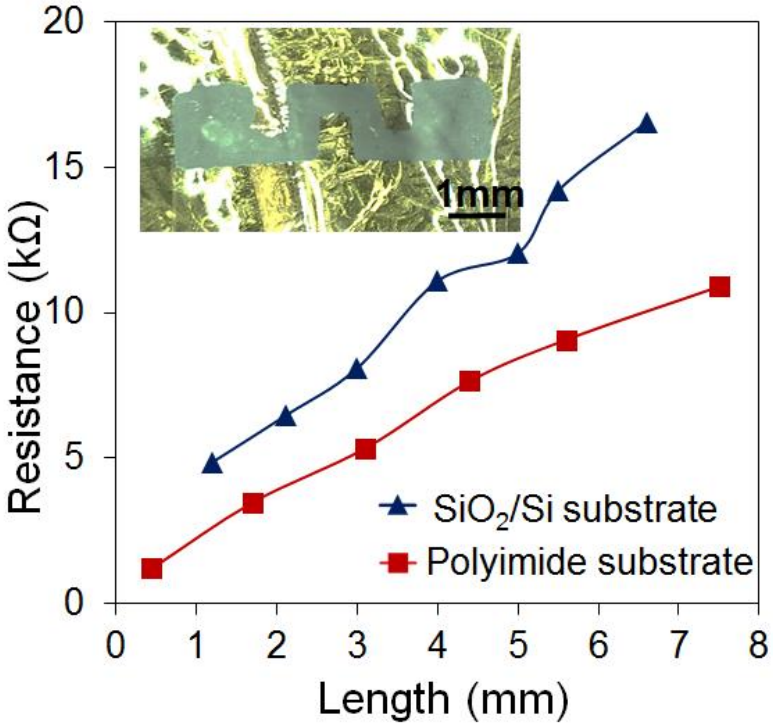

Figure 5.8: Change in resistance values with respect to the probe placement distance, of printed surfactant-free ink on SiO_2 /Si and polyimide substrates. Inset is optical image of printed ink on polyimide substrate.

5.4 MECHANICAL PROPERTIES

We proceeded to gauge the mechanical robustness of the printed structures which is important for flexible electronics. For flexible electronics applications, it is expected that the printed features will experience mechanical strain given the flexible, conformable nature of the substrates. Thus, it is important to validate the effect of mechanical strain on the electronic transport properties of the devices fabricated from the inks. In order to conduct this study, line patterns were printed on flexible polyimide substrates and then placed on substrate holders with a fixed radius of curvature and the data is shown in Figure 5.9. The test was performed by keeping

the distance between the probe tips constant at ~ 10 mm. The samples were tested at four radii of curvature, and the fixture for one such curvature is depicted in the inset of Figure 5.9.

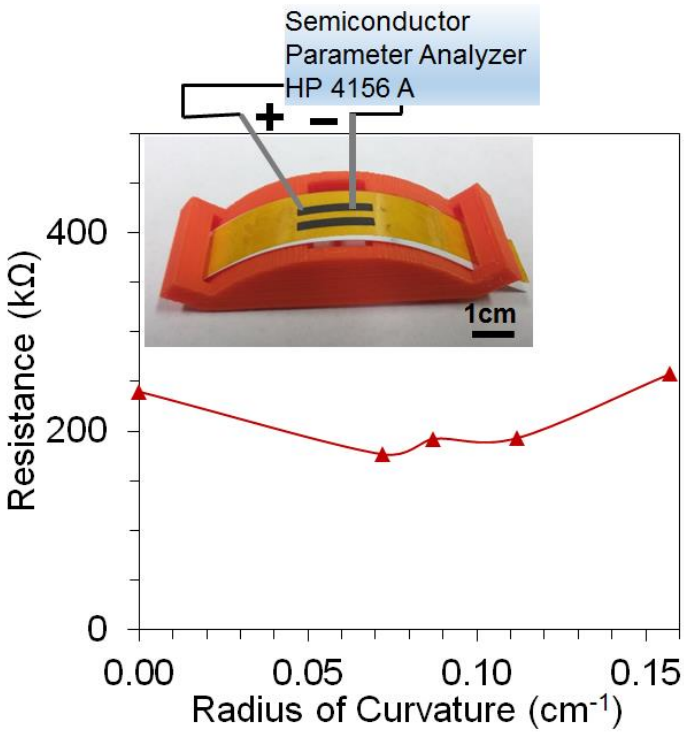

Figure 5.9: Resistance values changing with varying curvature radius. Inset showing schematic of the test fixture used for the strain-induced bending test.

Initially, there was a slight decrease in resistance during the first two bending positions, which was followed by an increase in resistance. As bending strain was induced, the graphene nanomembranes are likely to be initially compressed which decreases the membrane-to-membrane separation distance and hence enhances mechanical contact and the ensuing electrical transport. With increased bending however, the current decreases as the membranes start to separate with larger bending angles, and the larger inter-membrane separation leads to a reduction in the electrical transport. The resistance values obtained as the bending test was performed still resulted in a very small increase in resistance values from 239 kΩ (no bending case) to 257 kΩ (radius of

curvature ~ 0.157 cm^{-1}), which accounts for a total change in resistance of less than 8 %. Other conductive materials have previously been used for flexible substrates, such as one-dimensional (1D) silver nanowires or copper; however, they are more expensive, and due to the high aspect ratio of nanowires (i.e. diameter of 55 nm, length of 8.1 μm), it is extremely difficult to print such structures without blocking the nozzles. In addition, the density of these wires deposited per volume of liquid printed is low, making them impractical for printing. [143] The ink formulation prepared in this work utilizes very cheap, earth-abundant graphite where the 2D layered morphology is beneficial to ensuring larger contact area between nanomembranes that is also advantageous for mechanical resilience, compared to a network of 1D conductors.

5.5 Resistance vs Temperature Measurements

In order to evaluate the thermal stability of the surfactant-free inks, the resistance *R* versus temperature *T* characteristic was measured from 6 K to 350 K, as shown in Figure 5.10, using a cryogenic probe stage that was equipped with a closed cycle refrigerator. Metal contacts (Molybdenum) were deposited on SiO_2/Si substrates and graphene-based inks were then printed in between the Mo electrodes, as shown in the inset. Figure 5.10, displays the *R-T* characteristic for the surfactant-free and the surfactant-assisted ink for comparative analysis. Both inks displayed a negative temperature coefficient of resistance (TCR), where the **R** decreases with increasing *T*. In addition, on average, the surfactant-free ink demonstrates a lower TCR over the entire thermal range compared to the surfactant-assisted ink, with TCR calculated from 5-80 K, 80-200 K, and 200-350 K to be ~ 1 Ω/K, ~ 5 Ω/K, and 3 Ω/K, respectively.

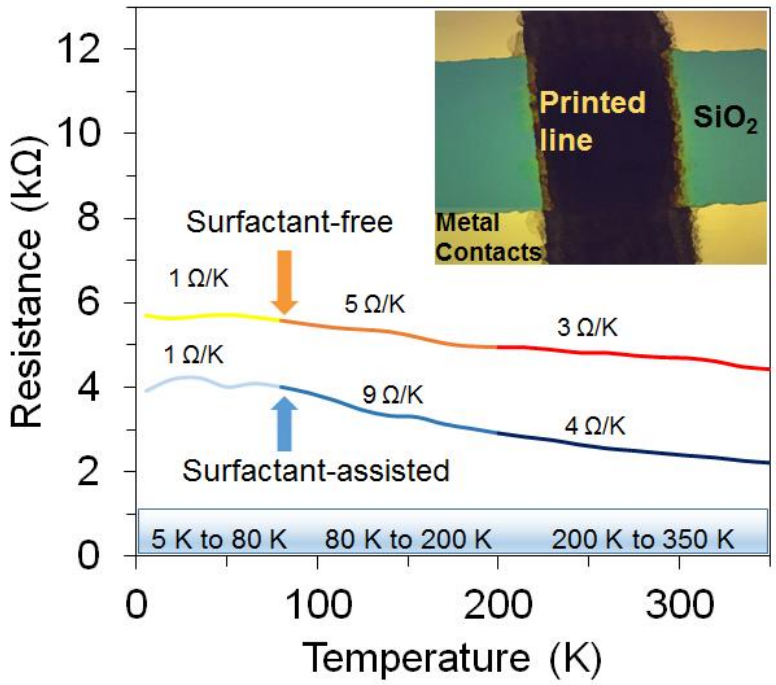

Figure 5.10: Resistance values of surfactant-free and surfactant-assisted ink printed on SiO_2/Si when subjected to different temperatures from 6 K to 350 K. Indicated are the three different temperature regimes and their respective average TCR denoted as Ω/K. Inset is an optical image of the ink-jet printed line connecting the Mo contacts on the SiO_2/Si substrate for which *R-T* data was obtained.

The variation of the resistance values of the surfactant-free ink with the increase in temperature can be calculated over the entire temperature range of 344 K (i.e. from 6 K to 350 K) to be ~ 3%. In contrast, the surfactant-assisted ink had higher TCR values in the three regimes of ~ 1 Ω/K, 9 Ω/K, and 4 Ω/K, respectively. In other reported materials, the range of temperatures studied is smaller (180 K [138]) with a variation in resistance of 2%. Therefore, the printed graphite film formed using a surfactant-free ink demonstrated minimal variation with temperature, that is attractive for applications where constant values of resistance over a wide range of temperatures maybe desirable for flexible electronics applications.

Chapter 6*:*

Conclusions

We have obtained high-quality inks using C/T and NMP as solvents for MoS_2 and graphite dispersion, respectively. NMP resulted in high GR nano-flake dispersion, low resistive printed pattern, and good printability. The addition of EC as a surfactant not only prevents the agglomeration of nanoparticles, but can be an important avenue for engineering the η of a solvent to make it suitable for ink-jet printing. The effect of EC in modifying θ_c of a solvent seems to be related to Pi of the solvent, with lower Pi (IPA and C/T) showing greater increase in θ_c for a given addition of EC. While EC has been added to the solution as surfactant before sonication in prior reports, we believe this reduces effective sonication power density to the individual particle clusters and reduces flake exfoliation efficacy. In our study we have noted that EC should be added to the solution mixture after sonication to prevent particle agglomeration, improve suspension stability, and achieve optimum solution viscosity for printing. We have observed GR with its layered structure results in higher nano-dispersed particle concentration in the aqueous suspension compared to GP. Furthermore, GR results in a more continuous film morphology, and low resistance after printing.

A graphite ink was prepared in NMP + EC and printed to produce a device that allows for power dissipation of up to 7W. Furthermore, this printed device demonstrates almost zero TCR over a wide temperature range. In order to fabricate such functional structures with ink-jet printing, the active nozzle number, printing passes, and annealing conditions are shown to play an important role to determine line resolution, and also dictate the morphological and electronic

transport characteristics of the printed graphene features. Raman shift as well as SEM characterization were used to confirm that the optimum temperature and time for post printing processing (annealing) of this device is one hour at 350 ˚C. The prepared ink can be used to print the device in rigid and flexible substrates as was demonstrated by printing in polyimide.

A surfactant-free printable and more environment friendly graphene ink was prepared that allows for lower temperature (350 ˚C) post printing processing. The ink was prepared in a mixture of Terpineol and Cyclohexanone (8:2) and was successfully printed with no surfactant added. This ink can be printed in rigid and flexible substrates and shows good flexible properties showing mechanical resilience. The resulting printed graphite film also performs with almost no change in resistance values over a wide range of temperatures.

References

[1] A. Geim and K. Novoselov, " The rise of graphene.," *Nature materials,* vol. 6, no. 3, pp. 183-191, 2007.

[2] S.-P. Chen, J. R. D. Retamal, D.-H. Lien, J.-H. He and Y.-C. Liao, "Inkjet-printed transparent nanowire thin film features for UV photodetectors," *RSC Advances, Royal Society of Chemistry,* vol. 5, no. 87, pp. 70707-70712, 2015.

[3] J. Chen, B. Yao, C. Li and G. Shi, "An improved Hummers method for eco-friendly synthesis of graphene oxide," *Carbon,* vol. 64, pp. 225-229, 2013.

[4] M. A. Ibrahem, T.-w. Lan, J. K. Huang, Y.-Y. Chen, K.-H. Wei, L.-J. Li and C. W. Chu, "High quantity and quality few-layers transition metal disulfide nanosheets from wet-milling exfoliation," *RSC Advances, Royal Society of Chemistry,* vol. 3, no. 32, pp. 13193-13202, 2013.

[5] L. Cai and C. Wang, "Carbon Nanotube Flexible and Stretchable Electronics," *Nanoscale research letters,* vol. 10, no. 1, pp. 1-21, 2015.

[6] Z. R. Robinson, S. W. Schmucker, K. M. McCreary and E. D. Cobas, "Chemical Vapor Deposition of Two-Dimensional Crystals," in *Handbook of Crystal Growth (Second Edition)*, 2015, pp. 785 - 833.

[7] A. Ayari, E. Cobas, O. Ogundadegbe and M. Fuhrer, "Realization and electrical characterization of ultrathin crystals of layered transition-metal dichalcogenides," *Journal of applied Physics,* vol. 101, p. 014507–014507, 2007.

[8] K. Kaasbjerg, K. Thygesen and K. Jacobsen, "Phonon-limited mobility in n-type single-layer MoS2 from first principles," *Physics Reviews,* vol. 85, 2012.

[9] M. Chowalla, H. Shin, G. Eda, L.-J. Li, K. Loh and H. Zhang, "The chemistry of two-dimensional layered transition metal dichalcogenide nanosheets," *Natural Chemistry,* vol. 5, pp. 263 - 75, 2013.

[10] J. Wilson and A. Yoffe, "The transition metal dichalcogenides discussion and interpretation of the observed optical, electrical and structural properties," *Advanced Physics,* vol. 18, pp. 193 - 335, 1969.

[11] E. B. Secor and M. C. Hersam, "Emerging Carbon and Post-Carbon Nanomaterial Inks for Printed Electronics," *The Journal of Physical Chemistry Letters, ACS Publications,* vol. 6, no. 4, pp. 620-626, 2015.

[12] V. Nicolosi, M. Chhowalla, M. G. Kanatzidis and M. S. Strano, "Liquid Exfoliation of Layered Materials," *Science,* vol. 340, p. 1226419, 2013.

[13] M. J. Allen, V. C. Tung and R. B. Kaner, "Honeycomb carbon: a review of graphene," *Chem.Rev.,* vol. 110, no. 1, pp. 132 - 145, 2009.

[14] G. Eda, G. Fanchini and M. Chhowalla, "Large-area ultrathin films of reduced graphene oxide as a transparent and flexible electronic material," *Nature nanotechnology,* vol. 3, no. 5, pp. 270-274, 2008.

[15] D. Dreyer, S. Park and R. S. Bielawski, "The chemistry of graphene oxide.," *Chemical Society Reviews,* vol. 39, p. 228, 2010.

[16] S. Stankovich, D. A. Dikin, R. D. Piner, K. A. Kohlhaas, A. Kleinhammes, Y. Jia, Y. Wu, S. T. Nguyen and R. S. Ruoff, "Synthesis of graphene-based nanosheets via chemical reduction of exfoliated graphite oxide," *Carbon,* vol. 45, no. 7, pp. 1558-1565, 2007.

[17] Y. Hernandez, V. Nicolosi, M. Lotya, F. M. Blighe, Z. Sun, S. De, I. McGovern, B. Holland, M. Byrne and Y. K. Gun'Ko, "High-yield production of graphene by liquid-phase exfoliation of graphite," *Nature nanotechnology,* vol. 3, no. 9, pp. 563-568, 2008.

[18] J. Coleman, M. Lotya, A. O'Neill, S. Bergin, P. King, U. Khan, K. Young, A. Gaucher, S. De and R. Smith, "Two-Dimensional Nanosheets Produced by Liquid Exfoliation of Layered Materials," *Science ,* vol. 568, no. 331, 2011.

[19] D. Li, M. B. Mueller, S. Gilje, R. B. Kaner and G. G. Wallace, "Processable aqueous dispersions of graphene nanosheets," *Nature nanotechnology,* vol. 3, no. 2, pp. 101-105, 2008.

[20] P. Sungjin, A. Jinho, J. Inhwa, R. D. Piner and Sung, "Colloidal Suspensions of Highly Reduced Graphene," *Nano letters,* vol. 9, no. 4, pp. 1593-1597, 2009.

[21] J. Li, M. C. Lemme and M. Östling, "Inkjet Printing of 2D Layered Materials," *ChemPhysChem,* vol. 15, no. 16, pp. 3427-334, 2014.

[22] M. Singh, H. M. Haverinen, P. Dhagat and G. E. Jabbour, "Inkjet printing process and applications," *Advanced Materials ,* vol. 22, pp. 673 - 685, 2010.

[23] H. Yan, Z. Chen, Y. Zheng, C. Newman, J. R. Quinn and F. Dötz, "A High-Mobility Electron-Transporting Polymer for Printed Transistors," *Nature ,* vol. 457, pp. 679 - 686, 2009.

[24] E. B. Secor, "Inkjet Printing of High Conductivity, Flexible Graphene Patterns," *the journal of physical chemistry letters,* 2013.

[25] B. Cook, B. Tehrani, J. Cooper, S. Kim and M. Tentzeris, "Integrated printing for 2D/3D flexible organic electronic devices," in *Handbook of Flexible Organic Electronics*, Atlanta GA, USA, Georgia Tech, 2015, pp. 199-216.

[26] D. Soltman and V. Subramanian, "Inkjet-printed line morphologies and temperature control of the coffee ring effect," *Langmuir, ACS Publications,* vol. 24, no. 5, pp. 2224-2231, 2008.

[27] B. Derby, "Inkjet Printing of Functional and Structural Materials: Fluid Property Requirements, Feature Stability, and Resolution," *Annu. Rev. Mater. Res. 2010. 40:395–414,* vol. 40, p. 395–414, 2010.

[28] B. Derby and N. Reis, "Inkjet printing of highly loaded particulate suspensions," *MRS Bull, Cambridge Univ Press,* vol. 28, no. 11, pp. 815-818, 2003.

[29] S. Di Risio and N. Yan, "Piezoelectric Ink-Jet Printing of Horseradish Peroxidase: Effect of Ink Viscosity Modifiers on Activity," *Macromolecular Rapid Communications, Wiley Online Library,* vol. 28, no. 18-19, pp. 1934-1940, 2007.

[30] Y. T. Liang and M. C. Hersam, "Highly concentrated graphene solutions via polymer enhanced solvent exfoliation and iterative solvent exchange," *J.Am.Chem.Soc., ACS Publications,* vol. 132, no. 50, pp. 17661-17663, 2010.

[31] J. Li, F. Ye, S. Vaziri, M. Muhammed, M. C. Lemme and M. Östling, "Efficient inkjet printing of graphene," *Adv Mater, Wiley Online Library,* vol. 25, no. 29, pp. 3985-3992, 2013.

[32] F. Torrisi, T. Hasan, W. Wu, Z. Sun, A. Lombardo, T. S. Kulmala, G.-W. Hsieh, S. Jung, F. Bonaccorso and P. J. Paul, "Inkjet-printed graphene electronics," *Acs Nano,* vol. 6, no. 4, pp. 2992-3006, 2012.

[33] M. Lotya, Y. Hernandez, P. J. King, R. J. Smith and V. Nicolosi, "Liquid Phase Production of Graphene by Exfoliation of Graphite in Surfactant/Water Solutions," *Journal American Chemistry Society,* vol. 131, pp. 3611 - 3620, 2009.

[34] H. Li, "Mechanical Exfoliation and Characterization of Singleand," *nanosheets,* p. 1974–1981, 2013.

[35] S. Satoru, T. Yusuke, F. Kazuaki and W. Gregory, "Graphene Growth from Spin-Coated Polymers without a Gas," *Japanese Journal for applied Physics,* vol. 51, 2012.

[36] M. Gall, Rut'kov and A. Tontegode, "Nature of the adsorption binding between a graphite monolayer and rhomium surface," *Soviet Physics Journal,* vol. Solid State, no. 27, pp. 1410 - 4, 1985.

[37] Y. Gamo, A. Nagashima, M. Wakabayashi, M. Terai and C. Oshima, "Atomic structure of monolayer graphite formed on Ni," *Surface Science,* vol. 61, no. 4, p. 374, 1997.

[38] I. Alstrup, I. Chorkendorff and S. Ullmann, "The interaction of CH4 at high temperatures with clean and oxygen covered Cu," *Surface science,* pp. 264 - 95, 1992.

[39] M. Batzill, "The surface science of graphene: metal interfaces, CVD synthesis, nanoribbons, chemical modifications, and defects," *Surface Science,* vol. 67, pp. 83 - 115, 2012.

[40] H. Cao, Q. Yu, L. Jauregui, J. Tian, W. Wu and Z. Liu, "Electronic transport in chemical vapor deposited graphene synthesized on Cu: quantum Hall effect and weak localization," *Applied Physics Letters,* vol. 96, p. 122106–122106, 2010.

[41] M. Bresnehan, M. Hollander, M. Wetherington, K. Wang, T. Miyagi and G. Pastir, "Prospects of direct growth boron nitride films as substrates for graphene electronics.," *Journal of Materials Resources,* vol. 29, pp. 459 - 71, 2014.

[42] S. Arya and D. A. , "Preparation, properties and applications of boron nitride thin films," *Thin Solid films,* vol. 157, pp. 267 - 82, 1988.

[43] Z. Q. Ganatra R, "Few layer MoS2–A promising layered semiconductor," *ACS Nano,* vol. 8, pp. 4074 - 99, 2014.

[44] F. Torrisi et al., "Inkjet-printed graphene electronics," *Nano ,* vol. 6, p. 2992, 2012.

[45] J. N. Coleman et al., "Two-dimensional nanosheets produced by liquid exfoliation of layered materials.," *Science ,* no. 331, p. 568, 2011.

[46] J. N. Coleman, "Liquid exfoliation of defect-free graphene.," *Science,* 2013.

[47] M. Lotya, P. King, U. Khan, S. De and J. Coleman, "High-concentration, surfactant-stabilized graphene dispersions," *Nano,* vol. 4, p. 3155, 2010.

[48] A. Ciesielski and P. Samorì, "Graphene via sonication assisted liquid-phase exfoliation," *Chem.Soc.Rev., 2014, 43, 1, 381-398,* vol. 43, no. 1, pp. 381 - 398, 2014.

[49] X. Han, Y. Chen, H. Zhu, C. Preston, J. Wan, F. Z and L. Hu, "Scalable, printable, surfactant-free graphene ink directly from graphite," *Nanotechnology,* vol. 24, 2013.

[50] N. Behabtu, J. R. Lomeda, M. J. Green and A. L. Higginbotham, "Spontaneous High-Concentration Dispersions and Liquid Crystals of Graphene.," *Nat. Nanotechnol,* 2010.

[51] D. Golberg, B. Yoshio, H. Yang, T. Takeshi, M. Masanori, T. Chengchun and Z. Chunyi, "Boron nitride nanotubes and nanosheets," *ACS Nano,* vol. 4, no. 6, p. 29792931, 2010.

[52] P. May, U. Khan, J. Hughes and J. Coleman, "Role of solubility parameters in understanding the steric stabilization of exfoliated two-dimensional nanosheets by adsorbed polymers.," *J. Phys. Chem.,* vol. 116, p. 11393, 2012.

[53] R. J. Smith, P. J. King, M. Lotya, C. Wirtz, U. Khan, S. De and A. Arlene O'Neill, "Large-scale exfoliation of inorganic layered compounds in aqueous surfactant solutions.," *Advanced Materials,* vol. 23, no. 34, pp. 3944-3948, 2011.

[54] T. H. Joong, I. J. Jeong, K. Haena, Y. H. Jun, K. Y. Hyung and S. W. Jong, "Extremely Efficient Liquid Exfoliation and Dispersion of Layered Materials by Unusual Acoustic Cavitation," *Scientific Reports,* pp. 1 - 7, 2014.

[55] S. L. Chang, S. Costel and M. Waleed, "Synthesis of conductive transparent few - layer grahene directly on glass at 450 C," *Nanotechnology,* vol. 23, no. june 15, pp. 1 - 6, 2012.

[56] G. Kim, A.-R. Jang, H. Jeong, Z. Lee, D. Kang and H. Shin, "Growth of high-crystalline, single-layer hexagonal boron nitride on recyclable platinum foi," *Nano Letters,* vol. 13, pp. 1834 - 9, 2013.

[57] Y.-C. Lin, W. Zhang, J.-K. Huang, K.-K. Liu, Y.-H. Lee, C.-T. Liang and e. al, "Wafer-scale MoS2 thin layers prepared by MoO3 sulfurization.," *Nanoscale,* vol. 4, pp. 6637 - 41, 2012.

[58] Y. Zhan, Z. Liu, S. Najmaei, P. Ajayan and J. Lou, "Large-area vapor-phase growth and characterization of MoS2 atomic layers on a SiO_2 substrate.," *Small,* vol. 8, pp. 966 - 71, 2012.

[59] Y. Lee, J. Lee, H. Bark, I.-K. Oh, G. Ryu, Z. Lee and e. al, "Synthesis of wafer-scale uniform molybdenum disulfide films with control over the layer number using a gas phase sulfur precursor," *Nanoscale,* vol. 6, pp. 2821 - 6, 2014.

[60] D. Makarov, D. Karnaushenko and O. G. Schmidt, "Printable Magnetoelectronics," *ChemPhysChem,* vol. 14, no. 9, pp. 1771-1776, 2013.

[61] M. Muccini, "A Bright Future for Organic Field-effect Transistors," *Nat. Mater.,* vol. 5, no. 8, pp. 605-613, 2006.

[62] L. Viculis, J. Mack and R. Kaner, "A Chemical Route to Carbon Nanoscrolls," *Science,* vol. 299, no. 5611, p. 1361, 2003.

[63] G. Chen, W. Weng, D. Wu, C. Wu, J. Lu, P. Wang and X. Chen, "Preparation and characterization of graphite nanosheets from ultrasonic powdering technique," *Carbon,* vol. 42, no. 4, pp. 753-759, 2004.

[64] M. Jana, S. Saha, P. Khanra, P. Samanta, H. Koo, N. C. Murmu and T. Kuila, "Non-covalent functionalization of reduced graphene oxide using sulfanilic acid azocromotrop and its application as supercapacitor electrode material," *Journal of Materials Chemistry A,* vol. 3, no. 14, pp. 7323-7331, 2015.

[65] K. R. Paton, E. Varrla, C. Backes, R. J. Smith, U. Khan, A. O'Neill, C. Boland, M. Lotya, O. M. Istrate and P. King, "Scalable production of large quantities of defect-free few-layer graphene by shear exfoliation in liquids," *Nature materials,* vol. 13, no. 6, pp. 624 - 630, 2014.

[66] U. Khan, H. Porwal, A. O'Neill, K. Nawaz, P. May and J. N. Coleman, "Solvent-exfoliated graphene at extremely high concentration," *Langmuir,* vol. 27, no. 15, pp. 9077 - 9082, 2011.

[67] U. Khan, A. O'Neill, M. Lotya, S. De and J. N. Coleman, "High-Concentration Solvent Exfoliation of Graphene," *Small,* vol. 6, no. 7, pp. 864 - 871, 2010.

[68] P. V. Kamat, "Manipulation of Charge Transfer Across Semiconductor Interface. A Criterion That Cannot Be Ignored in Photocatalyst Design," *The journal of physical chemistry letters,* vol. 3, no. 5, pp. 663-672, 2012.

[69] S. Park and R. S. Ruoff, "Chemical methods for the production of graphenes," *Nature nanotechnology,* vol. 4, no. 4, pp. 217 - 224, 2009.

[70] J. Li, F. Ye, S. Vaziri, M. Muhammed, M. C. Lemme and M. Östling, "A simple route towards high-concentration surfactant-free graphene dispersions.," *Carbon,* vol. 50, no. 8, pp. 3113-3116., 2012.

[71] B. V. Antohe and D. B. Wallace, "Acoustic phenomena in a demand mode piezoelectric ink jet printer," *J Imaging Sci Technol.,* vol. 46, no. 5, pp. 409 - 414, 2002.

[72] N. Reis, C. Ainsley and B. Derby, "Ink-jet delivery of particle suspensions by piezoelectric droplet ejectors," *J.Appl.Phys.,,* vol. 97, no. 9, pp. 94-103, 2005.

[73] S. O. Kasap, Principles of electrical engineering materials and devices, McGraw-Hill Companies, 2000.

[74] H. P. Le, "Progress and trends in ink-jet printing technology," *J Imaging Sci Technol.,* vol. 42, no. 1, pp. 49 - 62, 1998.

[75] H. Gan, X. Shan, T. Eriksson, B. K. Lok and Y. C. Lam, "Reduction of droplet volume by controllilng actuating waveforms in inkjet printing for micro-pattern formation," *Journal of micromechanics and microengineering,* pp. 1-8, 2009.

[76] O. A. Basaran, "Small-scale free surface flows with breakup: Drop formation and emerging applications," *AIChE J.,* vol. 48, no. 9, pp. 1842-1848, 2002.

[77] B. Gans, E. Kazancioglu, W. Meyer and U. S. Schubert, "Ink-jet Printing Polymers and Polymer Libraries Using Micropipettes," *Macromolecular Rapid Communications,* vol. 25, no. 1, pp. 292 - 296, 2004.

[78] J. Y. Hwang, M. K. Kim, S. H. Lee, K. Kang, H. Kang and Y. J. Cho, "A Study on Driving Waveform of a Piezoelectric inkjet Print Head," *Internat. Soc. for Optics and Photonics,* pp. 67170T-67170T-9, 2007.

[79] S. Bidoki, D. Lewis, M. Clark, A. Vakorov, P. Millner and D. McGorman, "Ink-jet fabrication of electronic components," *J Micromech Microengineering,* vol. 17, no. 5, p. 967, 2007.

[80] H. J. Shore and G. M. Harrison, "The effect of added polymers on the formation of drops ejected from a nozzle," *Physics of Fluids ,* vol. 17, no. 3, p. 033104, 2005.

[81] H. Dong, W. W. Carr and J. F. Morris, "An experimental study of drop-on-demand drop formation," *Physics of Fluids (1994-present),* vol. 18, no. 7, p. 072102, 2006.

[82] P. K. Notz, A. U. Chen and O. A. Basaran, "Satellite drops: Unexpected dynamics and change of scaling during pinch-off," *Physics of Fluids (1994-present),* vol. 13, no. 3, pp. 549 - 552, 2001.

[83] Y.-F. Liu, M.-H. Tsai, Y.-F. Pai and W.-S. Hwang, "Control of Droplet Formation by Operating Waveform for Inks with Various Viscosities in Piezoelectric Inkjet Printing," *Applied Physics A.,* vol. 111, no. 2, pp. 509 - 516, 2013.

[84] A. Capasso, A. D. R. Castillo, H. Sun, A. Ansaldo, V. Pellegrini and F. Bonaccorso, "Ink-jet printing of graphene for flexible electronics: An environmentally-friendly approach," *Solid State Commun,* vol. 224, pp. 53-63, 2015.

[85] L. Huang, Y. Huang, J. Liang, X. Wan and Y. Chen, "Graphene-based conducting inks for direct inkjet printing of flexible conductive patterns and their applications in electric circuits and chemical sensors," *Nano Research,* vol. 4, no. 7, pp. 675-684, 2011.

[86] R. Crooks and D. V. Boger, "Influence of fluid elasticity on drops impacting on dry surfaces," *Journal of Rheology (1978-present),* vol. 44, no. 4, pp. 973 - 996, 2000.

[87] C. Stow and M. Hadfield, "An experimental investigation of fluid flow resulting from the impact of a water drop with an unyielding dry surface," *The Royal Society,* vol. 373, no. 1755, pp. 419 - 441, 1981.

[88] R. L. Vander Wal, G. M. Berger and S. D. Mozes, "The combined influence of a rough surface and thin fluid film upon the splashing threshold and splash dynamics of a droplet impacting onto them," *Exp.Fluids,* vol. 40, no. 1, pp. 23 - 32, 2006.

[89] T. Young, "An essay on the cohesion of fluids," *Philosophical Transactions of the Royal Society of London,* vol. 95, pp. 65 - 87, 1805.

[90] P. C. Duineveld, "The stability of ink-jet printed lines of liquid with zero receding contact angle on a homogeneous substrate," *J.Fluid Mech.,* vol. 477, pp. 175 - 200, 2003.

[91] P. Hsu, R. Bhattacharya, H. Gleskova, M. Huang, Z. Xi, Z. Suo, S. Wagner and J. Sturm, "Thin-film transistor circuits on large-area spherical surfaces," *Appl.Phys.Lett.,* vol. 81, no. 9, pp. 1723 - 1725, 2002.

[92] R. Bhattacharya, S. Wagner, Y.-J. Tung, J. R. Esler and M. Hack, "Organic LED pixel array on a dome," *Proc IEEE,* vol. 93, no. 7, pp. 1273 - 1280, 2005.

[93] S. P. Lacour, S. Wagner, Z. Huang and Z. Suo, "Stretchable gold conductors on elastomeric substrates," *Appl.Phys.Lett.,* vol. 82, no. 15, pp. 2404 - 2406, 2003.

[94] D. S. Gray, J. Tien and C. S. Chen, "High-conductivity elastomeric electronics," *Adv Mater.,* vol. 16, no. 5, pp. 393 - 397, 2004.

[95] W. S. Wong and A. Salleo, Flexible Electronics: Materials and Applications, Springer Science & Business Media, 2009.

[96] S. Park, M. Vosguerichian and Z. Bao, "A review of fabrication and applications of carbon nanotube film-based flexible electronics," *Nanoscale,* vol. 5, no. 5, pp. 1727 - 1752, 2013.

[97] S. Swapp, "Scanning Electron Microscopy (SEM)," University of Wyoming, 2006.

[98] J. Goldstein, D. E. Newbury, P. Echlin, D. C. Joy, A. D. Romig Jr, C. E. Lyman, C. Fiori and E. Lifshin, Scanning electron microscopy and X-ray microanalysis: a text for biologists, materials scientists, and geologists, Springer Science & Business Media, 2012,.

[99] R. F. Egerton, Physical principles of electron microscopy: an introduction to TEM, SEM, and AEM, Springer Science & Business Media, 2006.

[100] A. Handbook, Materials Characterization, ASM International, 1986.

[101] P. Misra and M. A. Dubinskii, "Ultraviolet spectroscopy and UV lasers," CRC Press, 2002.

[102] Y. Gao, W. Shi, W. Wang, Y. Leng and Y. Zhao, "Inkjet Printing Patterns of Highly Conductive Pristine Graphene on Flexible Substrates," *Ind Eng Chem Res.,* vol. 53, no. 43, pp. 16777 - 16784, 2014.

[103] A. Kaul, "Two-dimensional layered materials: Structure, properties, and prospects for device applications," *Journal for Materials Research,* vol. 29, no. 3, pp. 348 - 361, 2014.

[104] S. T. Hobeom Kim1, "Organic solar cells using CVDgrown graphene electrodes," *Nanotechnology,* vol. 25, 2014.

[105] A. C. Ferrari, "Raman spectroscopy of graphene and graphite: disorder, electron–phonon coupling, doping and nonadiabatic effects.," *Solid State Commun., 2007, 143, 1, 47-57,* vol. 143, no. 1, pp. 47 - 57, 2007.

[106] A. Ferrari, J. Meyer, V. Scardaci, C. Casiraghi, M. Lazzeri, F. Mauri, S. Piscanec, D. Jiang, K. Novoselov and S. Roth, "Raman spectrum of graphene and graphene layers," *Phys.Rev.Lett.,* vol. 97, no. 18, p. 187401, 2006.

[107] A. Eckmann, A. Felten, A. Mishchenko, L. Britnell, R. Krupke, K. S. Novoselov and C. Casiraghi, "Probing the nature of defects in graphene by Raman spectroscopy," *Nano letters,* vol. 12, no. 8, pp. 3925 - 3930, 2012.

[108] I. M. Hutchins and G. D. Martinn, Inkjet Technology for Digital Fabrication, Cambridge, UK: Wiley, 2013.

[109] G. D. Martin, S. D. Hoath and I. M. Hutchings, "Inkjet printing-the physics of manipulating liquid jets and drops," *IOP Publishing,* vol. 105, no. 1, p. 012001, 2008.

[110] D. Jang, D. Kim and J. Moon, "Influence of Fluid Physical Properties on Ink-Jet Printability," *Langmuir,* vol. 25, no. 5, pp. 2629-2635, 2009.

[111] X. Li, G. Zhang, X. Bai, X. Sun, X. Wang, E. Wang and H. Dai, "Highly Conducting Graphene Sheets and Langmuir−Blodgett Films.," *Nat. Nanotechnol,* vol. 3, no. 9, pp. 538 - 542, 2008.

[112] M. Anyfantakis and D. Baigl, "Manipulating the Coffee-Ring Effect: Interactions at Work," *ChemPhysChem,* vol. 16, no. 13, pp. 2726-2734, 2015.

[113] J. Wang, L. Chen, W. Lu, M. Zeng, L. Tan, F. Ren, C. Jiang and L. Fu, "Direct growth of molybdenum disulfide on arbitrary insulating surfaces by chemical vapor deposition," *RSC Advances,* vol. 5, no. 6, pp. 4364-4367, 2015.

[114] A. Castellanos-Gomez, J. Quereda, H. P. van der Meulen, N. Agraït and G. Rubio-Bollinger, "Spatially resolved optical absorption spectroscopy of single-and few-layer MoS2 by hyperspectral imaging," *Nanotechnology,* vol. 27, no. 11, p. 115705, 2016.

[115] D. Fadil, H. R. Fayaz, G. Lara and A. B. Kaul, "Electrical Transport and Hot–Luminescence Effects in Exfoliated MoS_2 and WS2 2D-Materials".

[116] M. Davidovich-Pinhas, S. Barbut and A. Marangoni, "Physical structure and thermal behavior of ethylcellulose," *Cellulose,* vol. 21, no. 5, pp. 3243-3255, 2014.

[117] S. Niyogi, E. Bekyarova, M. E. Itkis, J. L. McWilliams, M. A. Hamon and R. C. Haddon, "Solution properties of graphite and graphene," *J.Am.Chem.Soc,* vol. 128, no. 24, pp. 7720-7721, 2006.

[118] J. C. Meyer, A. K. Geim, M. Katsnelson, K. Novoselov, T. Booth and S. Roth, "The structure of suspended graphene sheets," *Nature,* vol. 446, no. 7131, pp. 60-63, 2007.

[119] M. Michel, J. A. Desai, C. Biswas and A. B. Kaul, "Optimization of Fluid Characteristics of 2D Materials for Inkjet Printing," *MRS Advances ,* vol. 1, no. 30, pp. 2199-2206, 2016.

[120] M. Michel, J. Desai, C. Biswas and A. Kaul, "Engineering Chemically Exfoliated Dispersions of Two-dimensional Graphite and Molybdenum Disulphide for Ink-Jet Printing," *Nanotechnology,* (in press) 2016.

[121] I. Calizo, A. Balandin, W. Bao, F. Miao and C. Lau, "Temperature Dependence of the Raman Spectra of Graphene and Graphene Multilayers," *Nano Lett.,* vol. 7, no. 9, pp. 2645 - 2649, 2007.

[122] R. Vidano, D. Fischbach, L. Willis and T. Loehr, "Observation of Raman band shifting with excitation wavelength for carbons and graphites," *Solid State Commun., 1981, 39, 2, 341-344,* vol. 39, no. 2, pp. 341 - 344, 1981.

[123] A. C. Ferrari, "Raman Spectroscopy of Graphene and Graphite: Disorder, Electron–phonon Coupling, Doping and Nonadiabatic Effects.," *Solid State Commun., 2007, 143, 1, 47-57,* vol. 143, no. 1, pp. 47 - 57, 2007.

[124] W. Wang, Q. Peng, Y. Dai, Z. Qian and S. Liu, "Temperature Dependence of Raman Spectra of Graphene on Copper Foil Substrate," *J.Mater.Sci.,* vol. 27, no. 4, pp. 3888 - 3893, 2016.

[125] A. Eckmann, A. Felten, A. Mishchenko, L. Britnell, R. Krupke, K. S. Novoselov and C. Casiraghi, "Probing the Nature of Defects in Graphene by Raman Spectroscopy," *Nano Lett.,* vol. 12, no. 8, pp. 3925 - 3930, 2012.

[126] S. Tian, Y. Yang, Z. Liu, C. Wang, R. Pan, C. Gu and J. Li, "Temperature-dependent Raman Investigation on Suspended Graphene: Contribution from Thermal Expansion Coefficient Mismatch Between Graphene and Substrate," *Carbon,* vol. 104, pp. 27 - 32, 2016.

[127] M. J. Allen, J. D. Fowler, V. C. Tung, Y. Yang, B. H. Weiller and R. B. Kaner, "Temperature dependent Raman spectroscopy of chemically derived graphene.," *Appl. Phys. Lett.,* vol. 93, no. 19, p. 193119, 2008.

[128] L. B. Kish, "End of Moore's law: thermal (noise) death of integration in micro and nano electronics," *Phys. Lett. A,* vol. 305, no. 3, pp. 144 - 149, 2002.

[129] R. Courtland, "Transistors could stop shrinking in 2021," *IEEE Spectrum,* vol. 53, no. 9, pp. 9-11, 2016.

[130] C. Yan, J. Wang and P. S. Lee, "Stretchable Graphene Thermistor with Tunable Thermal Index," *ACS nano,* vol. 9, no. 2, pp. 2130 - 2137, 2015.

[131] J. D. Renteria, D. L. Nika and A. A. Balandin, "Graphene thermal properties: applications in thermal management and energy storage," *Appl. Sci.,* vol. 4, no. 4, pp. 525 - 547, 2014.

[132] D. Kong, L. T. Le, Y. Li, J. L. Zunino and W. Lee, "Temperature-dependent Electrical Properties of Graphene Inkjet-printed on Flexible Materials," *Langmuir,* vol. 28, no. 37, pp. 13467 - 13472, 2012.

[133] K. Chu, S.-C. Lee, S. Lee, D. Kim, C. Moon and S.-H. Park, "Smart Conducting Polymer Composites Having Zero Temperature Coefficient of Resistance," *Nanoscale,* vol. 7, no. 2, pp. 471 - 478, 2015.

[134] R. a. S. L. H. Shah, "Method of making zero temperature coefficient of resistance resistors," *U.S. Patent,* Vols. 4,579,600, 1986.

[135] H. Al-Mumen, F. Rao, L. Dong and W. Li, "Design, Fabrication, and Characterization of Graphene Thermistor," *IEEE,* pp. 1135 - 1138, 2013.

[136] L. Ding, C. Wang, L. Chu, J. Yan, Y. Na, Q. Huang and X. Chen, "Near Zero Temperature Coefficient of Resistivity in Antiperovskite Mn3Ni1− xCuxN.," *App. Phys. Lett.,* vol. 99, no. 25, p. 251905, 2011.

[137] J. Kang, H. Kim, K. S. Kim, S. K. Lee, S. Bae, J. H. Ahn and B. H. Hong, "High-performance Graphene-based Transparent Flexible Heaters," *Nano Lett.,* vol. 11, no. 12, pp. 5154 - 5158, 2011.

[138] K. Chu, S. C. Lee, S. Lee, D. Kim, C. Moon and S.-H. Park, "Smart conducting polymer composites having zero temperature coefficient of resistance," *Nanoscale,* vol. 7, no. 2, pp. 471 - 478, 2015.

[139] L. Ding, W. Cong, C. Lihua, Y. Jun, N. Yuanyuan, H. Qingzhen and C. Xiaolong, "Near zero temperature coefficient of resistivity in antiperovskite Mn3Ni1− xCuxN," *Appl. Phys. Lett.,* vol. 99, no. 25, p. 251905, 2011.

[140] B. Fu and L. Gao, "Tantalum nitride/copper nanocomposite with zero temperature coefficient of resistance.," *Scr. Mater.,* vol. 55, no. 6, pp. 521 - 524, 2006.

[141] E. A. G. Pineda and A. Hechenleitner, "Characterization of Ethylcellulose Films Containing Natural Polysaccharides by Thermal Analysis and FTIR Spectroscopy.," *Acta Farm. Bonaerense,* vol. 23, no. 1, pp. 53 - 57, 2004.

[142] M. K. Shahzad, M. Ubaid, M. Raza and G. Murtaza, "The formulation of flurbiprofen loaded microspheres using hydroxypropylmethycellulose and ethylcellulose.," *Advances in clinical and experimental medicine,* vol. 22, no. 2, pp. 177 - 183, 2012.

[143] D. J. Finn, M. Lotya and J. N. Coleman, "Inkjet Printing of Silver Nanowire Networks," *ACS Appl. Mater. Interfaces,* vol. 7, no. 17, pp. 9254-9261, 2015.

Appendix I

Operating Procedure for Liquid Dispersion Absorbance Measurements on CARY 5000

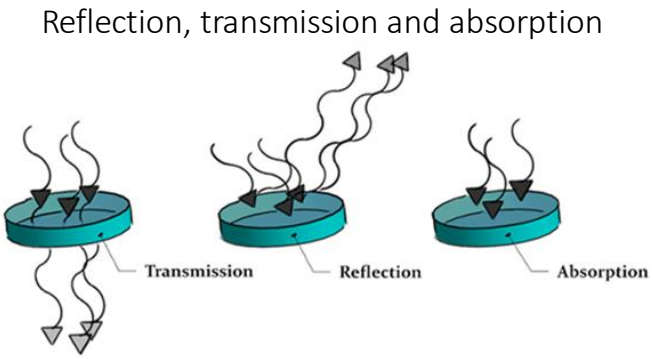

Fig. 1. Possible interactions of light with different substrates.

The information below is specifically for measuring absorption

I. Preparation of samples

a. The dispersion sample should have been allowed to stabilize at least 12 hours, this will allow for any precipitate to form and leave supernatant with stable dispersion. (This will of course depend on the requirements of the specific experiment).

b. Obtain supernatant for each dispersion sample that will be tested. Remember you need at least around 3.5 ml of testing liquid in the cuvette.

c. Prepare a box with the supplies you will need: quartz cuvettes, solvent, dispersions (samples to be measured), gloves, disposable pipettes, pipettor, klean wipes, double adhesive tape, flash drive (memory stick), etc. (See Fig.2.).

d. Bring all necessary material to cleanroom being careful not to disturb the dispersions in case there was more precipitate formed.

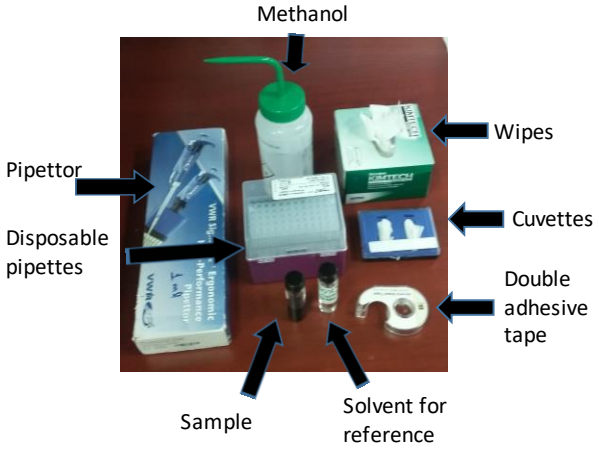

Fig. 2. Supplies needed for Liquid Absorbance Measurements.

II. Equipment Procedure

a. Turn on CARY and computer. Warm up the system at least 30 min before starting.

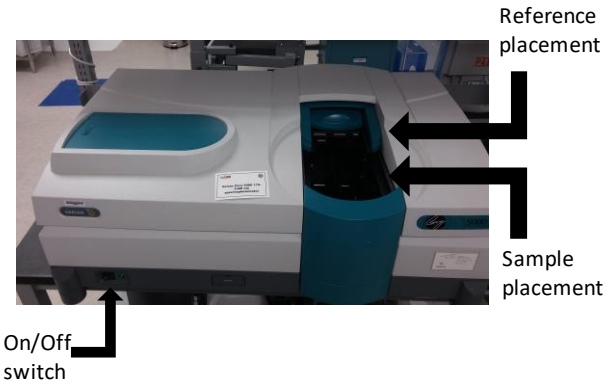

Fig. 3. CARY 5000 image indicating on/off switch and sample placement positions.

b. Rinse the cuvettes with methanol at least twice and also clean them on the outside.
c. Prepare sample holders (See Fig. 4a).
d. Using only solvent prepare the cuvettes for the initial baseline measurement. Using the pipette extract 3.5 ml from solvent and carefully fill both cuvettes always being careful of holding them by the sides, not the front of the cuvette, or you have to clean them again.

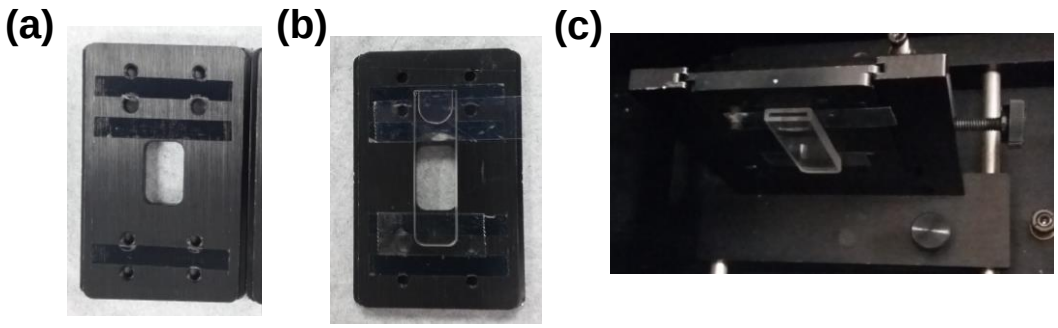

Fig. 4. a) Sample holder, b) sample holder with cuvette, c) sample holder and cuvette inside CARY.

e. Place both cuvettes on their respective sample holders and place them in the CARY 5000. Close the lid. (See Fig. 4b and c).
f. Open scan software from the icon in desktop.
g. From the **settings** window, choose **zero baseline correction**, press apply. (See below for explanation regarding baseline) Make sure you have selected "absorption" mode in settings. Choose the range of wavelengths to measure, (200 to 800 nm is the default settings).
h. Make sure "double beam" is selected. Time average: 0.1s, Data integral: 1nm.
i. Usually scan rate of 600nm/mm will work. (Default).

j. Press "obtain baseline" and continue to follow the instructions to place reference samples when indicated (See Fig. 5).

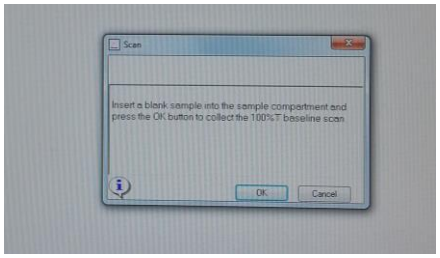

Fig. 5. Software prompts for baseline corrections.

k. When prompted, open the lid and cover the sample, close lid again to allow for zero absorption. (See fig.6).

Fig. 6. Covered sample for baseline correction.

l. Remove cuvette that holds reference sample. Discard solvent and rinse.
m. Using the pipettor, extract 3.5 ml from the supernatant (top) of the dispersion you want to measure and carefully fill the cuvette. Attach to holder (Fig. 7).

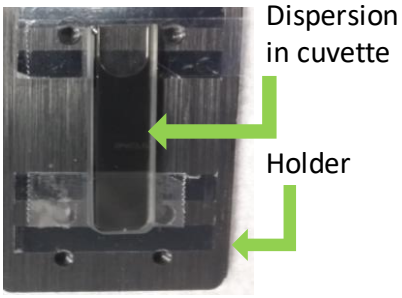

Fig. 7. Dispersion in cuvette on sample holder.

n. Place on the sample holder in CARY. Make sure cuvettes are steadily attached to holders. (Fig 4c and 8).

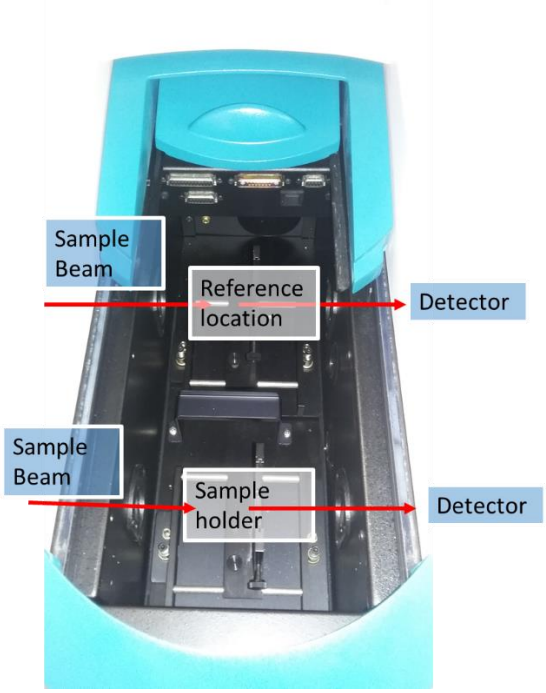

Fig. 8. Location for the positioning of samples, reference and ray path.

o. Select "start" and make sure you have selected the file saving destination you want the data to be saved on.
p. After the measurement is done, the software will automatically add a number to the name in preparation for the next measurement. At this point you may modify the name and test another sample, or finish the measurements. (See Fig. 9a).
q. If you finish the measurements, from the file menu, save your data as **.csv** file so that you can see it in **Excel**. (Fig. 9b).

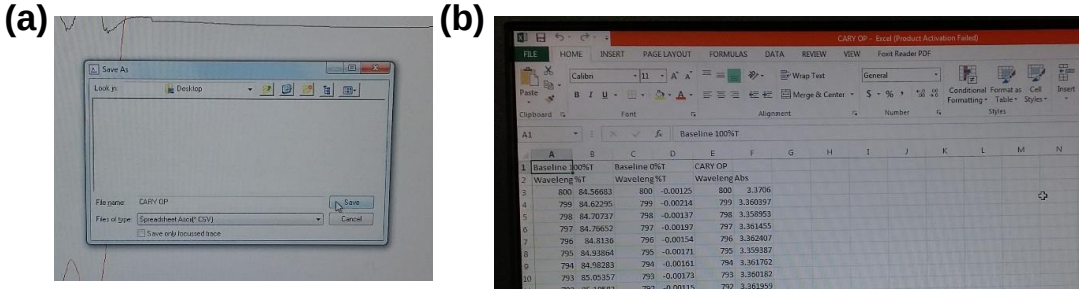

Fig. 9. Images of monitor as files are being saved (a) and excel with data (b).

r. Repeat according to number of samples to be tested. If the only difference between samples is concentration, you may continue with the same baseline. If there is any change in the solvents, you will have to get a new baseline for each different solvent you use.

s. Obtain measurements for all the samples you need.
t. When finished, remove both holders, the one with your sample and the one for the reference from CARY and turn equipment off.
u. Repeatedly rinse cuvettes with methanol, especially the one containing the dispersion.
v. Collect all material and take back to the lab being careful not to forget the memory stick.
w. If necessary, rinse cuvettes again, you may place individual cuvette in sonicating bath in methanol only if it is absolutely necessary and do it for 10 seconds at a time.
x. Put everything back where it should be.

Basic Operation Principle

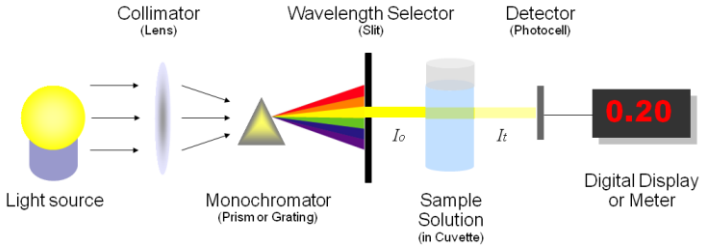

Fig. 10. Operation principle of absorbance spectroscopy.

III. Baseline or Calibration

Choose BASELINE from the Commands menu or settings. Select Zero Baseline correction.
When prompted, insert the blank sample into the sample compartment front beam and click OK.
After the baseline is collected, the word 'baseline' will be displayed in red in the ordinate status box, indicating that you are in baseline correction mode and have a valid baseline file for the correction.
Click the Start button or choose Start from the Commands menu to start the Scan run.

NOTE. It is very important to identify the baseline or reference one will be using. The zero baseline correction removes background noise, which is constant from the information you want to measure. The only difference between the baseline reference solvent in the cuvette and the sample should be whatever it is you are interested in measuring. For example, if the interest is in measuring graphite suspended particles in a solvent that also has a surfactant, the reference samples should include the solvent and the surfactant.
So if more than one element or compound is present in the samples, the same must be true for the reference (solvent). If the samples contain more than one liquid in a specific ratio, the same must be true for the baseline run. If the ratio of liquids varies from one sample to another, each one needs to be run as a baseline.

Liquid samples can be measured "dry"

IV. Measuring absorbance on dry samples

Another way of measuring absorbance of liquid samples is by drop casting them unto a substrate. Transparent VWR glass slides may be one option; quartz would be better, although more expensive.

a) In this case, the reference samples would be the clean glass slides, and the sample would be a glass slide containing the drop casted liquid. Definitely you cannot mix different types of slides for the reference and the sample.
b) For this type of measurements, it is critical that conditions for drop casting are first determined.
c) The samples that are going to be measured and compared should be drop casted in equal conditions as far as thickness, uniformity of film, etc. to avoid any deviation in the measurement due to differences in the above mentioned characteristics.
d) Follow the same instructions as liquid measurements, but using drop casted liquid samples on slides instead.
e) Turn on CARY and computer. Warm up the system at least 30 min before to start.
f) Prepare samples by drop casting on glass slides. Place samples in holders in CARY (Fig. 4).
g) Open scan software from the icon in desktop.
h) From the settings window, choose zero baseline correction, press apply. Make sure you have selected "absorption" mode in settings. Choose the range of wavelengths to measure, (800 to 200 nm is default setting).
i) Make sure "double beam" is selected. Time average: 0.1s, Data integral: 1nm.
j) Usually scan rate of 600 nm/mm will work.
k) Press "obtain baseline" and continue to follow the instructions to place reference samples when indicated. (See Fig 5).
l) When prompted, open the lid and cover the sample, close lid again to allow for zero absorption. (See Fig. 6).
m) Remove reference sample.
n) Place glass slide containing drop casted sample on holder.
o) Place on the sample holder in CARY. Make sure samples are steadily attached to holders (Fig. 8).
p) Select "start" and make sure you have selected the file saving destination where you want the data to be saved.
q) After the measurement is done, the software will automatically add a number to the name in preparation for the next measurement. At this point you may modify the name and test another sample, or finish the measurements. (Fig. 9a).
r) If you finish the measurements, from the file menu, save your data as **.csv** file so that you can later see it in Excel. (Fig. 9b).
s) Repeat according to number of samples to be tested.
t) Obtain measurements for all the samples you need.
u) When finished, remove both holders, the one with your sample and the one for the reference from CARY and turn equipment off.
v) Collect all material and take back to the lab being careful not to forget the memory stick.
w) Put everything back where it should be.

REFLECTION MEASUREMENTS
(Information from the Manual)

Reflection consists of two components: specular and diffuse. Specular reflectance is the mirror-like reflection off a sample surface. Diffuse reflectance occurs when the surface reflects light in many different directions, giving the surface a matt appearance.

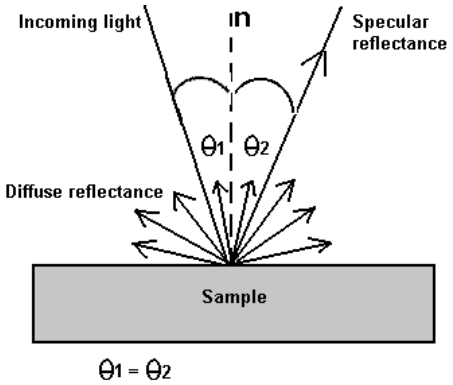

Fig. 11. The two components of reflection: specular and diffuse reflection. N represents the surface normal, an imaginary line perpendicular to the sample surface.

Traditionally, the accessory used to measure diffuse reflectance is the integrating sphere. Applications include characterizing solar materials, color measurement and characterization, and obtaining reflectance spectra of a painted surface. Integrating spheres have also proven ideal for measuring the transmission of turbid, translucent or opaque refractory materials where standard techniques proved inadequate due to loss of light resulting from the scattering effects of the sample. Samples which distort the beam of the instrument, such as a lens, can also be studied with the Diffuse Reflectance accessory.

The relative spectral reflectance (transmittance) is defined as the ratio of the flux reflected (transmitted) by the specimen to that of a standard surface under identical geometrical and spectral conditions. For transmittance the standard surface is air, and for reflectance the standard surface is a secondary white standard calibrated relative to the perfectly reflecting diffuser.
Because of the geometry of the integrating sphere, it has the ability to collect most reflected or transmitted radiation, remove any directional preferences, and present an integrated signal to the detector.

Whilst the DRA should be used when measuring the transmittance of opaque or diffusing solid samples, the accessory may also be used when measuring turbid liquids. **DRA was not used in this work;** however, it can be read from the above descriptions, DRA could potentially be a useful tool in the evaluation of the dispersions, as mentioned above, it may be used to measure "turbid liquids".

Reflectance measurements

In case Diffuse Reflectance Measurements are desired, please check the user guide or: http://mmrc.caltech.edu/Cary%20UV-Vis%20Int.Sphere/manuals/Cary5000_User_Guide.pdf

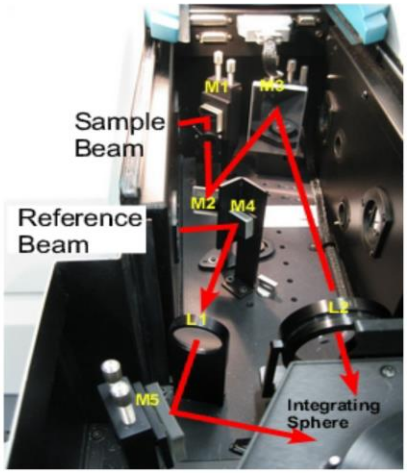

Fig. 12. Image of ray path when integrating sphere is used.

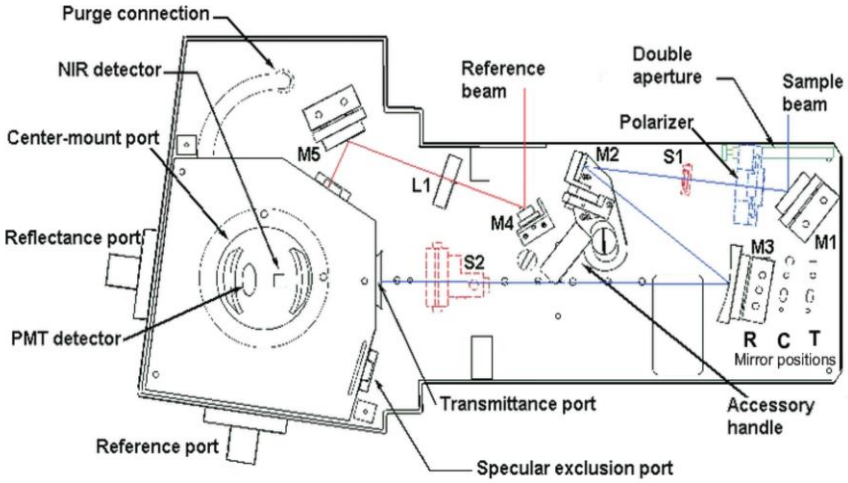

Fig. 12. Illustration of Ray path in Reflection Measurements.

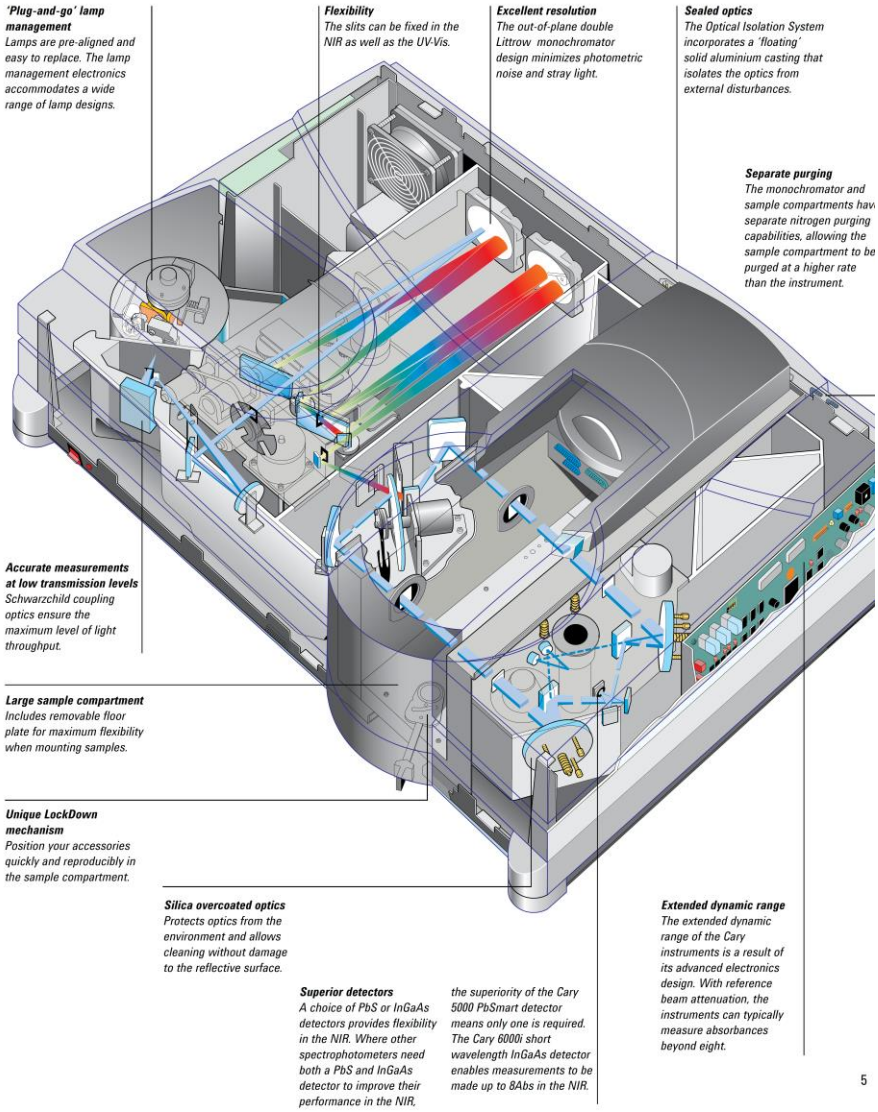

Fig. 13. Illustration of CARY 5000 and its advantages.

Vita

Mónica was born in Guadalajara, Mexico, she eventually moved to Mexico City, where she studied two years of Chemical Engineering at the National Autonomous University of Mexico (UNAM). She continued her studies in the Metallurgical and Materials Engineering Department at UTEP and obtained her Bachelor's and Master's Degrees. She moved to West Lafayette, IN where she began her career as a teacher at Purdue University as an Associate Professor in Spanish. Later on, she moved to Changzhou, China where she was a professor at the High School level teaching Science and Spanish. Mónica then returned to Cd. Juarez, Mexico where she taught various subjects such as Mathematics, Scientific Methods, Mechanics, Dynamics, Thermodynamics, and Electricity at the High School and Professional levels at the ITESM (Tec de Monterrey) in Cd. Juarez.

She returned to UTEP to pursue her Ph.D. in fall 2014 and joined the NDL (Nanomaterials and Devices Laboratory) where she began working under the direction of Professor Anupama B. Kaul. She has participated in various Conferences and Meetings such as IEEE, MRS, and the 2D Workshop in Washington DC in April, 2015. Her work during her Ph.D. has concentrated in exploring the preparation of 2D materials inks and optimizing their characteristics for printing. The future of this work is the expansion of device manufacturing using the inkjet printing technique and solution based processing.

Contact Information: monicamichelp@gmail.com

This thesis/dissertation was typed by Monica Michel.